Variability of methanol and OH masers associated with the star forming region G339.62-0.12

M Seidu

orcid.org 0000-0002-3858-3681

Dissertation accepted in fulfilment of the requirements for the degree *Master of Science in Astrophysical Sciences* at the North-West University

Supervisor:	Prof DJ van der Walt
Co-supervisor:	Dr S Goedhart

Graduation May 2020

28281942

Declaration

I, Mavis Seidu, declare that this thesis titled, **VARIABILITY OF METHANOL AND OH MASERS ASSOCIATED WITH THE STAR FORMING REGION G339.62-0.12** and the work presented in it are my own. I confirm that:

- This work was done wholly or mainly while in candidature for a research degree at this University.
- Where any part of this thesis has previously been submitted for a degree or any other qualification at this University or any other institution, this has been clearly stated.
- Where I have consulted the published work of others, this is always clearly attributed.
- Where I have quoted from the work of others, the source is always given. With the exception of such quotations, this thesis is entirely my own work.
- I have acknowledged all main sources of help.
- Where the thesis is based on work done by myself jointly with others, I have made clear exactly what was done by others and what I have contributed myself.

Signed: 

Date: February 20, 2020

Abstract

Astrophysical maser emission from various molecules and in a number of astrophysical environments is now a well-known phenomenon. Since the first discovery of hydroxyl (OH) maser emission by Weinreb et al. (1963), the use of masers to obtain information of the kinematics and physical properties of the environments where they occur, have expanded significantly. Masers occur in compact dusty dense regions and are associated with various environments such as high-mass star forming regions (SFRs), circumstellar envelopes around late-type stars, comets and even extragalactic galaxies. The physical conditions of these environments can be investigated through maser indications such as variability (i.e. the variations in the maser flux density).

Periodic variability was first evident in the brightest class II methanol (CH_3OH) masers associated in G9.62+0.19E (Goedhart et al., 2003). The discovery has led to several more studies of periodic variable masers in various high-mass SFRs. In various high-mass SFRs, the class II methanol masers are known to spatially coincide with OH masers and have a similar pumping mechanism (Cragg et al., 1992). It is, therefore, necessary to also investigate the OH masers for periodic behaviour other than just that of methanol.

This work presents the parallel observation of the 6.7 GHz CH_3OH and the mainline (1665 and 1667 MHz) OH masers in G339.62-0.12 carried out from February 2013 to July 2015. The 26 m single-dish telescope at the Hartebeesthoek Radio Astronomy Observatory (HartRAO) and the Karoo Array Telescope (KAT-7) are used respectively. The radio continuum at 18 cm observed with the KAT-7 is also presented.

The findings of this work show strong evidence of variability as well as periodicity of the 6.7 GHz CH_3OH and the mainline OH masers associated with G339.62-0.12. From the time-series analysis, the maser features are seen to be blue- and red-shifted from the systemic velocity ($V_{\rm sys}$ = -34.2 km s^{-1}). One interesting aspect is that periodic variability is clearly visible for the blue-shifted masers with velocities ranging between -37.6 km s^{-1} to -35.5 km s^{-1}. Using the Lomb-Scargle (LS) periodogram, the periods for the 6.7 GHz methanol, the 1665 and 1667 MHz OH masers are found to be 203 ± 2 days, 208 ± 2 days and 210 ± 2 days respectively. These periods fall within the derived periodicity (23.9-668 days) for all the periodic maser features. The red-shifted masers seem to show uncorrelated variability with some sort of periodicity. The period for the red-shifted masers is found to be 193 days, which is less than the periods of the blue-shifted masers. This may be an indication that the red-shifted masers are possibly associated with a different SFR. Although the mainline OH maser emission occurs in the same region as the 6.7 GHz CH_3OH, from our results we can deduce that they are not spatially co-located.

Keywords— High-mass star formation, molecular clouds, H II region, radio astronomy, masers

Acknowledgements

I want to render my gratitude to my supervisors, Prof Johan van der Walt and Dr Sharmila Goedhart. Through your impactful knowledge, wisdom and advice, we have been able to complete this work successfully. It has been a long journey, but I am grateful that all our meetings contained the solutions needed to push on with this work. Whenever I thought it was over, you always inspired me with your creative ways of handling things. Thank you, Prof Johan van der Walt, for making me laugh often.

I also would like to thank Prof and Mrs Chibueze for giving me support and tremendous advice to get this far. Thanks to Dr Bruno Letarte for the Friday braais and telescope outreaches. A big thank you to Dr Jabulani Maswanganye, whose knowledge taught me to always learn more and also for your technical support. I also want to render my appreciation to my Dad and Mom (WOII and Mrs Seidu) and siblings for their encouragement, support and love throughout this amazing journey.

We are thankful for the financial support from the Square Kilometer Array (SKA) which is now part of the South Africa Radio Astronomy Observatory (SARAO), the National Research Foundation (NRF) and the Centre for Space Research (CSR). Many thanks go to the NWU for their postgraduate financial support. I will also like to acknowledge the HartRAO and the SKA for allowing us to use their organisational facilities, telescopes and data. I cannot end without thanking Mrs Petro Sieberhagen and Prof Stefan Ferrera for their support. Thanks to Mr and Mrs van der Merwe for welcoming me to your home for breaks to revitalise myself.

My profound appreciation goes to Ms Marielle Tappan for proofreading and reviewing this work. My final thanks go to friends for being resourceful to me, providing some hours of entertainment and being there to hug me most of the time.

Contents

List of Figures

List of Tables

Chapter 1

Motivation of study

1.1 Overview

The detection of astrophysical masers by Weinreb et al. (1963) and Turner (1970) has implicitly spawned a new era of research on high-mass star formation (HMSF). Astrophysical masers are spatial events that result from stimulated emission of radiation and have high brightness temperatures ranging from 10^6 K to 10^{12} K (Sobolev et al., 1997). The brightness temperature of a radio source defined by Reid & Moran (1981), is the "temperature of a blackbody required to produce radiation of the same spectral intensity". Due to their amplification properties, masers are good probes of SFRs and serve as useful tools for investigating star formation processes and activities such as that of high-mass stars (Elitzur, 1992).

Maser emission in SFRs arises from various molecules including CH_3OH, OH, water (H_2O), silicon monoxide (SiO), ammonia (NH_3) and formaldehyde (H_2CO). Among these masers, methanol masers are exclusive to high-mass SFRs. They often coincide with HMSF indicators such as the ultra-compact H II regions and infrared (IR) sources (Ellingsen et al., 2007), making them good tracers of early HMSF.

Methanol masers have been categorised into two main classes; the class I and class II methanol masers (Batrla et al., 1987; Menten, 1991). Each class consists of a set of masing transitions associated with one of the symmetry groups (A- and E-type) of methanol (Lin & Swalen, 1959). The class I methanol masers include those at 9 GHz, 25 GHz, 44.1 GHz, 95.2 GHz and 132 GHz. They are collisionally pumped. The class II methanol masers occur at 6.7 GHz, 12.2 GHz, 23.1 GHz, 38.8 GHz and 107 GHz. They are detected in close proximity to H II regions and are radiatively pumped (Cragg et al., 1992; Sobolev et al., 1997). The pumping in masers causes excitation to occur from lower to higher energy levels through radiative processes or collisions.

Among the two classes of methanol masers, extensive studies have been carried out towards the class II methanol masers. This is primarily because the class II methanol masers are the brightest of the two classes masers. Unlike the class I methanol masers, the class II methanol masers lack any association with young low-mass stars ($M < 3\,M_\odot$) as well as evolved or late-type stars (Breen et al., 2013; Ellingsen, 2006). For example, the 6.7 GHz CH_3OH maser are exclusively associated with HMSF. However, Very Long Baseline Interferometer (VLBI) observations by Menten et al. (1992) in milliarcsecond resolution show the 6.7 GHz CH_3OH masers to be spatially coincident with the OH in some SFRs. Each of these masers consequently traces a different physical condition of the environments where they form.

MacLeod et al. (1993) and Caswell et al. (1995) reported the 6.7 GHz CH_3OH masers to be variable. To further investigate the nature and time-scale of the variability at 6.7 GHz, Goedhart et al. (2004) did extensive monitoring of 54 high-mass SFRs from January 1999 to March 2003. Forty-six of

the sources were found to be variable while eight were not. The variability of the masers included monotonic increase and decrease, quasi-periodic, aperiodic and periodic variations.

Periodic variable maser was first discovered by Goedhart et al. (2003) in G9.62+0.20E. From the monitoring programme, which was later extended to a total term of 10 years (Goedhart et al., 2014), seven additional high-mass SFRs were found to have periodic 6.7 GHz CH_3OH masers. The periods of these masers were found to range between 132.8-520 days. Sugiyama et al. (2017) also observed the 6.7 GHz CH_3OH masers in G014.23-00.50 and found the masers to have a short period of only 23.9 days. Currently, there are about 26 known periodic variable masers that have been detected (see Goedhart et al., 2014; Maswanganye et al., 2015, 2016; Szymczak et al., 2015). These include the newly discovered periodic variable 6.7 GHz CH_3OH maser associated with G323.46-0.08 (Proven-Adzri et al., 2019). Some of the known periodic masers have been listed in Table 1.1. Various models have been proposed to explain some possible mechanisms that can account for the observed periodicity. These models are based on the changes in the flux of the seed photons from background free-free emission (van der Walt, 2011) or changes in the maser pump due to radiative mechanisms (Van der Walt, 2014).

1.2 Research motivation

There are comparatively few high-mass SFRs where other maser species also exhibit periodic variability. Araya et al. (2010) first identified periodic variability in formaldehyde following the discovery of periodic methanol masers in G9.62+0.20E. Periodic OH maser associated with G12.88+0.49 was first reported by Green et al. (2012). The time-series, however, were under-sampled and there were weak indications of periodicity. Recently, Goedhart et al. (2019) reported on periodic OH masers associated with G9.62+0.20E. Goedhart et al. (2019) found the mainline OH masers strongly correlate with the 6.7 and 12.2 GHz CH_3OH masers in G9.62+0.20E. The OH maser features have sharp dips that appear when the 12.2 GHz CH_3OH maser starts to flare. Although weak flares were seen for the OH masers, the drop of the dips always coincides with the minima of the 6.7 GHz CH_3OH masers. Another intriguing aspect of their result is that, in projection, the periodic flaring methanol masers and the OH masers are found to be 1600 AU apart.

Since the 6.7 GHz methanol and the mainline OH masers are both pumped under similar excitation conditions (Cragg et al., 2002), they become interesting sources to possibly investigate in more detail. It is also essential to find periodic behaviour of other maser species associated with known periodic methanol masers such as the mainline OH masers. This can significantly add to our understanding of the underlying mechanism that drives the periodic masers in the SFRs. In this work, we investigate the 1665 and 1667 MHz OH masers associated with G339.62-0.12 for possible periodic behaviour.

TABLE 1.1: Lists of currently known periodic sources.

Source	Period (days)	D (kpc)	Luminosity ($L_\odot \times 10^4$)
G9.62+0.19	243.3	5.2± 0.6	270± 132
G12.68–0.18	307.0	2.4± 0.17	5.2± 1.3
G12.89+0.48	29.5	2.3± 0.13	21.5± 4.4
G14.23–0.50	23.9	2.0± 0.14	0.5± 0.1
G22.35+0.06	178.0	4.3± 1.4	8.4± 2.9
G24.14–0.01	182.0	13.5± 0.3	25± 5.0
G25.41+0.10	245.0	9.0± 0.3	18.7± 5.6
G30.40–0.29	222.0	7.2± 0.7	5.9± 1.5
G33.64–0.22	540.0	7.6± 1.0	14.4± 1.9
G36.70+0.09	53.0	10.0± 0.4	10.8± 2.7
G37.55+0.20	237.0	4.9± 0.5	31.9± 4.8
G45.47+0.13	195.7	7.8± 0.4	56± 14.0
G59.63–0.19	149.0	3.5± 0.3	6.5± 1.6
G73.06+1.8	160.0	2.4± 0.3	12± 3.0
G75.76+0.34	199.9	3.5± 0.3	138± 33.0
G107.29+0.63	34.4	0.76± 0.03	0.39± 0.1
G108.76–0.99	163.0	3.2± 0.2	48± 12.0
G188.95+0.89	404.0	2.1± 0.27	25± 6.0
G196.45–1.60	668.0	5.3± 0.024	132± 33.0
G328.24–0.55	220.5	2.8± 0.5	70± 17.0
G331.13–0.24	504.0	5.0± 0.5	53± 27.0
G338.93–0.06	133.0	3.2± 0.5	4.0± 1.0
G339.62–0.12	200.3	2.9± 0.5	12± 3.0
G339.98–0.42	246.0	5.5± 0.4	27± 14.0
G358.46–0.39	220.0	2.8± 0.7	3.0± 0.8
G323.46–0.08	93.5	–	–

Column 1: The name of known observed periodic masers. Column 2: The periods of the methanol masers. Column 3: The distances of the sources. Column 4: Bolometric luminosity of the sources. This table was adopted from Table A.3 of Olech et al. (2019). References to individual sources can be found in Olech et al. (2019) and Proven-Adzri et al. (2019).

Chapter 2

High-mass star formation, tracers and astrophysical masers

Figure 2.1 is an example of a high-mass star forming complex where dark lens of dust is seen to obscure incoming light from newly forming young massive stars. The environments are mostly molecular and are called molecular clouds. They are made up of gaseous and dust matter that interact with radiation passing through them. They are characterised by their complex morphology and optically thick dense structures where newly forming stars are harboured. This chapter presents a brief introduction of HMSF and describes their environments. Astrophysical masers formed in massive SFRs are also presented. This includes how they trace HMSF and the basic theory of forming astrophysical masers.

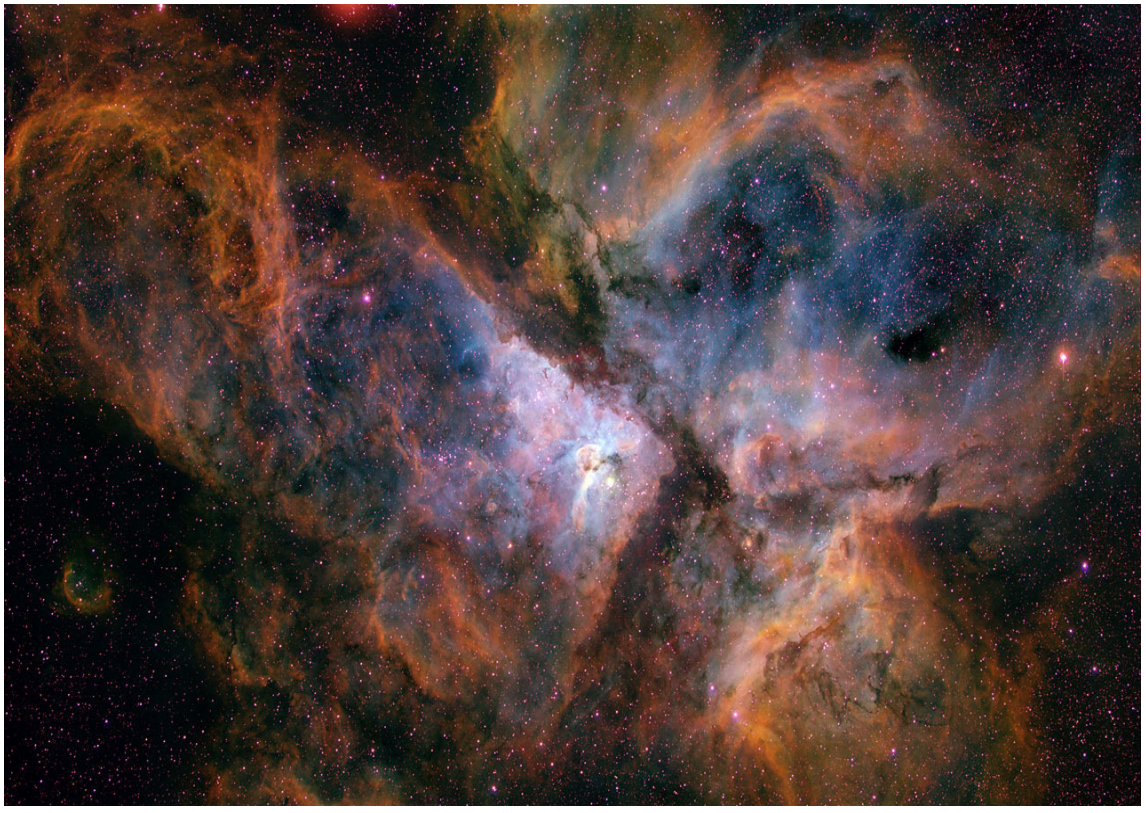

FIGURE 2.1: An example of a high-mass star forming molecular cloud (the Carina nebula) taken by combining three different optical band filters (blue, green and red). Image credit: N.Smith (University of California, Berkeley) and NOAO/AURA/NSF.

2.1 High-mass star formation: A general overview

High-mass stars, also referred to as massive stars, have masses of $M_* \geq 8\,M_\odot$. These are hot OB stars and have luminosities higher than 10^3 $L_\odot$ (Zinnecker & Yorke, 2007). At the earliest phase of their formation, newly forming massive young stellar objects (MYSOs) are deeply embedded within dusty cocoons of their natal cloud. This makes it difficult to directly observe newly forming MYSOs. Yet, through the studies of molecular lines and continuum emission (in the near-IR and millimetre emission), it has become possible to effectively trace their formation. For example, masers are found within compact regions of the molecular clouds and can easily probe such regions.

Massive stars dynamically have an influence on the evolution of most galaxies including the Milky Way Galaxy, making them essential to study. Massive stars are a major source of Ultra Violet (UV) radiation which can ionize the surrounding interstellar medium (ISM). This leads to changes in the physical properties of that part of the ISM. Also, UV photons ionise neutral hydrogen which consequently leads to the creation of H II regions. During their lifetime, massive stars possess strong stellar winds which transfer mechanical energy into the ISM. This compresses gases and creates shock fronts around the H II regions. Shocked gases produce shock waves which rapidly move through the H II regions causing the region to expand. This expanding region also causes other nearby regions to compress and sequentially triggers the formation of new massive stars in those regions (Bonnell & Dobbs, 2007). At the end of their life, massive stars can produce huge amounts of heavy elements through supernova explosions. The heavy elements are responsible for cooling processes and are dispersed within the Milky Way Galaxy (Klessen & Glover, 2016).

Though massive stars are important, their formation is extremely complex and has not been fully understood. Firstly, inspection of the stellar luminosity function for stars within a radius of a 100 pc from the sun (see for example, pg 85 of Scheffler & Elsasser, 1988) and also Kroupa (2002), shows that the stellar luminosity density is of the order of $10^{-8}\,pc^{-3}mag^{-1}$ compared to $34 \times 10^{-4}\,pc^{-3}mag^{-1}$ for solar mass stars. This shows that massive stars are extremely rare. A further explanation can also be due to their extremely short lifespan since they quickly exhaust their nuclear fuel once they reach the main-sequence. Secondly, the environments where HMSF occur are generally complex to observe. At the early stages moreover, newly forming MYSOs are not visible to optical and IR observations due to weak radiation fields of the MYSOs. However, radio, millimetre and sub-millimetre observations have successively made it possible to probe closer to the regions massive stars are forming (Zinnecker & Yorke, 2007). Lastly, massive stars form while they are deeply embedded inside optically thick clouds, making it difficult to observe individual massive stars (Motte et al., 2018).

In recent years, several theoretical models and observational studies have been aimed towards understanding massive star formation (Krumholz, 2015; Tan et al., 2014; Yorke & Sonnhalter, 2002; Zinnecker & Yorke, 2007). The two most competing proposed scenarios are the core accretion model and the competitive accretion theoretical model.

In the core accretion model, molecular clumps fragment under initial self-gravitating conditions such as turbulence. Individual cores which serve as the object for forming the MYSO are formed from the fragmented clouds (Bonnell et al., 2004). The cores form until they reach a mass of the order of the Jeans mass where gravitational collapse is beginning. The collapse is initiated at the centre of the core, thus the centre becomes condensed. The gas of the inner core becomes adiabatic

when it reaches a density $\rho \sim 10^{-13}\,\mathrm{g\,cm^{-3}}$ and the temperature increases (McKee & Ostriker, 2007). The gas in the core become high enough to cause hydrogen dissociation, thereby leading to another collapse. Afterwards, a hydrostatic core which becomes the protostar through accretion is formed. When the accreting matter has lower angular momentum, a protostellar disk of size $\sim$ 1000 AU is formed (Krumholz & Bonnell, 2007). When the angular momentum is large, a low-mass protostar will be formed. Since the mass of the cores determines the mass that will form the stars, the most massive cores are predicted to end up forming a single or multiple massive stars (Bonnell, 2001; Krumholz et al., 2009) than cores with less mass. Due to lack of observations, it is still debatable whether HMSF is a scaled-up version of low-mass stars or not.

The competitive accretion model satisfies the condition that massive stars form through the Bondi-Hoyle-Lyttleton accretion and the in-falling matter occurs unto a cluster. The clustered stars compete for the same molecular gas reservoir, but the stars with the deepest well will form massive stars by accumulating most of the molecular gas. Thus, the competitive accretion ends up forming massive protostellar clusters rather than a single stellar object (McKee & Tan, 2002). Despite the complexities of how massive stars form, it is however necessary to understand the mechanisms at play in their SFRs. The subsection below gives a brief description of HMSF environments and some evolutionary phases of HMSF.

2.1.1 Environments and evolution of high-mass star formation

HMSF occur in massive clouds, referred to as Giant Molecular Clouds (GMCs). The GMCs have masses $\gtrsim 10^5\,\mathrm{M_\odot}$, confined to the spiral arms of the Milky Way Galaxy and thus, they become the main sites for HMSF to occur in the Milky Way Galaxy (Blitz, 1993). GMCs have non-uniform density where certain parts are less dense than other parts. The lower density regions appear to have long strands of filamentary structures. The filaments have higher than average substructures known as clumps running along with them as shown in Figure 2.2. The clumps have smaller sizes (about 1 pc) and masses of 10^2-$10^3\,\mathrm{M_\odot}$. The lifetime for the less massive clumps is estimated to be $5{\times}10^4$ yr while that of clumps with masses greater than $10^5\,\mathrm{M_\odot}$ is estimated to be $1{\times}10^4$ yr (Urquhart et al., 2018). The more massive clumps ultimately form rich clusters of massive stellar objects than the less massive clumps (Tigé et al., 2017).

Subunits of dense molecular cores, considerably smaller in size (< 0.1 pc), are found inside the clumps. The cores have uniform densities than that of the clumps. They are the earliest detection phase of massive star formation and are generally observed in distinct phases. They start with a cold core phase to a hot core phase. The temperature range for these phases is ~10-200 K (Hoare et al., 2007). The cold phase is the first evolutionary phase of HMSF. These are *starless cores* in which no gravitational contraction is identified. Observationally, they are cold dark clouds that are only observable at millimetre wavelengths. These cores are harboured in dark filamentary clouds and can easily be detected through observations of infrared dark clouds (IRDCs). Such observations reveal absorption features when the cores are observed against bright sources (Carey et al., 1998, 2000).

The cold cores have dust temperatures ranging between 10-15 K and typical density of $n_{\mathrm{H_2}} > 10^5\,\mathrm{cm^{-3}}$ (Churchwell, 2002). Subsequently, gravitational contraction begins until a temperature of 100 is reached, leading to the formation of hot molecular cores. Due to the contraction, the

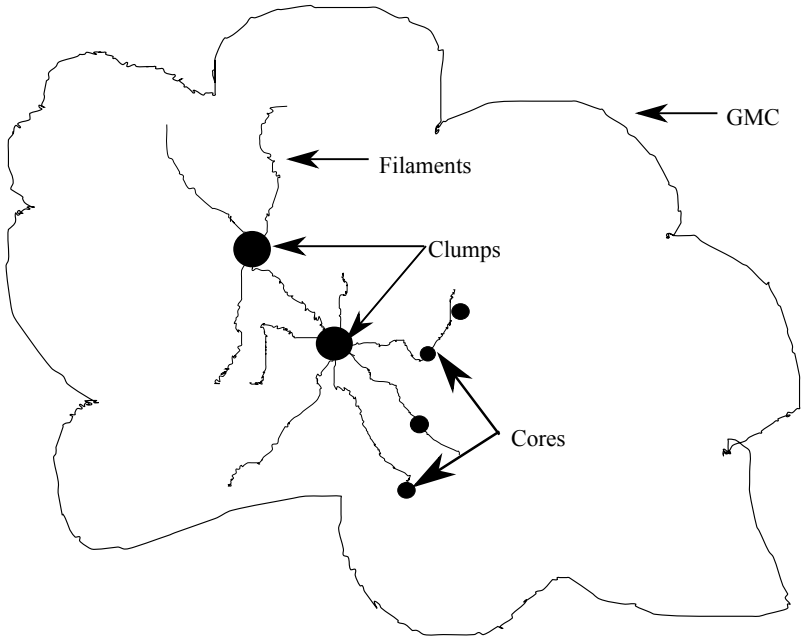

FIGURE 2.2: Schematic diagram of a GMC and its subunits.

internal pressure of the cloud increases and the central part becomes highly compressed. The cores are essentially the birth sites for MYSOs and have smaller sizes (< 0.1 pc) as well as high densities of about $n_{\mathrm{H_2}} \geq 10^7\,\mathrm{cm}^{-3}$ (Zinnecker & Yorke, 2007). As the core heats up, the internal motion of the cores increase the pressure increases and the potential energy is converted to kinetic energy. Lastly, the development of H II region marks the last phase of HMSF.

The evolutionary sequences of the H II region are, hyper-compact (HC), ultra-compact (UC), compact and finally, to the classic H II region. HCH II and UCH II regions are the smallest of the H II regions with sizes ≤ 0.1 pc and are compact with electron densities $n_H \geq 10^5\,\mathrm{cm}^{-3}$ (Stahler & Palla, 2005). They are the precursors of the H II region (Kurtz, 2005). Due to the high column density of the dust and gas surrounding these regions, they are only detectable at centimetre wavelengths (Churchwell, 2002; Hoare et al., 2007; Keto, 2003). H II region emit free-free radiations at such wavelengths which give rise to the flux of radio continuum emission.

2.2 Interstellar masers as tracers of massive star formation

Observational tracers of the early phase of HMSF in dense regions include mid- and FIR emission, HCH II and UCH II regions and interstellar masers such as CH_3OH, H_2O and OH masers. The presence or absence of any of the tracers gives an indication of the phase of HMSF evolution they are tracing. The various maser species trace different phases of HMSF processes. (Breen et al., 2010).

Interstellar masers are found in compact regions near MYSOs as shown in Figure 2.3. MYSOs produce UV radiation which heats up dust and gas components surrounding them. Diffuse IR emission from the heated dust grains ionise the regions and give rise to the creation of the H II regions. Winds from the MYSOs produce shock waves through interactions. The waves are

propagated through the region, leading to the expansion of the H II region. The edge of the expanding H II region is a thin layer of ionised gas called the ionisation front. Surrounding this layer is a propagating condensed shell called the shock front. Ionization photons produced from the wind interaction are absorbed in the region between the ionisation front and the shock front, producing seed photons for forming masers. Various masers observed in UCH II regions are found outside the ionised gas of the UCH II region (Menten et al., 1992). Since methanol and OH masers are known to coexist, it can be that these masers arise outside the ionised region (Sobolev et al., 2002).

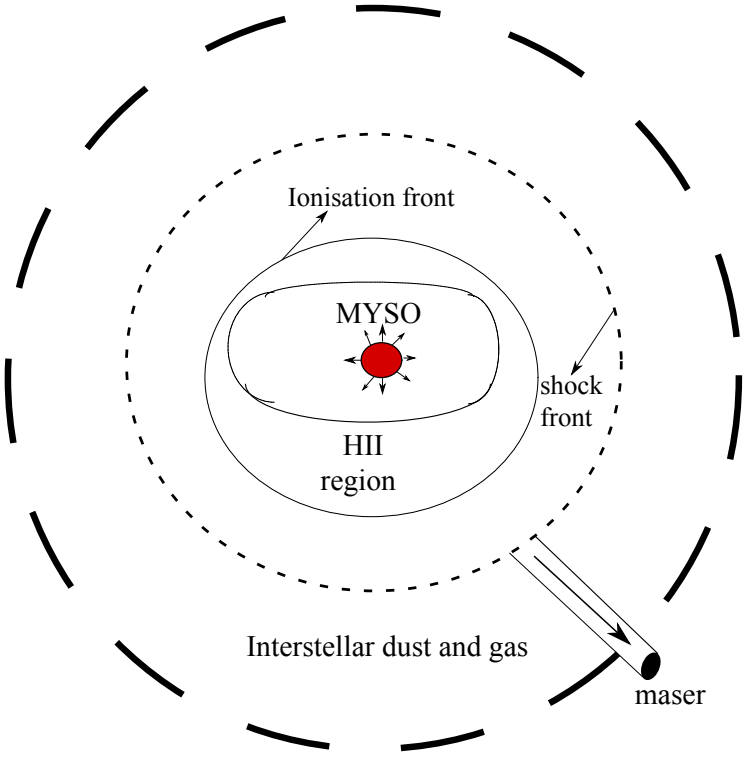

FIGURE 2.3: Schematic diagram representing tracers of a MYSO forming in an obscured dense SFR.

The region just beyond the envelope of the H II region is photon dominated and has a high abundance of interstellar molecular gas and dust. Temperature variations from the dust give information on the evolutionary sequence of the forming MYSO. From Figure 2.3, the masing region is found outside the H II region where enough photons can be produced to form masers (Menten et al., 1992).

The methanol molecule is the second most abundant molecule after H_2O molecules in massive star environments. They form through grain surface reactions occurring on icy grain mantles (Dartois et al., 1999). Icy mantles of water ice also evaporate from the surface of the grains to form OH in masing regions (Hartquist et al., 1995).

From the various OH masers, the interstellar mainline OH masers are prevalent. The 1665 MHz OH masers have stronger emission lines than the 1667 MHz OH masers. However, the spectra of these masers may look similar and have velocity coherence when they both appear in the same region. Although single-dish observations by Weinreb et al. (1965) found the OH maser transitions

not to resemble each other, some similarities are found based on the interferometric observations of Norris & Booth (1981). These masers are found near UC H II regions (Stahler & Palla, 2005).

Compared with H_2O masers, OH masers are found in the inner part of bipolar outflows while the H_2O masers lie away from the centre of the outflow (Stahler & Palla, 2005). H_2O masers are fundamentally known to be associated with shock gases which provide the mechanism for the pumping in H_2O masers and require high density regions. The OH and H_2O masers are found to be associated with SFRs and evolved stars. There is evidence of water masers tracing the evolutionary sequence of low-mass protostellar objects (Breen et al., 2010).

Lastly, in comparison to CH_3OH masers, OH masers in massive SFRs have a similar pumping mechanism as that of the Class II CH_3OH masers. They are both detected toward IR sources and found to be associated with bipolar outflows. Unlike H_2O and OH masers, methanol masers are not associated with late-type stars. This makes them exclusive tracers of massive star formation (Breen et al., 2013). In the next section, the theory of how masers form in interstellar space will be discussed. Maser emission requires interaction between a thermal source and a gaseous medium (e.g. atoms or molecules). Therefore, we will also present the mechanisms through which maser emission occurs.

2.3 Theory of astrophysical masers

[1] The term maser is an acronym for Microwave Amplification by Stimulated Emission of Radiation. Maser emission occurs when photons with energy ($h\nu$) stimulate molecules to produce more photons with an energy similar to that of the initial photons. Maser emission requires a population inversion between two energy levels which originates through collisions or interaction of molecules with non-black body radiation. Since astrophysical masers arise in a gaseous medium (Gray, 2012), the principle of radiative transfer will first be presented, considering interactions between the gaseous medium and radiation from a source. In this section, some of the conditions required for population inversion to occur will be described. The last subsection will present some of the pumping mechanisms which account for the population distribution in the energy levels of masers.

2.3.1 Radiative transfer

Consider radiation emitted from a thermal source and propagating through a medium, the direction along which the radiation propagates is denoted by s as shown in Figure 2.4. If the source of radiation is a blackbody, the radiation will be emitted isotropically. The blackbody is direction independent due to the isotropic distribution. However, the interest here is the flow of radiation through the medium at all points along a ray.

For radiation passing through an inhomogeneous medium, part of the radiation is emitted, absorbed and even scattered. The optical depth (τ_ν) of the inhomogeneous medium from one point to the other ds is defined as

$$d\tau_\nu = k_\nu ds \tag{2.1}$$

[1] This section is based on the reviews of Choudhuri (2010) and Gray (2012) with minor changes using the review of Elitzur (1992).

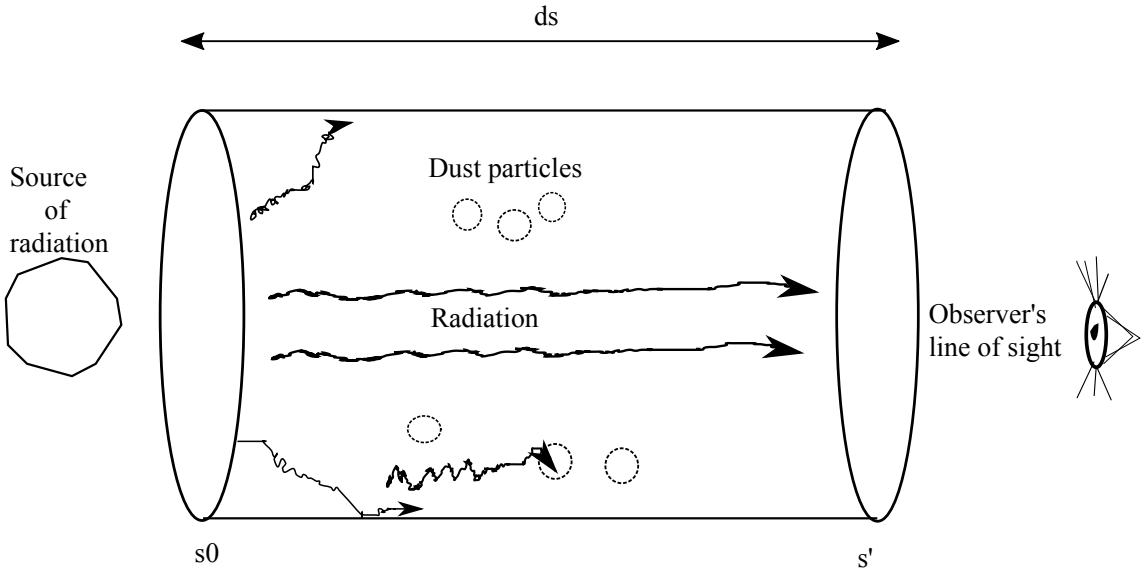

FIGURE 2.4: An illustration the flow of radiation from a source through a medium.

where ν is the frequency of the radiation and k_ν is the absorption coefficient. The equation of radiative transfer is

$$\frac{dI_\nu}{ds} = -k_\nu I_\nu + j_\nu \tag{2.2}$$

where I_ν is the specific intensity, j_ν is the emissivity and the ratio of the j_ν and k_ν is the definition for the source function S_ν. Dividing the radiative transfer equation in Equation 2.2 with the absorption coefficient and making use of Equation 2.1 and the source function, the radiative transfer equation becomes

$$\frac{dI_\nu}{d\tau_\nu} = -I_\nu + S_\nu \tag{2.3}$$

Also, multiplying Equation 2.3 by e^{τ_ν} gives

$$\frac{dI_\nu}{d\tau_\nu}(e^{\tau_\nu}) + I_\nu e^{\tau_\nu} = S_\nu e^{\tau_\nu} \tag{2.4}$$

which is simplified as

$$\frac{d}{d\tau_\nu}(I_\nu e^{\tau_\nu}) = S_\nu e^{\tau_\nu} \tag{2.5}$$

Now, integrating between the optical path 0 and $\tau_{\nu'}$ using Equation 2.5 can be written as

$$\int_0^{\tau_\nu} d(I_\nu e^{\tau_\nu}) = \int_0^{\tau_\nu} S_\nu e^{\tau'_\nu} d\tau'_\nu \tag{2.6}$$

leading to the general solution of the radiative transfer equation in Equation 2.2. Over an entire column gas, the equation now becomes

$$I_\nu = I_\nu(0)e^{-\tau_\nu} + \int_0^{\tau_\nu} e^{-(\tau_\nu - \tau'_\nu)} S_\nu(\tau'_\nu) d\tau'_\nu \tag{2.7}$$

where $I_\nu(0)$ is the initial intensity of the radiation. Therefore,

$$I_\nu(\tau_\nu) = I_\nu(0)e^{-\tau_\nu} + S_\nu(1 - e^{-\tau_\nu}) \tag{2.8}$$

In the absence of radiation from a source, $I_\nu(0) = 0$. The equation becomes

$$I_\nu(\tau_\nu) = S_\nu(1 - e^{-\tau_\nu}) \tag{2.9}$$

If the medium is optically thick $\tau_\nu \gg 1$ and $e^{-\tau_\nu}$ in Equation 2.9 becomes very small. This implies that photons emitted by the medium will easily be absorbed (see Figure 2.4). The $e^{-\tau_\nu}$ becomes negligible and only the source function is what is usually seen. In the optically thin case, $\tau_\nu \ll 1$, therefore, the photons will pass through the medium without being absorbed. An observer will only see radiation emitting towards the observer's line of sight. Satisfying these conditions, for the optical thick case, Equation 2.9 becomes

$$I_\nu = S_\nu \tag{2.10}$$

and for the optically thin case,

$$I_\nu = S_\nu \tau_\nu \tag{2.11}$$

2.3.2 Population inversion and amplification

Consider a collection of molecules with two energy levels, the intensity received is given by Equation 2.9. The populations in the lower and upper states are denoted by n_l and n_u, respectively. The change in the energy levels is $h\nu_0$ and the statistical weights of the levels are g_l and g_u. When a photon with energy $h\nu_0$ passes through the medium of the homogeneous slab, the molecules/atoms of the medium will interact with the photon either through absorption or via stimulated emission. This will result in transitions characterised by the Einstein coefficients (A_{ul}, B_{ul} and B_{lu}) for emission, absorption and stimulated emission.

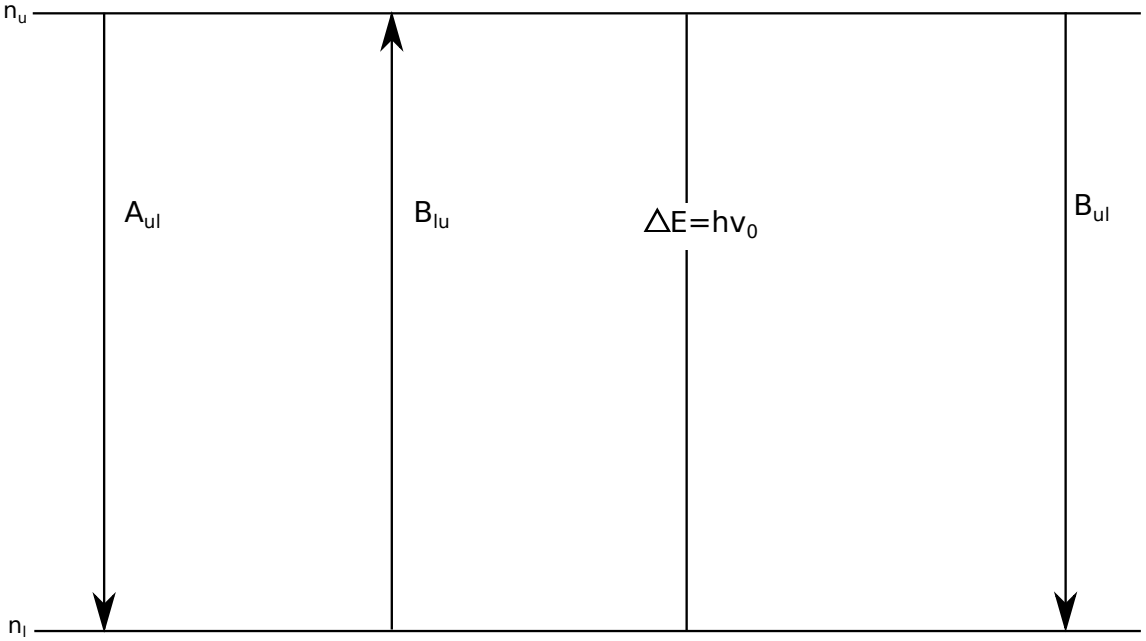

FIGURE 2.5: A schematic diagram showing the transition between states of a system having two energy levels and the Einstein coefficients (A_{ul}, B_{ul} and B_{lu}). A_ul is the coefficient of spontaneous emission, B_ul is the radiative absorption and B_lu is the stimulated emission.

Figure 2.5 shows the transitions between the lower (l) and upper (u) states of the system with energy levels and the level populations are denoted by n_l and n_u, respectively. The statistical weights of the levels are $g_{\rm l}$ and $g_{\rm u}$.

In thermodynamic equilibrium, the number of absorbed photons are equal to the number of emitted photons. The number density in the upper states having energy $h\nu_0$ above the lower state from Stahler & Palla (2005) is

$$\frac{n_u}{n_l} = \frac{g_u}{g_l} e^{\left(-\frac{h\nu_0}{kT_{ex}}\right)} \tag{2.12}$$

where k is the Boltzmann constant and $T_{\rm ex}$ is the excitation temperature of the two energy level system (i.e. the temperature at which populations in the energy levels will have a Boltzmann distribution).

Using the Boltzmann relation in Equation 2.12, the energy density is given by

$$U_\nu = \frac{\frac{A_{ul}}{B_{ul}}}{\frac{g_l B_{lu}}{g_u B_{ul}} e^{\left(-\frac{h\nu_0}{kT_{ex}}\right)} - 1} \tag{2.13}$$

Using the Planck law in frequency, the energy density is

$$U_\nu = \frac{8\pi h\nu_0^3}{c^3} \frac{1}{\left(e^{\frac{h\nu_0}{kT_{ex}}} - 1\right)} \tag{2.14}$$

where c is the speed of light. The Einstein coefficients are related by

$$A_{ul} = \left(\frac{8\pi h\nu_0^3}{c^3}\right) B_{ul}, \qquad B_{lu} = \frac{g_u}{g_l} B_{ul} \tag{2.15}$$

From Equation 2.13, the term $\frac{h\nu_0}{kT_{\rm ex}}$ becomes very small at lower frequencies, that is $\frac{h\nu_0}{kT_{\rm ex}} < 1$. Thus, stimulated emission will exceed absorption processes in radio frequency domain as opposed absorption dominating in the ultraviolet and optical. Assuming a local thermodynamic equilibrium (LTE),

$$n_u B_{ul} U_\nu > n_l B_{lu} U_\nu \tag{2.16}$$

where $n_{\rm u} B_{\rm ul} U_\nu$ is the number of downward transitions per unit volume per unit time and $n_{\rm l} B_{\rm lu} U_\nu$ is the number of induced upward transitions per unit volume per unit time due to the presence of radiation with energy density U_ν.

Assuming $B_{\rm lu} U_\nu = B_{\rm ul} U_\nu$, then $n_{\rm u} > n_{\rm l}$. This is the condition for population inversion to occur, thus, using Equation 2.12, we get

$$\frac{n_u}{n_l} > \frac{g_u}{g_l} \tag{2.17}$$

The above equation results in a negative absorption coefficient and a negative excitation temperature, thus, the intensity is amplified as it propagates through a path length of the medium. This implies that the final intensity (I_ν) will greater than the initial intensity from the radiation source (I_0) and $k_\nu < 0$, when the incident radiation is amplified.

In masers, apart from the absorption coefficient being negative, $T_{\rm ex}$ as well as the optical depth are all negative which causes the radiation to be amplified exponentially in the maser cloud. At the beginning of the amplification process, the intensity growth becomes exponential and the

maser is termed as *unsaturated*. The growth becomes rapid until stimulated emission leads to less molecules in the excited states and there is no longer exponential amplification. This results in maser saturation where the intensity increases linearly with path length. Unsaturated masers have narrower line profiles as compared to saturated masers which make them to have small apparent sizes of spots.

2.3.3 Pumping

Stimulated and spontaneous emission cause losses in population inversion, therefore a mechanism is required to maintain the inversion against such losses. There are two forms of pumping mechanisms found in masers that maintain the population inversion so that the molecules can cascade to the masing level. This process is best described using a system having three or more energy levels. The mechanisms are as a result of collisional excitation processes or radiative processes which account for the population distribution in the energy level (Elitzur, 1982). In the collisional excitation mechanism, the molecule collides with another molecule such that there is overpopulation in $n_{\rm u}$. Due to the high tendency of gas thermalisation, there is a high amount of collisions causing the masers to be destroyed quickly in this kind of pumping (Elitzur, 1982). H_2O masers are known to be collisionally excited (Elitzur & Fuqua, 1989; Strel'Nitskii, 1974).

For the radiative pumping, more molecules in the lower energy level are pumped to $n_{\rm u}$ and cascaded to $n_{\rm l}$ due to the presence of radiations (Elitzur, 1982). This kind of pumping is seen in the class II CH_3OH and mainline OH masers. These masers give information on the presence of the emission responsible for their pumping mechanism in the SFR. The details of the pumping scheme are seen from the efficiency of the population inversion (η_p), given as

$$\eta_p = \frac{p_u - p_l}{p_l + p_u} \tag{2.18}$$

In Equation 2.18, $p_{\rm u}$ and $p_{\rm l}$ are the pump rates of the upper and lower states, respectively. The rate at which molecules are excited to the upper state or de-excited to the lower state is what is termed as pump rate. When $p_{\rm u} > p_{\rm l}$, it means that more molecules are promoted to the upper level than the lower level and $\eta_p > 0$. This will lead to population inversion, a requirement to form a maser. When $p_{\rm u} \leq p_{\rm l}$, $\eta_p \leq 0$ and no maser will be formed.

Chapter 3

Observational techniques in radio astronomy

The study of compact molecular masers has been one of the essential ways to effectively explore HMSF in complex regions (Gray, 1999). Owing to the advancement of radio astronomy observations, compact masers can easily be observed through the use of radio telescopes. This chapter will describe some of the radio astronomy observational techniques which is relevant to the HartRAO 26 m single-dish telescope and the KAT-7 interferometer.

3.1 Description of radio telescopes

Radio telescopes are used as single-dish telescopes or arrays of telescopes (Ryle et al., 1959). The arrays of telescopes are referred to as an interferometer. Radio telescopes are generally categorised into various types based on their mounts with which the telescope rotate about their axes, the way they focus radio emission, the reflector types and their observing frequencies. The mounts include the equatorial and altitude-azimuth mount types (Condon & Ransom, 2016). The equatorial mount radio telescopes rotate about the declination and polar axes while the altitude-azimuth mount telescopes rotate about azimuth and elevation axes. All single-dish radio telescopes are generally made up of a reflector dish, a receiver system, a back-end system for detecting and correlating voltages as well as a computer system for recording and storing data. These components will be discussed in the subsections below.

3.1.1 Dish

The dish, also known as aperture (D) of a radio telescope has a collecting surface area (A_e) that is made of reflective material or a composite (Foley et al., 2016). There are various dish shapes, however, the most familiar types are the parabolic dish telescopes. They have reflector systems that are used to focus radio waves and are designed to follow the Prime focus, Cassegrain or Gregorian reflector designs (Napier, 1999). The Cassegrain and offset Gregorian types are dual-reflector systems. They have a primary and secondary reflector. The difference is that the Cassegrain has a hyperbolic convex secondary reflector surface while the Gregorian has an ellipsoid concave secondary reflector surface design. The Prime focus has no secondary reflector, rather, it has a receiver hosted right at the focus of the primary reflector. Figure 3.1 is an illustration of the geometries of the various reflector systems.

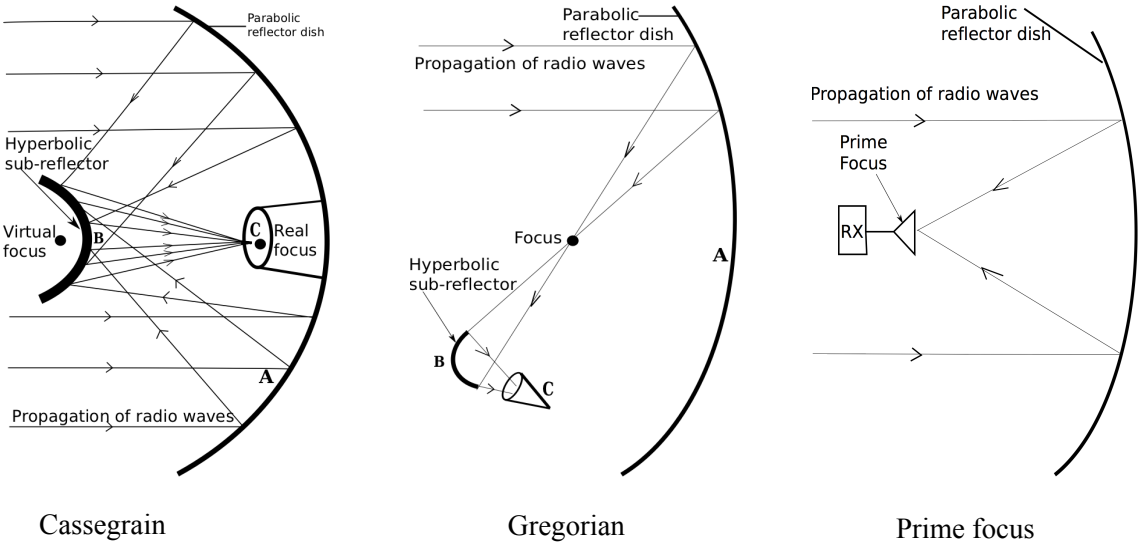

FIGURE 3.1: An illustration of various antenna reflector layouts adopted from Garett (2015).

3.1.2 Receivers

Radio telescopes consist of front-end and back-end receiver systems. A typical front-end system consists of feeds, connecting cables and mixers and amplifiers. The feed is an opening where the signals reflected by the secondary reflector is focused into and transmitted over to the receiver. The feed transforms the radio signals into a waveguide mode for easy transmission in the waveguide cable. Splitters or Orthomode transducers (OMT) separate the signals into two orthogonal polarisations. In the mixers, the radio signals are combined with a local oscillator (LO) to convert the polarised signals into intermediate frequencies (IF) signals. The frequency conversion is done to minimise signal loss and to easily manipulate the signal as it passes through the receiver system. IF amplifier amplifies the signal at the new frequency which then gets filtered and down-converted to a lower frequency signal. This signal is easy to sample and detect at the detector. To eliminate additional noise (discussed in section 3.2) from being introduced to the output signals, the front-ends are usually cooled.

The receiver back-ends for a single-dish radio telescope comprise of a detector (usually a Square-Law detector), spectrometer and or a radiometer. A square-law detector outputs the noise power response per frequency bandwidth ($\Delta\nu$) which is proportional to the system temperature. The spectrometer is made up of a single sideband receiver where spectral line information is stored. The spectrometer measures the total power in each band channel and outputs the spectrum of spectral line observations. Unlike the spectrometer, the radiometer averages over the frequency range for continuum measurements and works as a square-law detector.

3.2 Detection with radio telescopes

A radio source produces a signal power (P) over a frequency bandwidth ($\Delta\nu$). From the Nyquist theorem, received by the antenna from the source is given as

$$P_\nu = kT\Delta_\nu \tag{3.1}$$

where k is the Boltzmann constant. effective collecting area (A_e) of a dish is an important property of radio telescopes. The power received from a radio-emitting field unto the effective area compared to the actual area of the dish is called *antenna efficiency*. Part of the signal can be 'lost' when the reflector surface is poorly designed. Also, radio signals are not reflected into the receiver depending on the perfection of the parabola shape. A radio-emitting source with a uniform T_b occupies a solid angle Ω referred to as the source beam. The antenna also has a beam (θ) which is less or equivalent to the power illuminated from the emitting radio source. The main beam of an antenna is the power pattern from the central peak of the source. Source emissions measured outside of the main lobe are known as side lobes. The width of the antenna beam is inversely proportional to the aperture size in units of wavelengths.

The total output power measured by a radio telescope has a fraction of external noise contributions as well as noise contributions from the electronics of the telescope. These noise contributions are collectively termed as the system temperature and it is given as

$$T_{sys} = T_{CMB} + T_{loss} + T_{atm} + T_{cal} + T_{spill} + T_R \tag{3.2}$$

where T_{CMB}=2.7 K is the noise emission from the big bang cosmic microwave background (CMB) at all frequencies, T_{atm} is the temperatures from atmospheric effect, T_{cal} is the noise contribution due to injected noise from the noise diode, T_{loss} is the noise contribution due to loss in the feed, T_R is the receiver temperature and T_{spill} is the noise contribution due to sun's radiation and radiation from the ground being scattered into the feed-horn and resulting in a spillover temperature. The system temperature can be expressed in terms of System Equivalent Flux Density (SEFD) which is defined by Wrobel & Walker (1999) as the flux density a source would deliver with the same power. The SEFD is expressed as

$$SEFD = \frac{2\eta k T_{sys}}{A_e} \tag{3.3}$$

where η is the efficiency of the antenna. The factor of 2 accounts for half of the total signal received by a single polarisation of the receiver from an unpolarised source. The SEFD can be measured observationally by determining the fractional increase in power obtained when on and of a source of known flux density.

The antenna temperature (T_A) is the signal power transferred to the receiver by the antenna from the source. It relates the power in Equation 3.1 as

$$T_A = \frac{P_\nu}{k} = \frac{A_e S_\nu}{2k} \tag{3.4}$$

In general, the flux of a source emission can be expressed as

$$S[Jy] = \frac{kT_A}{A_e} \times 10^{-26} [W\, Hz^{-1}\, m^{-2}] \tag{3.5}$$

From equation 3.5, the flux density of the source is related to the antenna temperature T_A. The antenna temperature is related to the brightness temperature as follows;

$$T_A = \frac{T_B}{\lambda^2} \int_{4\pi} A_e(\theta, \phi) d\Omega \tag{3.6}$$

For an unresolved source, that is a source which extends over a very small solid angle (Ω), $T_{\rm A} \propto T_{\rm B}$ multiplied by a beam filling factor. The beam filling factor is the ratio of source angular size to the beam size of the telescope. The signal to noise (S/N) is given by

$$S/N = \frac{S_\nu \sqrt{\Delta\nu_N t}}{SEFD} \tag{3.7}$$

where t is the integration time. The detection limit of any source is three times S/N or greater.

The ability of a radio telescope to measure and detect very faint sources is termed as sensitivity measured in Kelvin per Jansky ($\mathrm{K\,Jy^{-1}}$). The main effects influencing the sensitivity of radio telescopes are the size and efficiency of the reflector dish as well as the receiver efficiency. The sensitivity (K) of a telescope is directly proportional to the effective $A_{\rm e}$ of the dish from Equation 3.3 as

$$K = \frac{\eta A_e}{2k} \tag{3.8}$$

The sensitivity in units of Jansky per Kelvin [$\mathrm{Jy\,K^{-1}}$] is determined by the size and perfection of a telescope's aperture and the surface accuracy, that is the degree of surface irregularities of the antenna dish. Bigger telescopes have better sensitivity than smaller telescopes.

3.3 Design and signal processing of the HartRAO 26 m telescope

The 26 m single-dish radio telescope is shown in Figure 3.2. It is located at the Hartebeesthoek Radio Astronomy Observatory in South Africa and was built in 1961 by Blaw Knox (Combrinck & Nickola, 2001). The telescope is an equatorial mount telescope, tracking in right ascension (RA) and declination (DEC). This makes it easier to counteract the Earth's rotation to track radio sources at any angle. The telescope operates at frequency ranges between 1 GHz and 23 GHz, making it good for the observation of masers such as the class II methanol and the mainline OH masers. It has a good reflectivity with a surface tolerance of 0.5 mm RMS.

The HartRAO 26 m single-dish telescope is a Cassegrain-type telescope having primary and secondary reflectors. The secondary reflector is a hyperbolic sub-reflector with a size of about 3 m. It is mounted at the focal opening positioned centrally and symmetrically at the center of the parabolic dish reflector. The sub-reflector is held up by four pod legs called a quadrupod and it can be adjusted to focus on different receivers during observations. At the centre of the HartRAO 26 m telescope is the feed cone where a waveguide is connected the receiver system. The receivers are designed to observe at a wavelength of 1.3, 2.5, 3.5, 4.5, 6, 13 or 18 cm. With the wide range of wavelength bands, a sub-band can be selected for a specific observing frequency.

The 4.5 cm receiver is used to observe the 6.7 GHz methanol masers (see Table 3.1 for the specifications). The receiver is fully polarised and contains splitters for splitting the radio signals

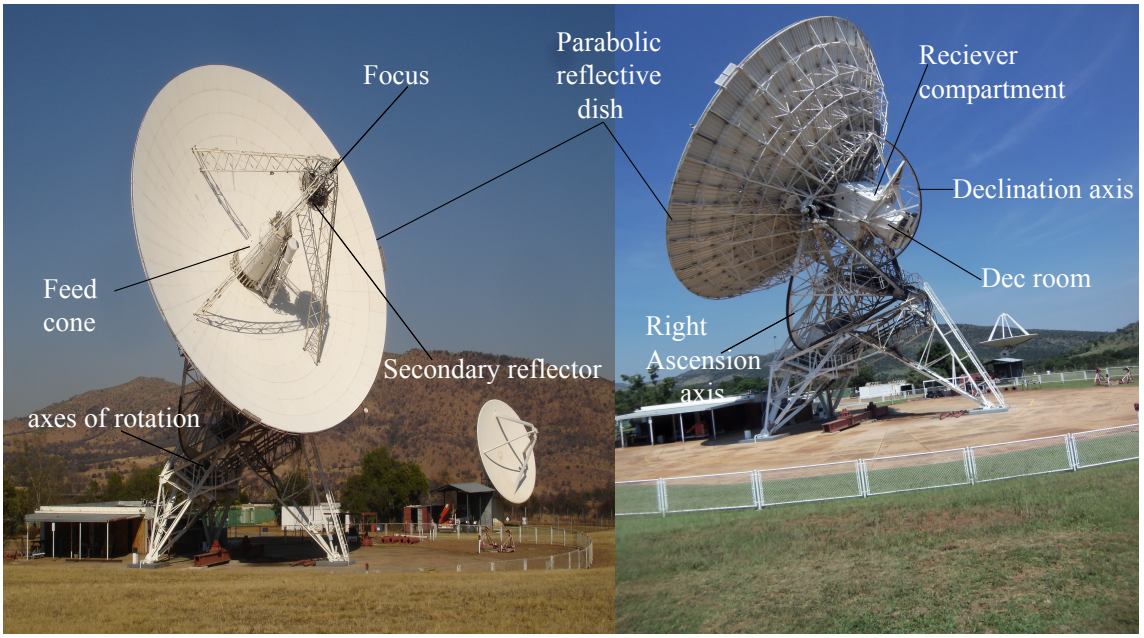

FIGURE 3.2: Image of the HartRAO 26 m single telescope.
Image credit: http://www.hartro.ac.za/gallery/index.html

into left and right circular polarisation (LCP and RCP) components. The 4.5 cm receiver has a cryogenic system that minimises the noise contributions from the system electronics by cooling the Low Noise Amplifier (LNA) and other front-end electronics. Since the system temperature introduces uncertainty in the flux density measurements which affects the amplitude of the spectra, any high variations found in the $T_{\rm sys}$ must be discarded. Directly below the receivers is an instrumentation room, known as the Dec room. Radio signals are mixed down to a lower frequency in the Dec room to reduce transmission loss and transmitted over coaxial cable to the control room. Back-end detectors are installed in the control room.

TABLE 3.1: The 26 m single-dish telescope receiver specifications

Specifications	6.7 GHz methanol maser
Band	4.5 cm (between C and X)
$T_{\rm sys}$	< 70 K
Polarization of feed	L & R circular
Frequency	$6008 - 6682$ MHz
Total Bandwidth (MHz)	660
Angular resolution	$\sim 1'$
Focus	4.6 m

3.3.1 Signal processing and calibrations

Emission from a radio-emitting field gets onto the reflective dish where it is then reflected onto the hyperbolic sub-reflector, focused into a feed-horn and then to the receiver. Each polarisation component is detected separately inside the receiver which gives the radio signals. Before the signals reache the Dec room, they are again filtered using a bandpass filter in the post-amplifier. Outputs from the Dec room are conveyed by co-axial cable to the control room where there are a spectrometer and a radiometer. The noise from the electronics is detected with the detector. Depending on the type of radio source emission that was observed, the radiometer or the spectrometer is used for further analysis. At 4.5 cm, the spectrum output from the spectrometer spans over 1024 channels. For OH masers, the frequency bandwidth is usually 1 MHz since the masers have narrow bandwidths. For calibration purposes, the voltage measured from a receiver is squared in the radiometer to enhance the S/N expressed in Equation 3.7. The final output, that is the total power from the back-ends, is further transferred to the computer for data capturing.

3.3.2 Noise diode and receiver calibration

Prior to observation, a once-off calibration procedure is done on the telescope instrument and online systems to test for inconsistencies in the electronics. Calibration is done on the receiver to determine the noise temperatures of the receiver. The noise contribution from the sky is usually small compared to the receiver noise. Since the T_{sys} comprise of all the noise contribution both from the sky and the system, it is necessary to establish a calibration scale.

For the 4.5 cm receiver, a small amount of noise from a calibrator whose value is known in Kelvins is injected into the system while the noise calibrator is on and off. In this case, the noise diode is the calibrator noise and the temperature is denoted by T_{ND}. Once the diode temperature is known, the power is converted from counts to Kelvin. Figure 3.3 is a display of temperature measured by the HartRAO 26 m telescope when the noise diode is fired on and off. From the image, assuming a noise diode temperature of 14 K, a conversion factor (T_c) measured in units of [counts K^{-1}] is given by;

$$T_c = \frac{\Delta P_{Tot}}{T_{ND}} \tag{3.9}$$

Therefore, the number of counts in every 1 K is equivalent to the value of the conversion factor. In this instance, a conversion value of 9101 $\pm$ 123 counts K^{-1} is obtained. This value will then be used to calibrate the antenna temperature.

3.4 Observational techniques of single-dish telescope

3.4.1 Pointing observations

A number of factors can affect the pointing accuracy of a telescope. This includes the antenna surface and support structure deformation. The deformation is caused by gravity or thermal expansion and contraction of the structure. For the 26 m telescope, gravitational deformation is a

major factor. Pointing correction is essential, especially for the HartRAO 26 m telescope because inaccurate pointing induces variations in the measured total power from the radio source. Thus, to minimise atmospheric effects and gravitational deformation, observations are always carried out within 45 ° of zenith whenever possible.

To determine the pointing error, spectra scans are done at half-power points to the North (N), South (S) and centre of a source in continuum or spectral line mode. The peak profile of the source is usually shifted from the antenna beam centre. A pointing correction is done to determine by how far the profile peak is shifted from the beam centre. Also, the T_A is obtained from this observation for the cardinal points and the "on-source" observations.

3.4.2 Continuum observation and flux density calibration

To determine the sensitivity of the radio telescope, a radio source that is bright with known flux density is observed. Such a radio source is called a *calibrator* source. Calibrator sources are continuum or point sources with non-variable flux density over a period of time and are usually resolved or unresolved sources. With this observation, the telescope is pointed ahead of the calibrator's path. The source is allowed to drift through the beam of the telescope and the radiometer is used in this case. In single-dish radio telescope observation like that of HartRAO, the sensitivity is also referred to as Point Source Sensitivity (PSS). This is temperature-based and given as

$$PSS = \frac{S_\nu/2}{K_s T_A} \tag{3.10}$$

where the S_ν in Equation 3.10 is the observed flux from a radio source and is in units of Jy. k_s is the source correction factor. For point sources, $k_s = 1$. The PSS is however, measured in $\mathrm{Jy\,K^{-1}}$per polarisation. Therefore, the PSS for each polarisation is calculated from the antenna temperature

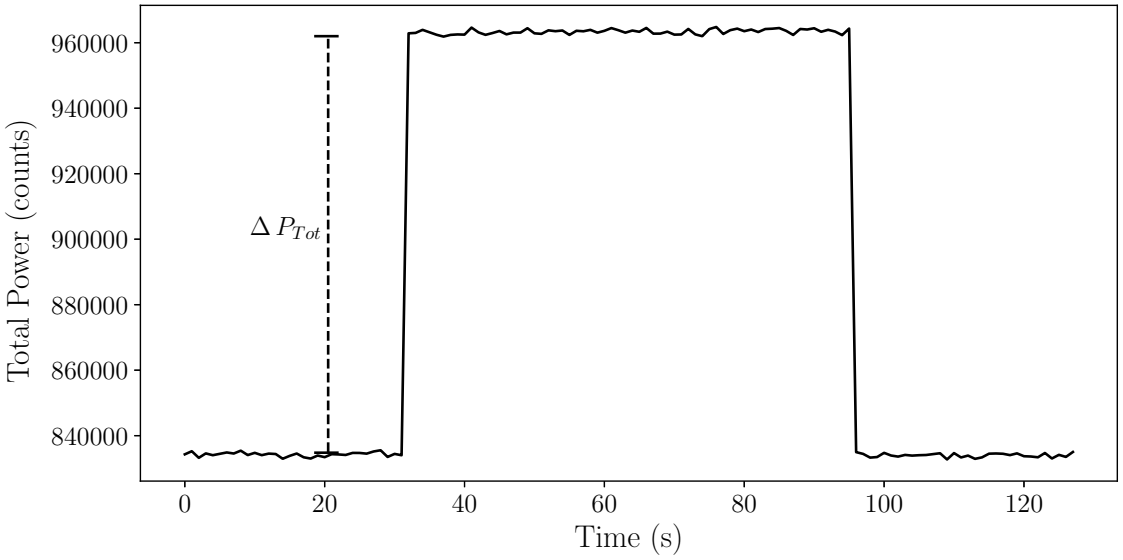

FIGURE 3.3: The measure of the jump between system counts and the fired noise diode. The undulated segments indicate the measurement of noise contribution to the system, whereas, the step change represents the on and off of the noise diode.

as a function of each polarisation. The polarisation can be left and right circular polarisation (LCP and RCP) and the antenna temperature for the PSS is $T_{\rm A}^{\rm lcp}$, $T_{\rm A}^{\rm rcp}$. The PSS values of the calibrator sources are calculated using Equation 3.10. The PSS values are multiplied with the $\rm T_A$ after multiplication by the noise diode conversion factor in order to convert to flux density in units of Jy. A correction factor for the pointing offset is also applied to the source flux density.

3.4.3 Bandpass correction

The bandpass of the total power spectrum is not usually flat due to poor antenna response and instability of the system noise. To eliminate any of such variations, a baseline correction must be done. In a single-dish observation like the HartRAO 26 m telescope, the following spectral line techniques can be employed for the bandpass correction.

1. **Position switching**
   When using this technique, a target is observed "on-source" and the received signal is compared to the signal measured when the telescope is moved to a relative position in the sky. Similar time is used for the on and off-source positions. This observing mode easily cancels out baseline effects because atmospheric effects are rejected while the best spectral baselines are achieved.

2. **Frequency switching**
   For frequency switching observations, the LO is switched such that the line spectrum is shifted to the left and right (positive and negative features) sides of the spectral bandpass. To improve the signal-to-noise, the two line spectrum found to the left and right of the bandpass are combined. With the frequency switching technique, frequency-dependent effects are corrected and systemic offsets are removed. The technique is used for sources with angular sizes smaller than the beam size of the telescope. It is also efficient for observing narrow-lines and to identify spectral lines (Matthews et al., 2004).

3.5 Design and signal processing of the KAT-7

The KAT-7 follows a different design from the HartRAO 26 m single-dish telescope. It is a seven-element radio interferometer built in the Karoo region of South Africa. The KAT-7 is a precursor of the MeerKAT 64 dishes. Each telescope of the KAT-7 is 12 m in diameter and pairs up with another to form a baseline. The KAT-7 baselines range from a minimum of 26 m to a maximum of 185 m (see Figure 3.4).

The KAT-7 is an altitude-azimuth mount radio telescope and has an offset prime focus configuration. The composite dish has a surface tolerance of 1.5 mm root-mean-square (RMS). For detailed specification of the KAT-7 design, see Foley et al. (2016). The KAT-7 uses a dual-heterodyne receiver system, consisting of waveguides, ortho-mode transducer (OMT), LNA and cryostats for cooling the LNA (Lehmensiek & Theron, 2011). During the signal processing, the LNA is kept as cold as possible at all times. To cool the LNA, KAT-7 uses the Stirling pump cooling system with a temperature of 77 K. The Stirling pump extends the cooling processes in the

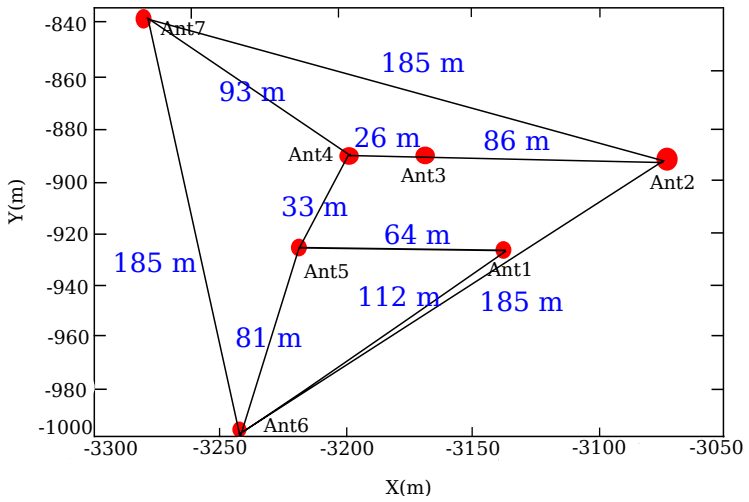

FIGURE 3.4: The layout of the 7-dish Karoo Array Telescope baselines.

receiver system and this mechanism increases the thermal efficiency to obtain high power output. Specifications of the KAT-7 receiver at 18 cm are also listed in Table 3.2.

3.5.1 Processing radio signals with the KAT-7

Radio signals are converged from the primary reflector to the prime focus into the horn. The OMT separates the signals into two linear polarisations, vertical (V) and horizontal (H) linear polarisations and down-converted to RF signals. Multiplying the radio signals by a gain factor increases the S/N, thus, the signals are scaled at the coupler (see Figure 4 of Foley et al., 2016). Afterwards, they transmitted to a bandpass filter where they are filtered into a specified frequency band of interest. With the required frequency band, the signals continue to an attenuator. Inside this compartment, the radio signal is down-converted to radio frequencies. The total power obtained from each polarisation is converted into optical signals. The output is transported over a $\sim$ 5.6 km fibre-optic cable to minimise the risk of introducing radio frequency interferences (RFI). Calibration on the flux, phase and delays are done at this stage (see Section 3.6). The optical signals are then converted back to low-frequency signals that go into a computing container. Inside the container, they are heterodyned by a downconverter into an IF signal with a bandwidth of 400 MHz. The IF signals are mixed with local oscillators, digitised and then multiplied by the bandwidth correlator. The process of multiplying the signals at the correlator is known as cross-correlation.

TABLE 3.2: KAT-7 receiver specifications

Band	L
T_{sys}	$< 35\,K$
Polarization of feed	Dual Linear
Frequency	1.2 GHz –1.95 GHz
Total Bandwidth	750 MHz

For maser observations such as that of the mainline OH masers, the maser monitoring correlator mode is used with a processed bandwidth of 1.5625 MHz and a processed channel width of 381 Hz. The correlated measurements are stored as visibility measurement sets.

3.6 Fundamentals of radio interferometric observation and imaging

Radio telescopes measure time-varying voltages of astronomical radio sources. Recognising two point sources as separate sources requires a telescope with higher angular resolution ($\theta \sim \frac{\lambda}{D}$, where θ is the smallest separation between the point sources). Due to the large beams of single-dish telescopes, the separation cannot be identified. This will mean the point source will not be resolved. However, using two small telescopes help to increase the resolving power of the instrument, therefore, the separation can be seen. Combining two or more telescopes produce interference patterns by cross-correlating voltages at the correlator. The cross-correlated voltages at different locations is a spatial coherence, also called complex visibilities. The visibilities comprise of both amplitude and phase.

To correct for anomalies in the phase and amplitude and also find the flux density of the target source, calibrator sources are observed. A flux calibrator is used to determine the flux density of the target source. A phase calibrator is then used to correct for time-invariant gain and phase variations as a function of frequency. The phase calibrator is also known as the complex gain calibrator. The solutions are then transferred to the target source to correct for sky and system gain variations during the tracking. These procedures are known as calibration procedures. In this way, changes of the sky and telescope can be determined during the observations (Fomalont & Perley, 1999).

In interferometry, Fourier analysis is used to create images of target source from the visibility measurements. The images provide detailed information which cannot be achieved by the use of only a single-dish telescope. Interferometers sample in the Fourier domain (*u,v*) than in the image domain (*l,m*). Sampling in Fourier space has made it easy to estimate for the observed sky brightness distribution ($I^{\rm obs}$(l,m)) obtained from the observed visibilities ($V^{\rm obs}$(u,v)). $I^{\rm obs}$(l,m) is a 2-D Fourier transform of $V^{\rm obs}$(u,v). The complex visibility is defined as

$$V^{obs}(u,v) = \int I^{sky}(l,m) e^{-2\pi i(ul+vm)} \tag{3.11}$$

From observed visibilities, the sky brightness is the Fourier Transform of the observed complex visibility and the *uv*-plane. The sky brightness can be estimated using Equation. 3.11. From the calibration, $I^{\rm sky}$(l,m) can be determined from creating a *dirty image* (I^D). Convolving the sky intensity distribution (I^{sky}) of the source with the synthesized beam or the point spread function of the dirty beam (I^{PSF}(l,m)) results in the dirty image. From the Van Cittert-Zernike Theorem, an image can be formed through the summation of cosine fringes in the Fourier sampling space (Thompson et al., 2017a; Zernike, 1938). The imaging equation is given by

$$I^D(l,m) = I^{PSF}(l,m) * I^{sky}(l,m) \tag{3.12}$$

To account for the $I^{sky}(l,m)$, there is a need to estimate for the visibility function ($S(\mathrm{u},\mathrm{v})$, $V^{\mathrm{obs}}(\mathrm{u},\mathrm{v})$) in the un-sampled regions of the *uv*-plane. $S(\mathrm{u},\mathrm{v})$ is the sampling function of the sky or the *uv* coverage. The radio telescopes form *uv* tracks by tracking the projected target in the *lm* plane. The *uv* tracks, also known as *uv* coverage correspond to the frequency sampling over the *uv*-plane as the Earth rotates or the number of baselines per the array of telescope. Assuming few telescopes are used for observation, there will be gaps in the *uv*-plane sampling. These can be minimised by increasing the number of telescopes in the interferometer for observation as well as the integration time for the observation. Taking a Fourier Transform of the *uv* coverage results in the synthesized beam. The synthesized beam is also known as the instrument response and must be deconvolved (subtracted) for the flux density measurements to be correct. Additionally, increasing the integration time for the observation improves the S/N (see Section A.1).

In order to also achieve a smooth image of the true sky, the dirty beam is subtracted from the synthesized image through a process of deconvolution. The imaging process is more of a convolution approach while the deconvolution is a reconstruction of the image to get the I^{sky} as shown in Figure 3.5.

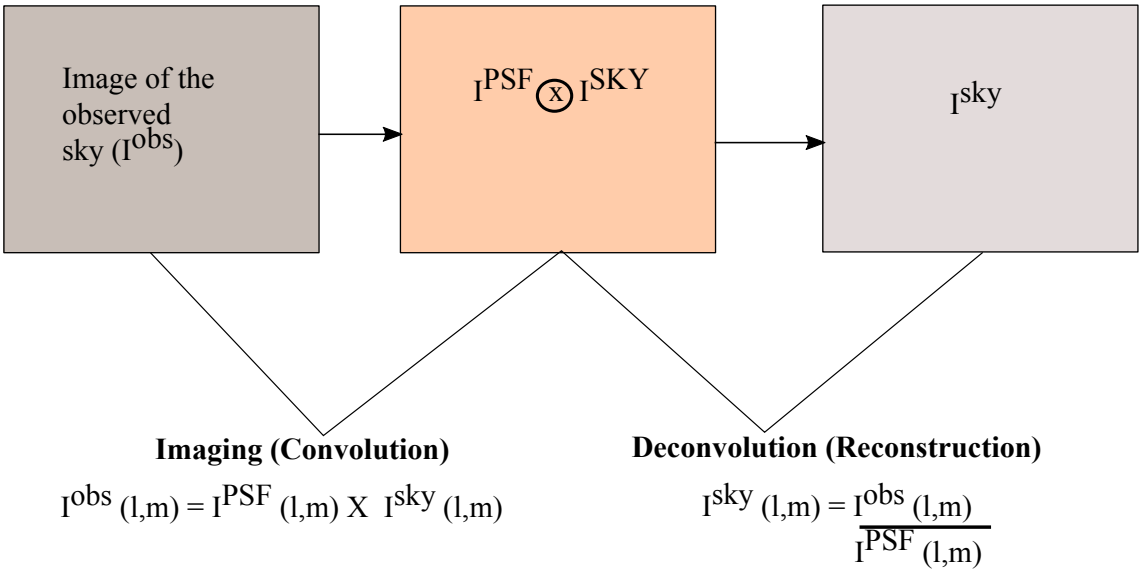

FIGURE 3.5: A representation of Deconvolution principles

3.6.1 Deconvolution and imaging

CLEAN algorithms are possible means of carrying out deconvolution. There are quite a number of CLEAN algorithms but for this work, we will present on the Classic CLEAN algorithm (see Garsden et al., 2015, and references therein for details on other CLEAN algorithms).

The 1st Generation Calibration Classic CLEAN algorithm was proposed by Högbom (1974). Also referred to as the Högbom CLEAN, it is an iterative deconvolution and the procedures are implemented to produce images through deconvolution as follows:

1. Construct a dirty image and a point spread function of the observation. The number of iterations set by the deconvolution must be set to zero.

2. Find the point where the peak flux is located.

3. Multiply the PSF by a flux value and subtract from the dirty image. This will result in a delta function of the sky model. We stated that the FT of a point source is a delta function. Repeat steps (2) and (3) until we reach a stopping criterion. The input parameters of the stopping criterion consider the loop gain and the number of iterations. The gain controls the amount of flux to be subtracted through each iteration. The loop gain is set somewhere between 0 and 1. If no flux is subtracted, the loop gain is equal to zero and with this, we are sure that there will be no deconvolution. If the gain is set to 0.2, it means for every iteration, 20% of the flux will be subtracted until it reaches the noise level which is set as the threshold. The number of iterations is stopped using the stopping criteria.

4. Convolve the sky model (I^m) with a CLEAN beam (C) and add the residual image to finally restore the image. The CLEAN beam is a 2D Gaussian fit to the main lobe of the PSF. CLEAN uses the number of iteration to implement the process until the stopping criteria or the total known flux has been reached. Once all the flux has been subtracted, no further CLEAN is needed. The restored image (I^{Res}) can finally be described in Equation. 3.13;

$$I^{Res} = I^m_{clean} * C + R \tag{3.13}$$

where, (I^m_{clean}) is the sky model composed of CLEAN components, (R) the residual and in this case, * is the deconvolution operator.

There are also variants of the Högbom's method; the Clark (1980) and the Schwab (1984) CLEAN implementations. Clark's method considers the deconvolution first in the visibility domain after a partial image is created from the Högbom's deconvolution. Additionally, it makes use of the Fast Fourier Transform (FFT) algorithm to speed the convolution process. After the process, an Inverse Fourier Transform (IFT) is applied to convert the visibility back to an image domain. This is quite useful over a very large field of view. The Schwab (1984) CLEAN method is more advanced compared to Clark's method. This method caters for any aliasing artefact in the PSF. The disadvantage of this method is that it is computationally expensive and uses high memory.

Chapter 4

Observations and data processing

4.1 Target source

G339.62-0.12, shown in Figure 4.1, is a complex radio source. Inspection of the Spitzer 24 μm image suggests G339.62-0.121 be located North-West to a filamentary structure associated with a larger molecular cloud. The cloud has been classified as a bipolar nebular containing both G339.62-0.12 and G339.58-0.12 clumps (Samal et al., 2018). The latter harbours a methanol maser found at about 2.4′ from G339.62-0.12 (Caswell et al., 2011).

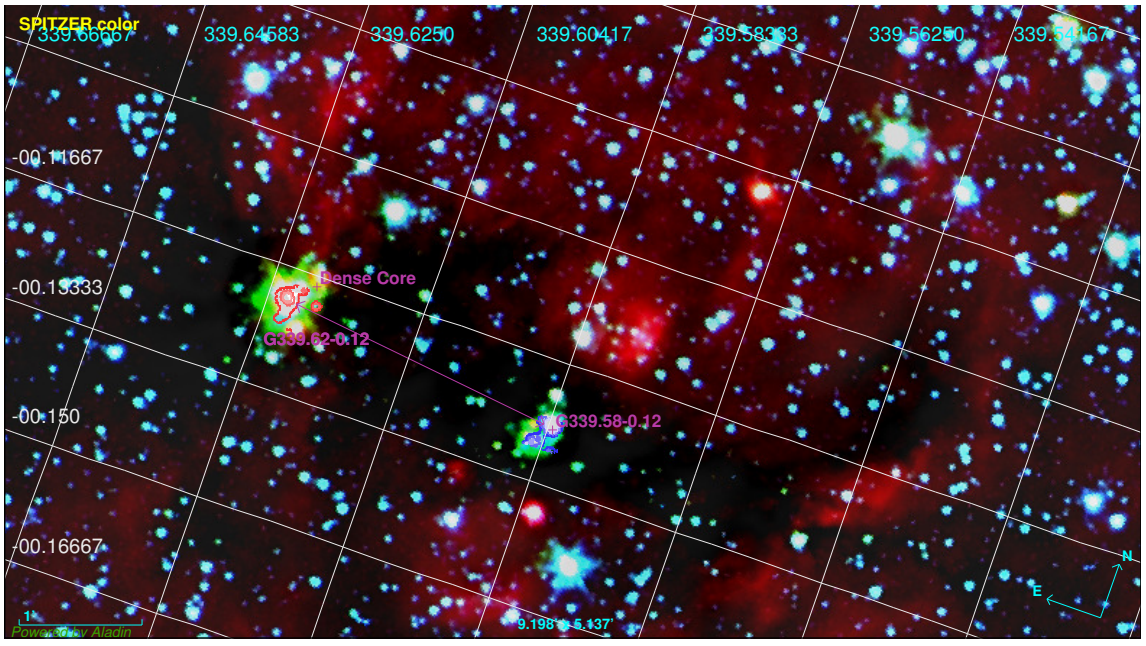

FIGURE 4.1: An image of G339.62-0.12. The IRDC image at 24 μm is represented in black. The Spitzer 24 μm are represented in green, yellow, red and blue colours. The contours are the 2MASS images of the region.

A dense core, AGAL339.62-0.12 has also been identified to be associated with G339.62-0.121 (Contreras et al., 2013). The dense core has $V_{\rm lsr}$ = -34.2 km s^{-1} although Giannetti et al. (2014) derived a $V_{\rm lsr}$ = -34.58 km s^{-1} from C^{17}O(3-2) data. Using the systemic velocity of AGAL339.623-0.122 and the method of Reid et al. (2009), the near kinematic distance to G339.622-0.121 is found to be 2.6 kpc (Green & McClure-Griffiths, 2011). G339.62-0.12 coincides with the IRAS source 16424-4531 where Bronfman et al. (1996) observed CS(2-1) emission in the direction of the IRAS source. Bronfman et al. (1996) suggested that G339.62-0.12 is associated with a H II region having a velocity of -33.2 km s^{-1}. The observations of Purser et al. (2016) reveal G339.62-0.12 to have east and west lobe components of free-free emission. The east lobe coincides with OH maser emission

whereas the brightest methanol maser observed by Caswell (1996) is found 2 arcsecs from the centre of the lobe. The peak H_2 column density of G339.62-0.12 is found to be 2.4 $\times 10^{23}$ cm^{-2} and the dust temperature is $\sim$21 K (Samal et al., 2018).

A bright YSO is found 1 arcsec away from the bright methanol maser in G339.62-0.12 (Samal et al., 2018). To the South and North of G339.62-0.12 are two nearby diffuse regions found at 0.25 pc and 0.21 pc from the position of the YSO. The south extended diffuse region contains an early B star that may be the main source of heating the dust in the region (Samal et al., 2018). This diffuse region is observed as an ionised gas with dust temperature T_d >21 K. A cold region to the west of G339.62-0.12 has a dust temperature ranging between 17 K and 19 K (Samal et al., 2018).

The G339.62-0.12 radio source was initially described as a radio quiet source, having a luminosity of 5.2×10^4 L$_\odot$ (Mottram et al., 2011). This implies that the source is in the early phase and the UC H II region has not developed (Navarete et al., 2015). According to Walsh et al. (1998), no UC H II region has been observed towards G339.62-0.12. Purser et al. (2016) derived a luminosity of 1.9×10^4 L$_\odot$, which is an indication of a high-mass star forming in the region.

4.2 The HartRAO observations and calibrations

In this work, the HartRAO 26 m single-dish telescope was used to observe the 6.7 GHz CH_3OH masers from February 2013 to July 2015. The cryogenically cooled 4.5 cm full polarisation receiver was used, thus, the observations were carried out in the LCP and RCP. The masers were observed once every week or once in two weeks with a velocity resolution of 0.044 km s^{-1}. However, the observation time was increased to two or three times per observation or daily observing when the maser was seen to rapidly vary. The total on-source observation integration time was 420 seconds per epoch.

4.2.1 Continuum drift scans and calibration

For this observation, Virgo A was observed and used as a flux calibrator. It has been measured to have frequency ranges of 1408-10550 MHz (see Table 5 of Ott et al., 1994). Due to the stable flux density Virgo A has, it has been proposed as an ideal calibrator at frequencies above 5 GHz (Baars et al., 1977). This means Virgo A has small fluctuations in flux distribution over time. Further, Virgo A is also "believed" to have about 5% absolute accuracy Baars et al. (1977).

4.2.1.1 Flux density calibration

Using the drift scans (see Section 3.4.1), three scans were made on the Virgo A for each polarisation as shown in Figure 4.2. Two of the drift scans were North and South of the target source at half power beam points. Table 4.1 gives the list of parameters used in this work for Virgo A. The calibrator source was observed for 90 seconds for each observation.

TABLE 4.1: Parameters of the Virgo A calibrator observations at 6.7 GHz.

Virgo A	
Longitude	187.7°
Latitude	12.2°
Backend type	Radiometer
Central frequency of backend (MHz)	6668.518
Bandwidth of backend (MHz)	16
RCP Noise diode Temp (K)	14
LCP Noise diode Temp (K)	21

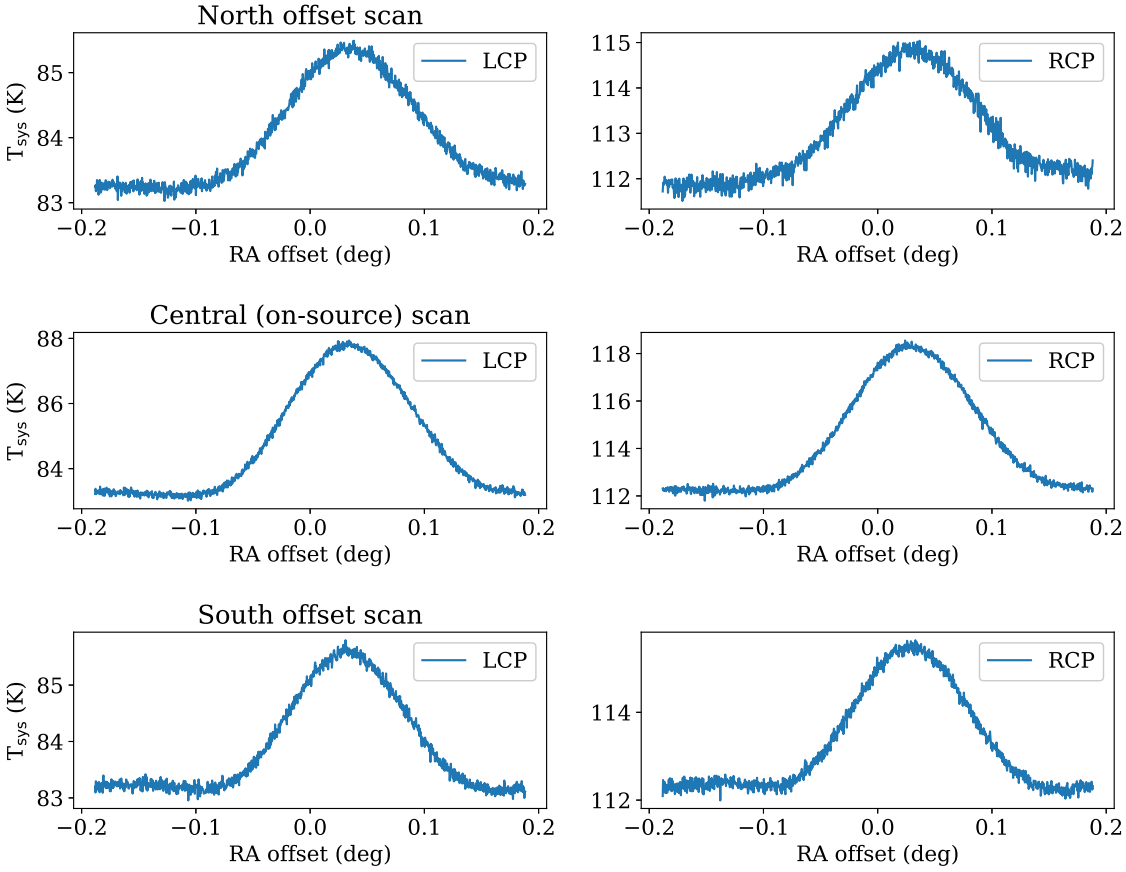

FIGURE 4.2: Example of drift scans for Virgo A

4.2.1.2 Baseline and amplitude correction

The baseline is set by fitting a linear function or as it was in some cases, a second-order polynomial through the center of the beam. The peak in each scan is assumed to have a Gaussian profile. Thus, the peak of each scan in the North-South direction was fit with a Gaussian beam, having a width equivalent to the half-power beamwidth of the telescope beam. This was done to determine the pointing offsets between the source and the centre of the telescope beam. The product of the pointing correction factor and driftscan antenna temperature gives the corrected antenna temperature as shown in Figure 4.3.

The corrected T_A was used to determine the PSS values for the LCP and RCP, they were found to be 6.1 Jy K^{-1} and 4.5 Jy K^{-1} respectively (see Figure 4.4). Each polarisation PSS was expected to remain almost at a constant value but slight variations were identified in the PSS. This may be due to internal system variations or possibly deformation of the reflective surface of the dish at low elevations. During observations, pointing corrections were done periodically. This means every artificial variation in the time-series was annulled whenever the pointing was correctly done.

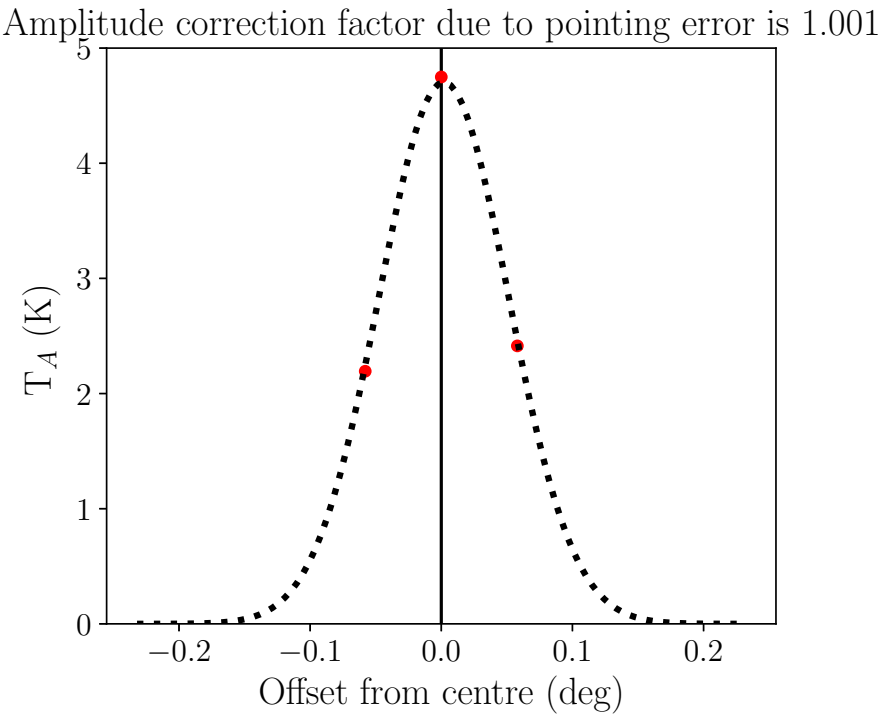

FIGURE 4.3: Pointing correction factor applied to the continuum source peak amplitude. The red dots represent the measured antenna temperature from the cardinal points. The amplitude is the result after the pointing correction factor has been applied.

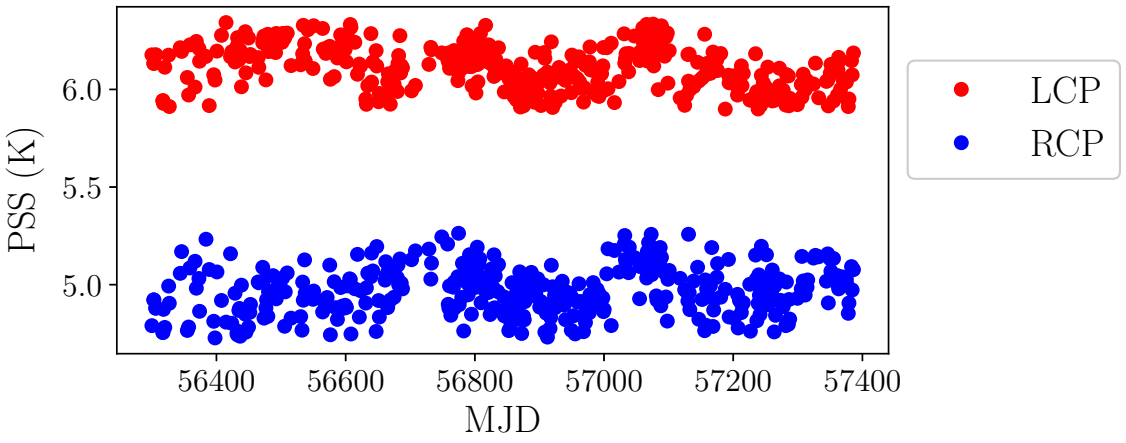

FIGURE 4.4: The Point Source Sensitivity of the 26 m telescope from the left and right circular polarisations of Virgo A.

4.2.2 The 6.7 GHz CH_3OH maser observations and calibration

Prior to the frequency switched observations, five pointing offset observations were done in spectral line mode on G339.62-0.12 (see Figure 4.5). The pointing checks were made within 3 arcmins at 6.7 GHz. The strongest maser peak found between -33.2 $km\,s^{-1}$ and -32.5 $km\,s^{-1}$ was used to find the pointing errors by fitting the top of the peak with second-order polynomial as shown in Figure 4.6.

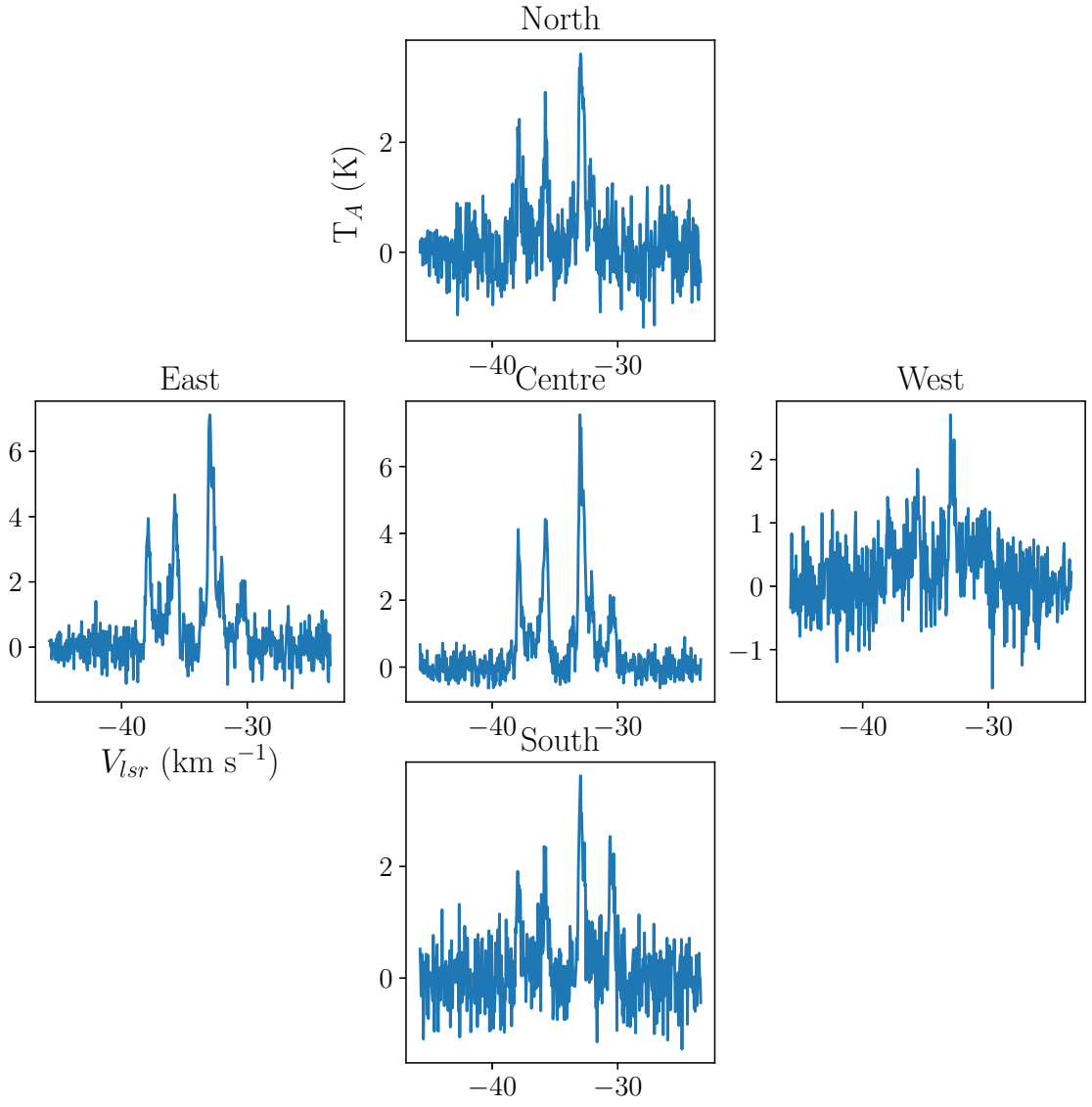

FIGURE 4.5: The pointing observation of the G339.62-0.12 maser source.

The North and South scans were averaged in order to correct for bandpass. This was also done for the East and West scans. Afterwards, the pointing for the North-South and the East-West were determined (see Figure 4.7) and the pointing correction was applied to the spectra of the maser. To obtain the total power, a reference spectrum measured from the frequency switching technique was subtracted from the original spectrum. This corrects for variations in the bandpass and flattens the baselines.

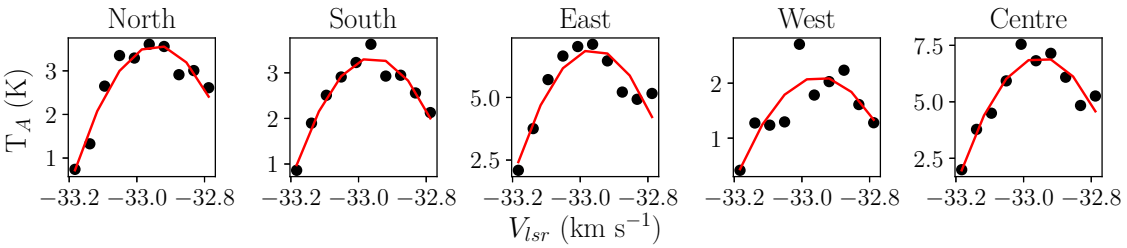

FIGURE 4.6: Fitting the topmost of the peak power measured at the half-power points. The black dots represent the maser amplitude and the red line is the polynomial fit used.

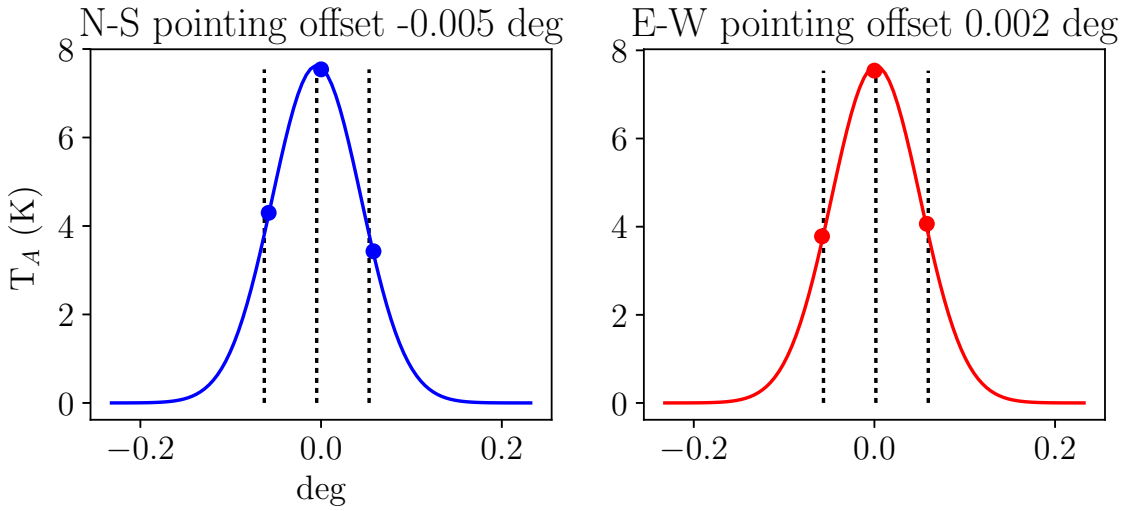

FIGURE 4.7: Pointing offsets measured to correct for pointing errors from zenith. The N-S pointing is slightly off as compared the E-W pointing.

The 6.7 GHz methanol masers were observed using the frequency-switching technique described in Section 3.4.3. Figure 4.8 shows the maser spectra obtained with the frequency switching observation. From the figure, a spike-like feature was found at the centre of the bandpass. This could be effects of the spectrometer. That channel was removed before further data processing was carried out.

4.2.2.1 The 6.7 GHz CH_3OH maser data reduction

The polarised spectra with common velocities were summed together as shown in Figure 4.9. The baselines are then linearly fit to correct for the remaining variations in the baseline (see Figure 4.10). Lastly, the maser spectrum for each polarisation was multiplied with the measured PSS to convert from antenna temperature in [K] to flux density in units of [Jy]. Each polarisation, however, contains half of the total intensity. Hence, the polarised spectra were finally added together to obtain the overall total flux density spectrum (see Section 5.2 for further discussion). The 6.7 GHz methanol maser data reduction was done using python programming packages.

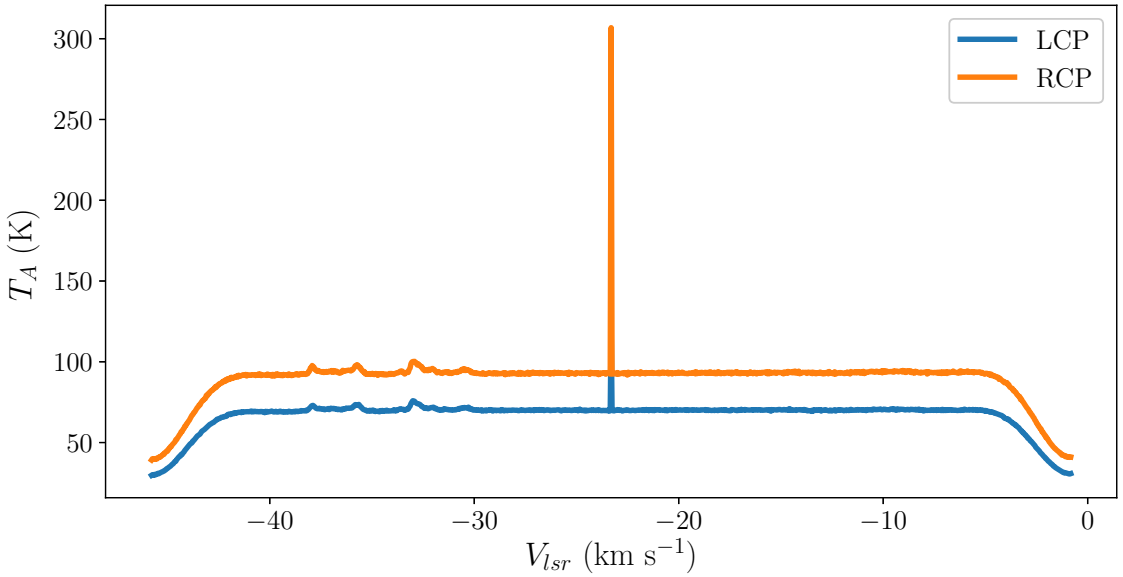

(A) Maser spectra at the left side of the bandpass

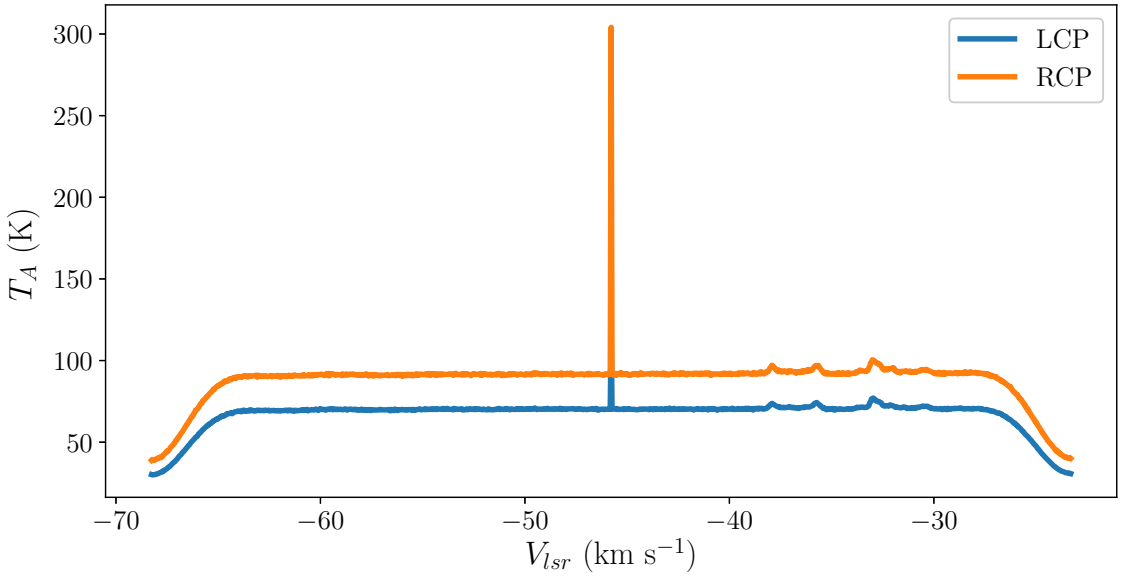

(B) Maser spectrum shifted to the right side of the bandpass

FIGURE 4.8: Spectra of maser frequency switched pair in each polarisation.

4.3 KAT-7 observations, calibration and data reduction

Using the KAT-7 interferometer, the mainline hydroxyl masers were monitored on weekly basis. The observations were centred at rest frequencies of 1665.40184 MHz and 1667.35903 MHz respectively and the velocity resolution was 0.068 km s^{-1}. The c16n2M4k correlator mode was used (Goedhart et al., 2019), considering the stokes I correlation. The primary beam, the synthesized beam, the angular resolution and the field of view have been calculated in Appendix B.1.

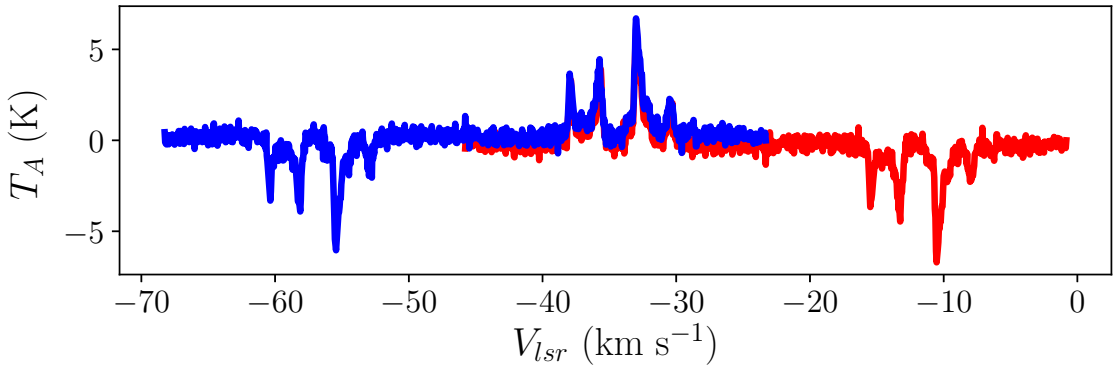

FIGURE 4.9: Frequency switched pairs from the LCP and RCP having common velocities were summed to obtain the overall total power. The blue represents the spectrum for the RCP and the red spectrum is the RCP.

First, the PKS 1934-638 and PKS 1722-55 calibrator sources were observed. PKS 1934-638 was observed as a flux and bandpass calibrator while PKS 1722-55 observed as a gain calibrator. The flux calibrator was observed every few hours and then followed by the gain calibrator which was observed once every 15 minutes. The target source was then observed followed by the gain calibrator again. The cycle was repeated throughout the observation. Using standard flagging methods, corrupt scans and bad datasets from the visibility measurement sets were discarded. Channels of no interest ,as well as visibilities with spurious amplitudes, were also removed to eliminate RFI. Furthermore, baselines showing random phase or high variation in the phase were flagged. Also, as part of data editing and calibrations, bandpass correction was done to eliminate both system and atmospheric errors along the frequency axis of observation. This was followed

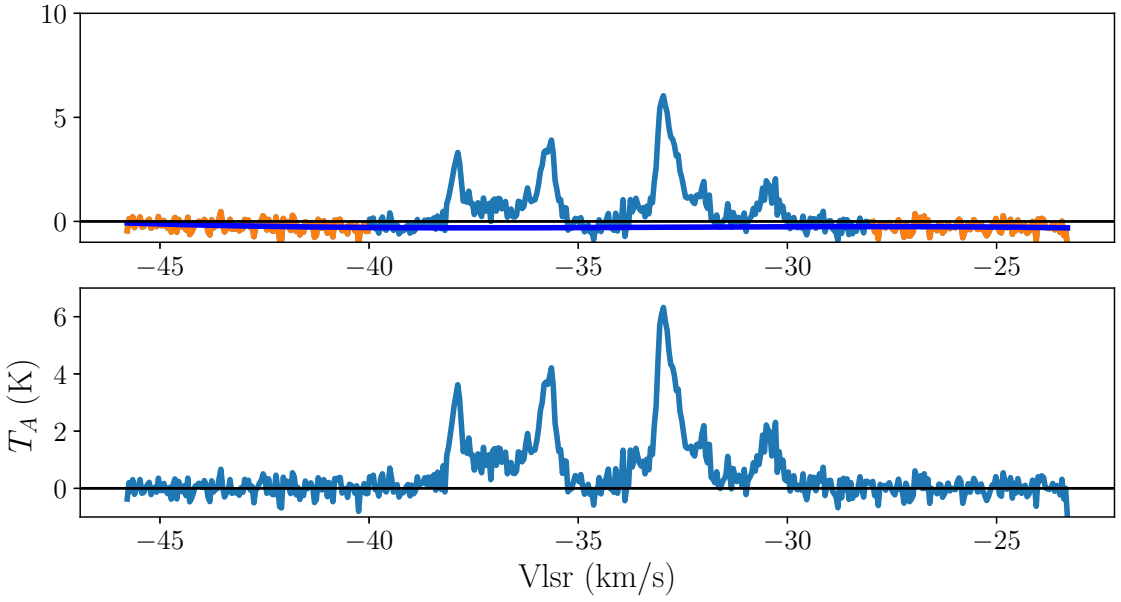

FIGURE 4.10: Correcting for baseline effects using emission-free channels. The black horizontal line in the panels is to show that the emission free channels will have almost zero temperature once the baselines are corrected.

with flux calibration where the flux scale of Perley & Taylor (1999) was adopted to correctly scale the amplitude of PKS 1934-638. Gain calibration was done thereafter. Using the technique of self-calibration (SelfCal), a sky model for PKS 1722-55 was constructed. The SelfCal method removed most of the field effects as shown in the top right panel of Figure 4.11. By plotting the gain solutions, the amplitude and phase coherence were checked and the solutions transferred to the G339.62-0.12 target field. All calibration and part of the data reduction were done using the Common Astronomy Software Application (CASA) versions 4.6 and 4.7 respectively.

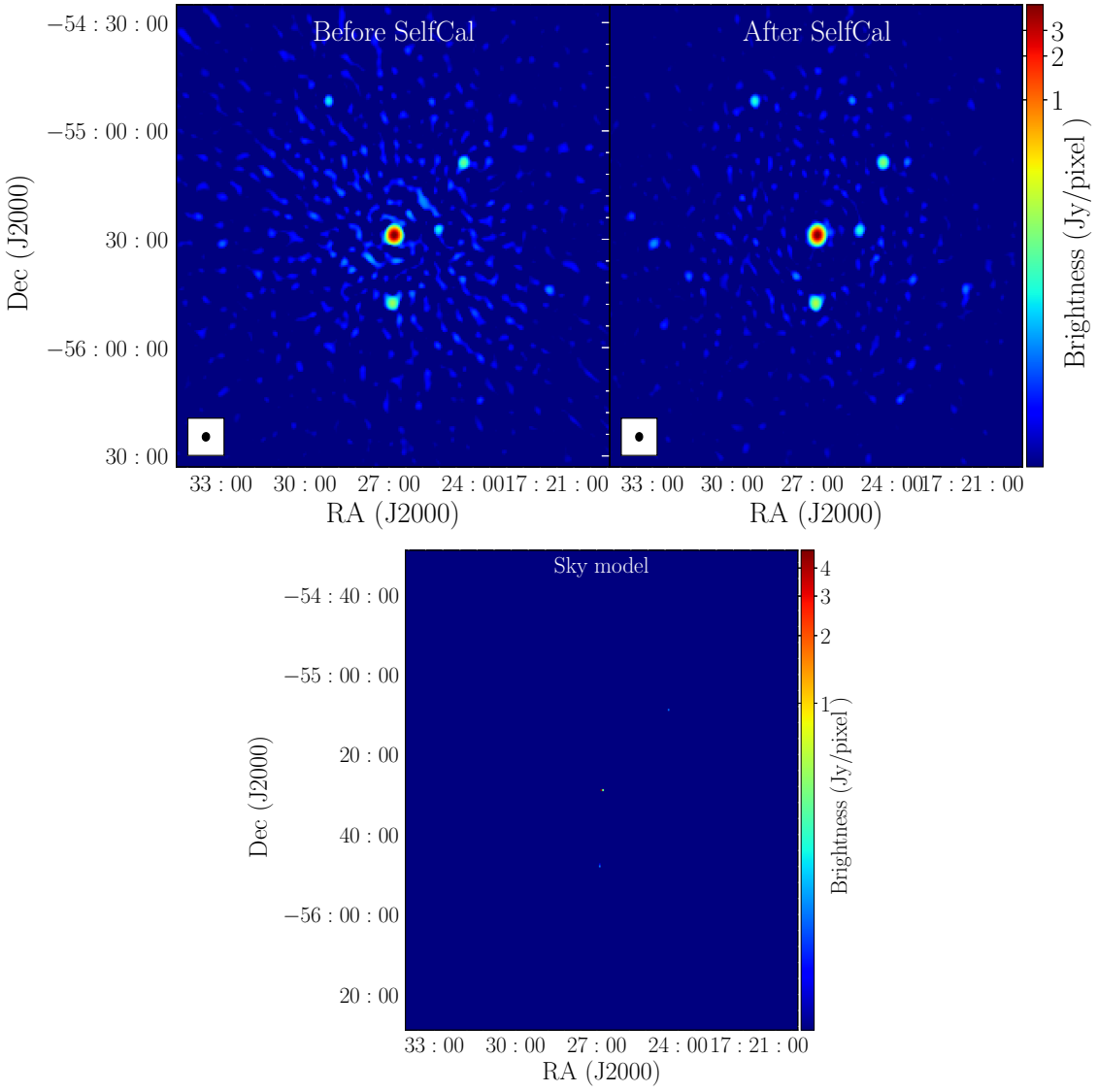

FIGURE 4.11: The top panels are the generated sky images before and after self-calibration. The bottom panel is the sky model of PKS 1722-55. It is worth noting that the model is for a gain calibrator and will be used to calibrate the G339.62-0.12 maser field.

The G339.62-0.12 maser field was calibrated following the calibration procedures described in section 3.6.1. Through the method of interpolation, the gain solutions were transferred to the G339.62-0.12 target field. Using the **cvel** task in CASA, doppler-shift correction was also done as well as re-gridding and transforming the data into a reference frame. This converts the maser frequency channels into velocity channels measured in $\mathrm{km\,s^{-1}}$ by re-aligning the emission in the channels while the velocity rest frame is also set to Local Standard of Rest defined in the Kinematics (LSRK). The datasets were then re-gridded into spectra windows having a total of 2000 channels. The KAT-7 data contained both the continuum and the maser emission. Therefore, by applying linear interpolation to emission-free velocity channels, the baseline for the continuum was established and then subtracted. Thus, the final calibrated data was separated into two datasets for imaging, one having the subtracted continuum and the other containing the maser emission. This was to enhance the dynamic range of the maser field as well as to easily identify the maser lines.

The data cubes for the continuum and the maser lines were generated through the process of deconvolution already described in Section 3.6.1. In this work, the Högbom CLEAN algorithm was used for the deep automated imaging. For the radio continuum, all available observation of the continuum data sets were combined before imaging. The frequency channel to be mapped onto the image was set to multi-frequency scale (mfs) in the **mode** parameter of CLEAN. The mfs is ideal for combined channels, making it easier to identify extended or compact sources (Cornwell, 2008). From the continuum data cube, the peak flux of the individual source was subtracted to a threshold of 5 $\mathrm{mJybeam^{-1}}$ of the RMS noise level to establish an image for the continuum.

For the maser data cube, a general CLEANing was first run to deconvolve the maser sources. This generated initial sets of the CLEAN image components. From the residual image, individual masers in the field were identified and masked for CLEANing. Since OH masers could have very narrow bandwidth, the following criteria were used to select sources in the field that were considered to be maser sources.

- Components that consistently show emission over the velocity range of $\geq 1\,\mathrm{km\,s^{-1}}$ and also appear within not less than three channels were considered as maser sources.
- Components having a flux density of $> 5\,\sigma$ were considered to be maser sources.
- The RA and DEC for the identified field sources were compared with those in the literature and using the SIMBAD Astronomical Database.

The **mask** parameter was also used to confine CLEAN to search for components in specific regions where the masers were identified. The size of the masked box used was 300.8×250.3 arcsecs, signifying more than four times that of the primary beam. It can be deduced from this that the masers were unresolved. The threshold value to stop CLEANing was set to three times of the r.m.s noise (3σ). A default gain parameter of 0.1 was used with 500 iterations for each CLEANing cycle. Parameters such as the cell size and image size specific to CLEAN have been calculated in the Appendix B.1.

Chapter 5

Results and analysis

Goedhart et al. (2014) have reported that the methanol masers associated with G339.62-0.12 are periodic. However, it is not known if the mainline OH masers associated with this source is also periodic or not. This is the first search of periodicity in the mainline OH masers associated with G339.62-0.12. This chapter is divided into three main sections. The first section (Section 5.1) presents the imaging procedures and the imaging results of the 18 cm radio continuum and the mainline OH masers. The second part is divided into two (Sections 5.2 & 5.3) where the spectra and time-series analyses are described. Section 5.4, which is the third section presents the periodic analyses done for some selected maser features.

5.1 Image of the field of view

5.1.1 The radio continuum

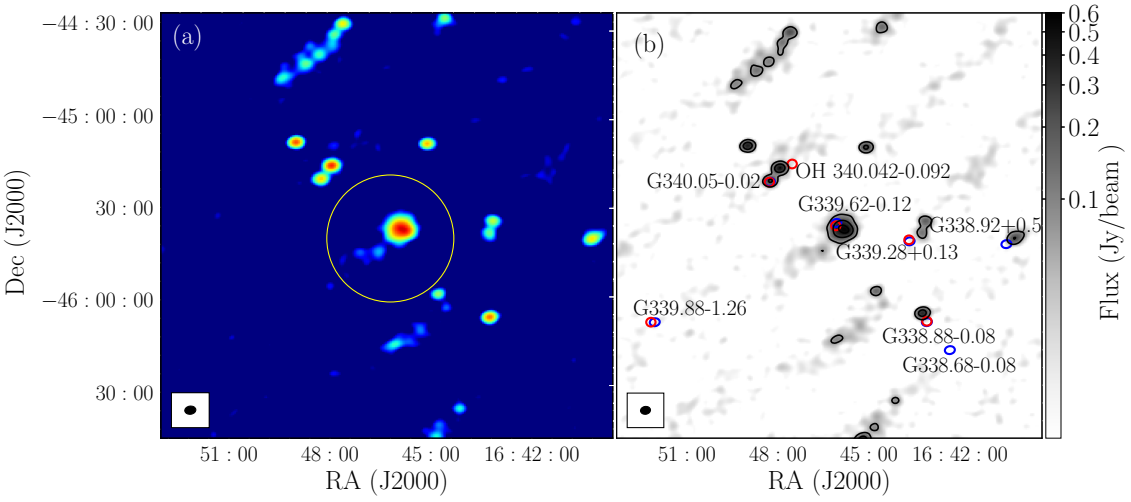

FIGURE 5.1: The radio continuum and OH maser emission in the field of view. (a) shows a multi-coloured scale of the radio continuum and (b) shows the overlay of OH masers on the radio continuum. The OH masers are represented with coloured o where the size of a maser ring is the size of the synthesized beam. The contour lines represent the levels at [0.152, 0.52, 1.01] mJy/beam.

Figure 5.1(a) shows a colour map of the radio continuum produced from the KAT-7 CLEAN continuum data. From the image, it is seen that various compact sources are present and are resolved in the radio continuum. The central source, G339.62-0.12, has been circled using a yellow ring. The other regions are seen to be compact compared to G339.62-0.12. It is also seen that a trailing tail-like structure is connected to G339.62-0.12. This might be an indication of quite a lot of HMSF activity occurring. Examples of such activities have already been discussed in Section 4.1.

TABLE 5.1: Hydroxyl maser sources detected in the field.

OH Maser frequency	Source name	RA (J2000) (h m s)	DEC (J2000) (° ′ ″)	Vel range ($km\,s^{-1}$)	Peak flux ($Jy\,beam^{-1}$)
1665 MHz	G339.62−0.12	16 46 08.3	−45 35 46.4	−30 −39	48.13
	G339.92+0.56	16 40 34.9	− 45 42 27.5	−60 −64	2.28
	G338.68−0.08	16 42 22.1	−46 18 37.1	−19 −22	1.31
	G338.88−0.08	16 43 09.2	−46 09 08.3	−33 −38	4.13
	G339.28+0.13	16 43 46.8	−45 41 16.2	−70 −73	0.60
	G340.05−0.24	16 48 10.9	−45 22 08.6	−48 −59	102.63
	G339.88−1.26	16 52 03.1	−46 09 29.4	−32.6 −36	3
1667 MHz	G339.62−0.12	16 46 06.1	−45 36 40.1	−30 −39	11.91
	OH339.28+0.13	16 43 44.8	−45 42 54.5	−73 −74	1.13
	G338.88−0.08	16 43 08.3	−46 09 26.1	−33 −34	1.35
	OH340.04−0.09	16 47 31.5	−45 16 25.1	−9.9 −10.9	0.89
	G340.05−0.24	16 48 11.6	−45 21 30.1	−47.8 −57	7.9
	G339.88−1.26	16 52 03.9	−46 08 17.6	−35 −37	1.96

Column 1: The observed OH maser transitions. Column 2: The Galactic names of the maser regions. Column 3 & 4: The positions of the individual sources using units of RA and DEC. Column 5: The velocity ranges of maser emission shown in the imaging field. Column 6: The maximum brightness extracted from the image.

From Figure 5.1(b), the blue and red rings are the 1665 and 1667 MHz OH masers, respectively. Each maser emitting region identified in the field of view has been listed in Table 5.1. At a spatial resolution of 30 arcsec, individual maser spots could not be resolved. The reason for this is due to the smaller size of the masing region compared to the size of the synthesized beam. Only one maser spot is therefore seen for the individual maser transition in each region. It is worth noting that the OH maser emission occurs in certain regions at both 1665 and 1667 MHz. Also, not all the OH masers have associated radio continuum. However, the masers associated with G339.62-0.12 and G340.05-0.24 are well projected onto the continuum. Others are found offset or have no radio continuum.

TABLE 5.2: Example of parameters obtained from the G339.62-0.12 image.

OH Maser	Vel ($km\,s^{-1}$)	flux (Jy)	r.m.s (Jy)	Synthesized beam bmin (mas)	bmaj (mas)	bpa (°)	Area ($(''')^2$)
1665 MHz	-37.50	47.86	0.17	0.18	0.28	$-87.8\pm$ 3.1	51.57
1667 MHz	-36.45	12.98	0.19	0.16	0.25	-77.1 ± 2.9	47.14

Column:1 The mainline OH masers. Column 2: The velocity of the peak amplitude. Column 3: Maximum flux density of the peak after CLEANing. Column 4: The residual noise levels after deconvolution. Column 5: The FWHM of the minor and major axes and the position angle of the image component size convolved with the beam. The area of the synthesized beam is also given for each OH maser transition.

5.1.2 The OH masers associated with G339.62-0.12

For the mainline OH masers associated with G339.62-0.12, we present the results obtained from the imaging. Figures 5.2 to 5.4 are examples of images obtained from the CLEANing procedure. From the restored CLEAN image in Figure 5.2, the 1665 MHz OH masers (right panel) are brighter than the 1667 MHz OH masers (left panel). This is generally the case for interstellar OH masers found in Galactic SFR (Caswell & Haynes, 1987; Cohen, 1989). Table 5.2 is a summary of information obtained from the restored CLEAN image for the 1665 and 1667 MHz OH. For every velocity channel containing a maser emission, a 2-D elliptical Gaussian having the equivalent dimensions as the synthesize beam was fit to the region of emission in each emission channel. In this way, we were able to obtain the source emission in flux density units of the channels of emission. The observation time was converted to Modified Julian Day (MJD).

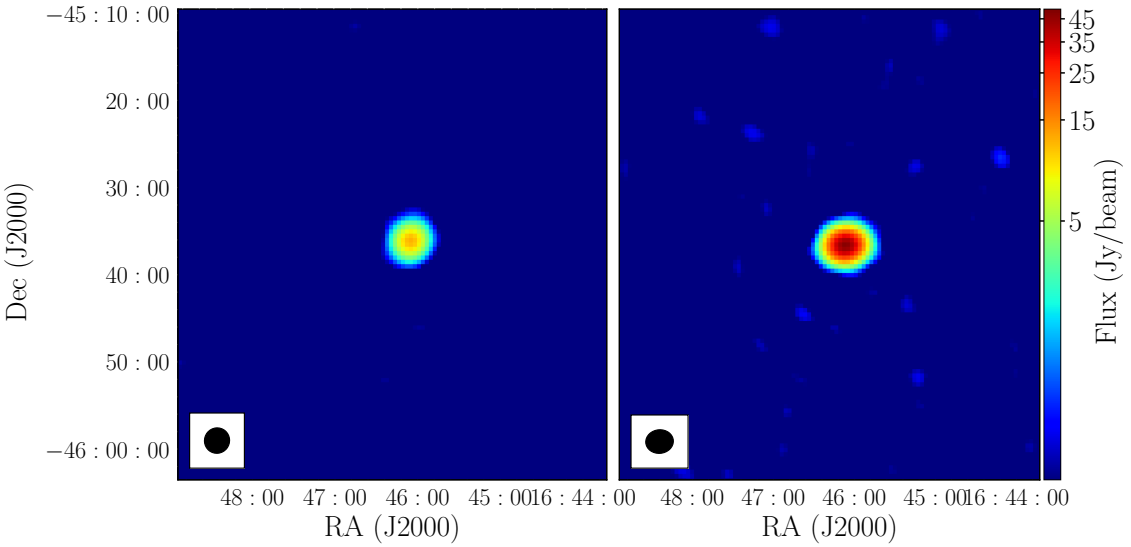

FIGURE 5.2: Restored CLEAN images for the 1667 MHz OH (left panel) and 1665 MHz OH masers (right panel).

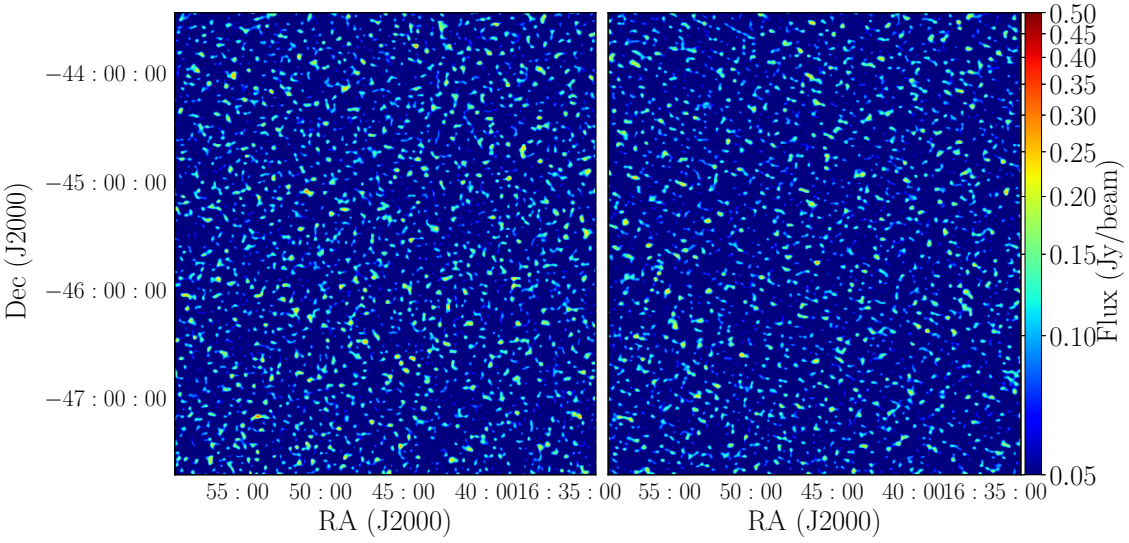

FIGURE 5.3: The residual images of the 1667 (left) and 1665 MHz (right) OH masers.

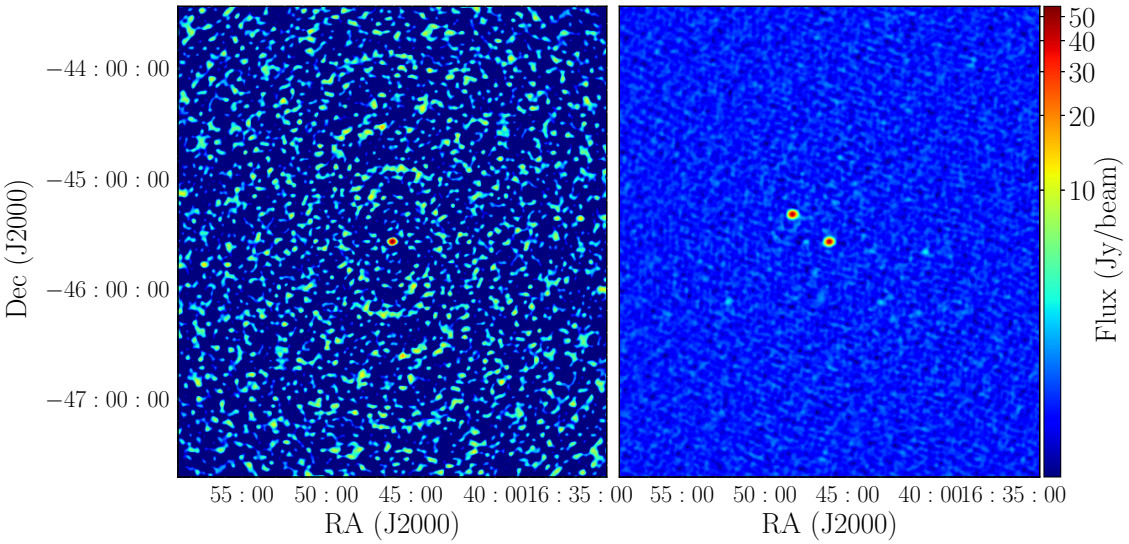

FIGURE 5.4: The left panel is the PSF image. The right panel is the zero moment map at 1665 MHz.

5.2 Analysis of maser spectra

Figure 5.5 shows the lower and upper envelopes as well as the average spectrum of the observed masers in G339.62-0.12. These envelopes represent the absolute maximum and minimum values reached over time for each velocity channel. The vertical dashed lines on the graph represents the systemic velocity ($V_{\rm sys}$ = -34.2 km s^{-1}) of the masers. Features that appear to be individual maser features are also labelled with letters. Each feature signifies the maximum flux density of the maser emission recorded at a specific velocity.

The 6.7 GHz CH_3OH maser spectrum is shown in the top panel of Figure 5.5. The spectrum covers velocity ranges from -38.2 km s^{-1} and -30 km s^{-1}. The identified velocity components have been labelled A to G. From the methanol maser spectrum, some of the velocity components seem to blend with other velocity features. This is predominantly seen in single-dish observations where the blending cannot be easily disentangled.

The middle and bottom panels of Figure 5.5 show the spectra for the mainline OH masers. The emission of both OH masers fall within the velocity range covered by the methanol maser emission. The features for the 1665 MHz and the 1667 MHz OH masers are labelled A to F and A to C, respectively.

For easy comparison, the average spectra for the 6.7 GHz CH_3OH and the mainline OH masers were overlaid as shown in Figure 5.6. Using $V_{\rm sys}$ as a reference, the maser emission falls on the red-shifted (V_3) or blue-shifted (V_1) side of $V_{\rm sys}$. However, no emission is found between -34 km s^{-1} and -35 km s^{-1} (V_2). For this current epoch, none of the strongest OH features corresponds to the CH_3OH maser features.

From the spectra, the mean flux densities of the peak features and the S/N were measured. The summary of the measured parameters from the spectra can be found in Table 5.3. With sufficient S/N, the measured flux density from the spectra was used to generate time-series for each maser feature. This will further be described in the section below.

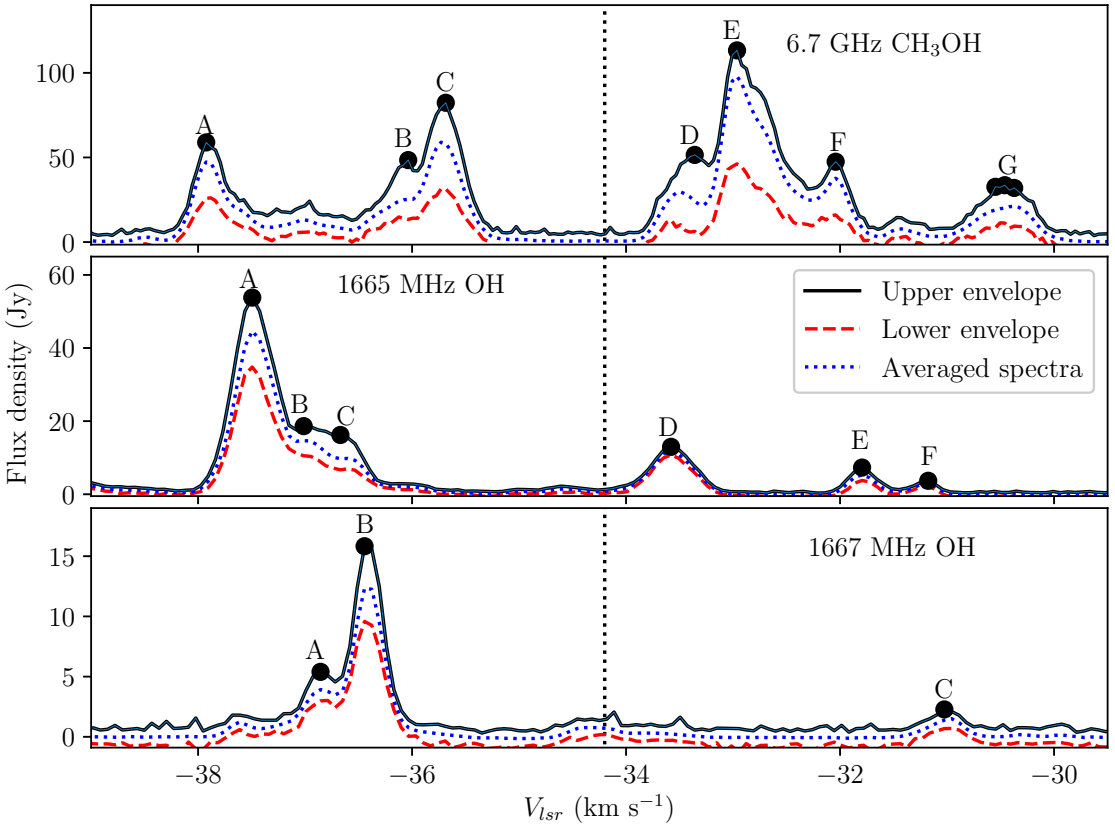

FIGURE 5.5: The spectra of the 6.7 GHz CH_3OH and the mainline OH masers in G339.62-0.12. Note that the labels correspond to the peak velocity components.

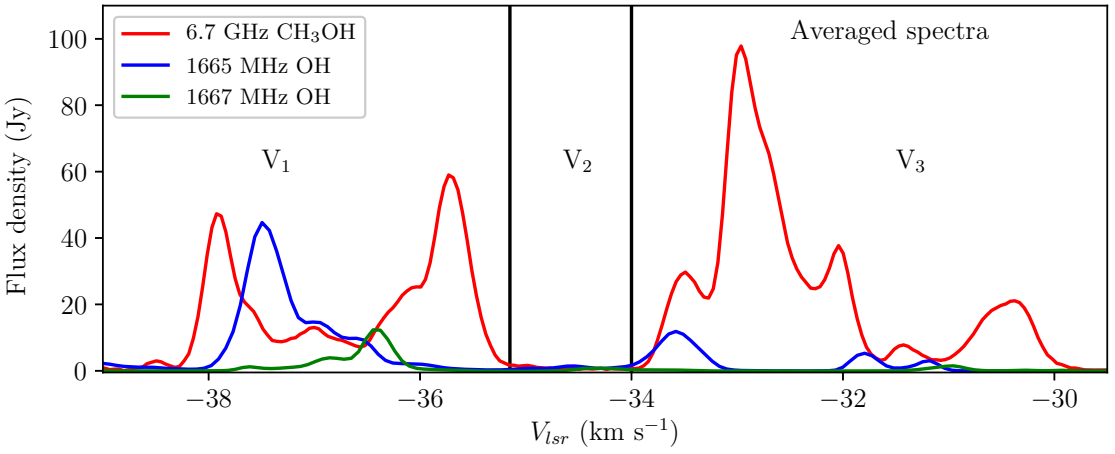

FIGURE 5.6: An overlay of the 6.7 GHz CH_3OH and the mainline OH masers mean spectra. (V_1) is a representation of the blue-shifted side while (V_3) is the red-shifted side of the systemic velocity.

TABLE 5.3: A summary of the parameters for the CH_3OH and OH maser spectra associated with G339.62-0.12.

Maser type	Peak Vel (kms^{-1})	Mean flux density (Jy)	Mean r.m.s (Jy)	S/N (σ)
6.7 GHz CH_3OH				
A	−37.92	47.4	1.7	24.4
∗	−37.57	18.0	1.8	10.4
∗	−37.27	9.0	2.1	4.8
∗	−36.96	12.8	1.9	7.1
B	−36.04	25.4	1.9	13.7
C	−35.69	58.3	1.7	29.2
D	−33.36	24.7	1.9	14.5
E	−32.96	98.5	1.8	55.1
F	−32.04	38.2	1.9	22.8
G	−30.55	18.8	2.0	14.7
	−30.46	20.0	1.8	14.6
	−30.37	21.0	1.9	15.3
1665 MHz OH				
A	−37.49	44.66	0.28	159.1
B	−37.01	14.69	0.21	69.4
C	−36.67	9.75	0.21	46.7
D	−33.58	11.87	0.20	58.8
E	−31.79	5.29	0.21	25.6
F	−31.17	3.04	0.20	15.0
1667 MHz OH				
A	−36.86	3.92	0.24	16.5
∗	−36.51	9.54	0.23	40.9
B	−36.44	12.34	0.24	52.6
∗	−36.24	5.93	0.23	26.0
C	−31.03	1.38	0.23	6.0

The asterisk (∗) represents maser features that were not labelled on Figure 5.5 but form part of the masers blue-shifted components from the systemic velocity.

5.3 Time-series analysis

Figure 5.7 shows the time-series for the 6.7 GHz methanol maser associated with G339.62-0.12. The time series of each velocity component clearly shows the masers are variable. It is interesting to note that the features with velocities ranging between -35.6 km s^{-1} and -37.5 km s^{-1} have regular cycles with each light curve consisting of four cycles. The first cycle is, however, not well sampled. It can also be seen in Figure 5.7 that the time interval per cycle is almost always the same. The features at -37.92 km s^{-1} and -37.57 km s^{-1} show less clear cycles. For the maser velocity components with velocities ranging between -34 km s^{-1} and -30 km s^{-1}, the features show increasing and decreasing amplitude or asymmetric profiles without clear cyclic modulation. For example, the component at -33.36 km s^{-1} steadily increases from 25 Jy to 53 Jy after reaching MJD 56750 (see Appendix C for more examples of the behaviour).

Figures 5.8, & 5.9 show the time-series for the 1665 and the 1667 MHz OH masers. Visual inspection of the time-series shows that the OH masers are also variable. The OH maser features blue-shifted from the systemic velocity also have well defined cycles.

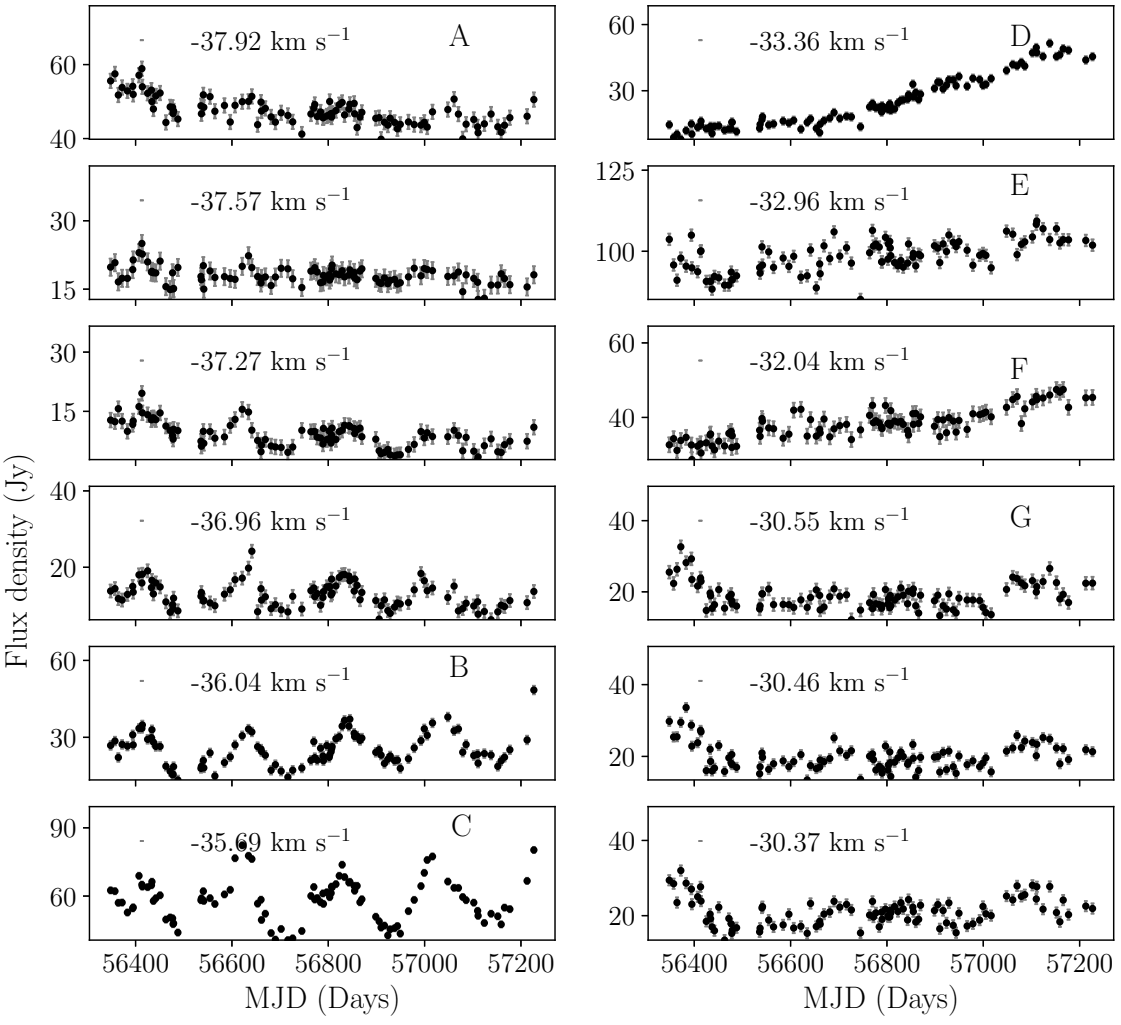

FIGURE 5.7: The light curves for the 6.7 GHz CH_3OH maser.

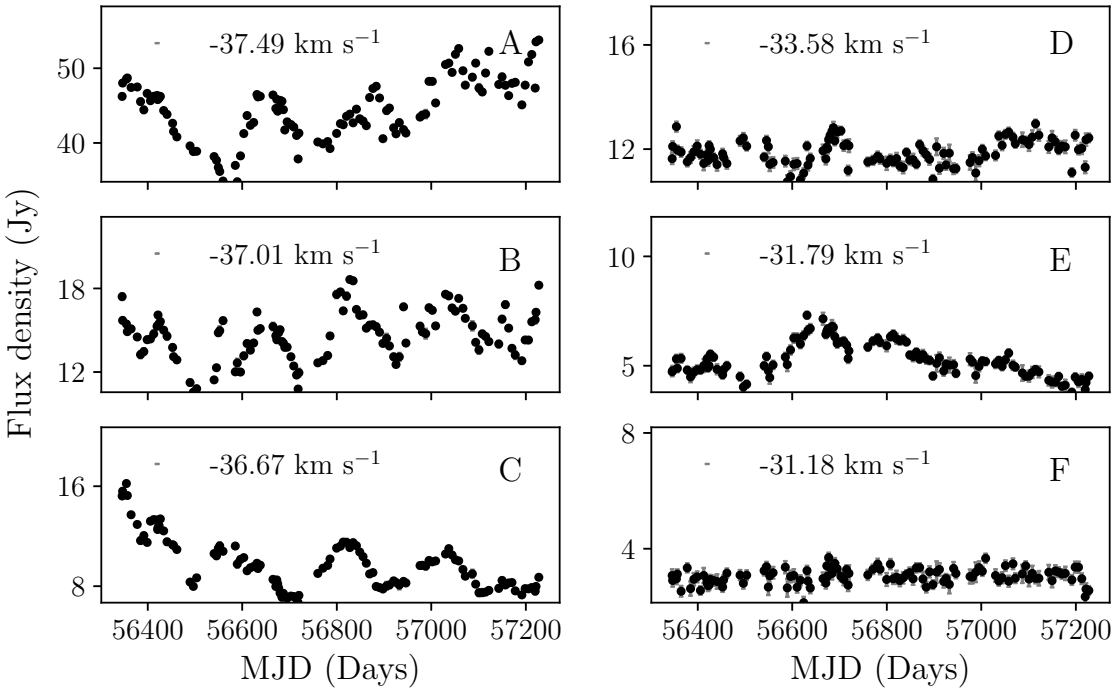

FIGURE 5.8: Time series for the 1665 MHz OH maser.

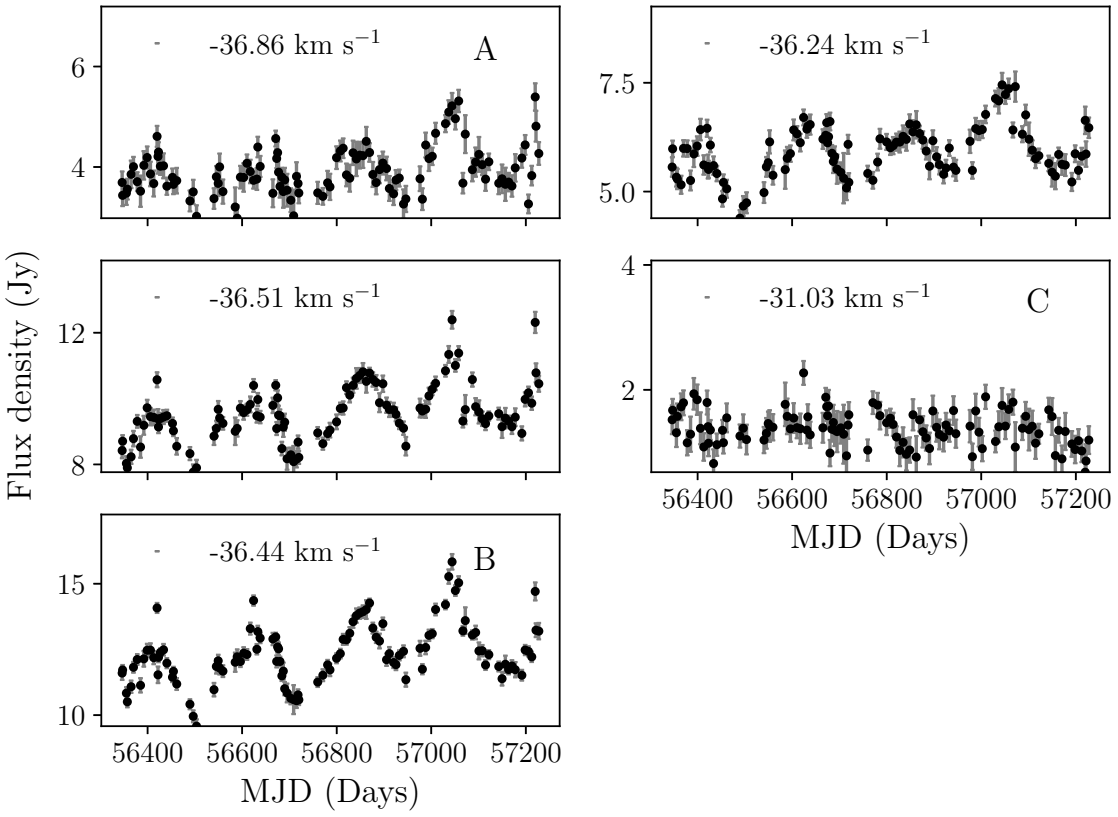

FIGURE 5.9: The light curves for the 1667 MHz OH maser.

5.4 Period search and statistical significance

One key task in time-domain maser studies is to determine the periodicity of periodic masers. However, observations in radio astronomy are seldom done at regular intervals. Gaps are therefore found in the data and dealing with the gaps becomes a necessity. The Lomb-Scargle (L-S) periodogram is one of the commonly used methods to search for periodic signal(s) in unequally spaced sample data (Lomb, 1976; Scargle, 1982). A periodogram measures the variability power of different frequency components in order to identify significant periods in a time-series (Schuster, 1898).

Let's consider the sequence of observation ($X_{\rm j}$) in a time-series measured at times ($t_{\rm j}$). The equation for the Lomb-Scargle periodogram ($P_{\rm LS(f)}$) over specified frequency (f) is given as

$$P_{LS(f)} = \frac{1}{2}\left\{ \frac{\left[\sum_j X_j \cos\omega(t_j-\tau)\right]^2}{\sum_j X_j \cos^2\omega(t_j-\tau)} + \frac{\left[\sum_j \ X_j \ \sin\omega(t_j-\tau)\right]^2}{\sum_j X_j \ \sin^2\omega(t_j-\tau)} \right\} \tag{5.1}$$

where $\omega = 2\pi f$ and j = 1, 2, 3, ..., N. N is the total number of samples. Equation 5.1 was obtained from VanderPlas (2018). The parameter τ, is a constant defined by

$$\tau = (\frac{1}{2\omega})\tan^{-1}\left[\frac{\sum_j \sin 2\omega(t_j)}{\sum_j \cos 2\omega(t_j)}\right] \tag{5.2}$$

Not all peaks in the periodogram are real. There is a possibility of having peaks that result from noise, therefore, a significance test must be carried out. With this, the probability of finding a peak with a particular power that exceeds a certain power threshold level (z_0) can be determined from the calculated periodogram using the Cumulative Distribution Function (CDF). Using the L-S periodogram, the significance of the power in a range of frequencies is given by

$$Prob(P_{LS}(f) > z_0) = exp(-z_0) \tag{5.3}$$

where Prob ($\rm P_{LS}(f) > z_0$) is the periodogram value and it is equivalent to the False Alarm Probability (FAP) (Scargle, 1982). The CDF for the power distributed exponentially is denoted by Z and $\rm P_{LS}(f) = Z$

The probability that a significant peak(s) identified in the periodogram does not result from noise is given through the False Alarm Probability (FAP) and it is related to Equation 5.3 as

$$FAP = 1 - [1 - exp(-z_0)]^M \tag{5.4}$$

where M is the number of independent frequencies, expressed as $M \approx \frac{\Delta f}{\delta f}$. Δf is the change in frequency and $\delta f = \frac{1}{T}$ where T is the period. Any peak found below the value of z_0 will be not be taken as real peaks.

5.4.1 L-S periodogram analysis of the observed masers in G339.62-0.12

Using the L-S periodogram, we investigated each maser time-series for possible presence of periodic variations. As a first step, those maser features with well-sampled cycles were selected for the analysis. The blue-shifted maser features having well sampled cycles were used to search for the period.

Figures 5.10 & 5.11 show the periodogram labelled A to R for the blue-shifted 6.7 GHz CH_3OH and the mainline OH masers, respectively. For the 6.7 GHz CH_3OH maser, the peak of feature A at -37.92 km s^{-1} is very low as compared to that of the other features labelled B to F. The period of the maximum in the periodogram for features B to F is 210 ± 19 days. The peak profiles of the masers are also seen to be quite broad in the periodogram. The broad peaks reflect the uncertainty in the frequency of the periodogram. The uncertainty in each peak was determined using a Gaussian function to fit the top half of the peak. The half width at half maximum (HWHM) of the full width at half maximum (FWHM) of the Gaussian function fit is given by

$$HWHM = \sqrt{2ln(2)}\ \sigma \tag{5.5}$$

where σ is the standard deviation of the Gaussian function. The uncertainty in the period was estimated from

$$|\frac{f\sigma}{P_{LS}(f)}| = P(\frac{\delta_\sigma}{\nu_0}) \tag{5.6}$$

where f is the frequency, σ is the standard deviation of the Gaussian from Equation 5.5, δ_σ is the uncertainty in the period and the ν_0 is the mean of the Gaussian peak profile.

Figure 5.11 shows the periodograms for the blue-shifted 1665 MHz and 1667 MHz maser features. The periods for 1665 MHz features K and L is 205 ± 22 days while for feature M it is 215 ± 32 days. For the 1667 MHz maser, the features Q and R also had the same period of 205 ± 19 days. The large uncertainties in the period are suspected to likely result from the relatively short time-series.

To increase the time-series, the 6.7 GHz CH_3OH maser time series of Goedhart et al. (2014) and that of this current observation were combined for the feature at velocity -36.96 km s^{-1}. Although this gave a much longer time-series (from MJD 52852.86 to 54735.57 and MJD 56342.17 to 57176.97), there was a gap of about 1600 days found in the time-series. Using the new time-series as well as the 1665 MHz OH maser feature at -37.01 km s^{-1} and the 1667 MHz OH maser feature at -36.44 km s^{-1}, the resulting periodogram is shown in Figure 5.12. The peak profile of the 6.7 GHz CH_3OH maser is now seen to be quite narrow and the corresponding period is found to be 201 days. Since this period falls within the error range of the derived periods for all the periodic features, this period may be a good indication of the actual underlying period of all the periodic masers in G339.62-0.12. The period was further used to fit the time-series of the masers as shown in Figure 5.13. Due to the differing cycle patterns, it is seen that the peaks of the masers do not follow each other although the peaks are well defined.

To further investigate the periodicity for individual maser species, all velocity channels between -39 km s^{-1} and -30 km s^{-1} were selected for the analysis. This is to likely to show the velocity channels which exhibit periodic behaviour immediately. In this case, the periodogram for each channel was calculated and the maximum power and the corresponding periods were extracted.

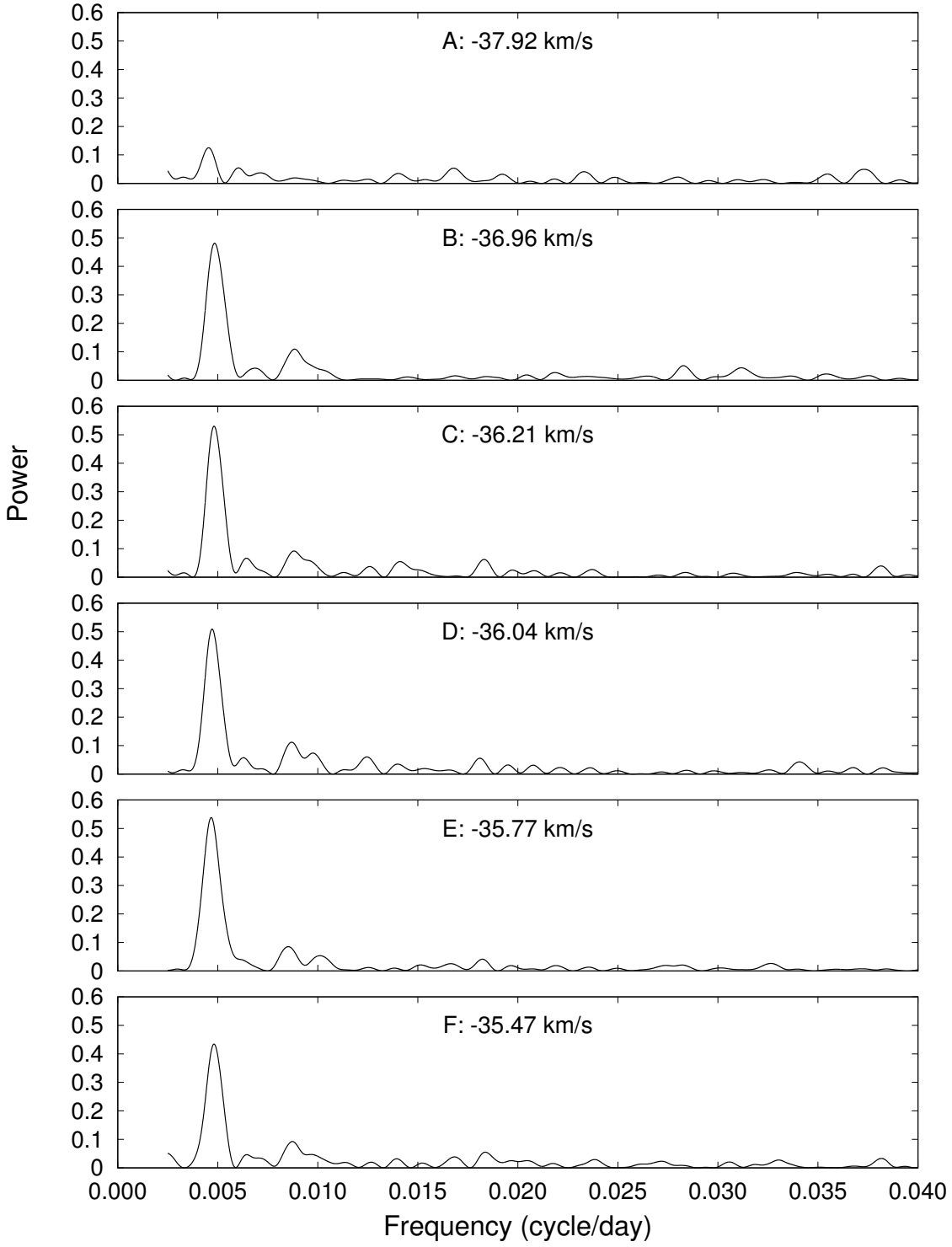

FIGURE 5.10: Periodogram for six blue-shifted 6.7 GHz CH_3OH maser features.

For the 6.7 GHz CH_3OH masers, a third-order polynomial was used to first detrend the time-series. Figure 5.14 shows the power and period at the maximum for the selected velocity channels where the upper panel represents the maximum power ($P_{\max}$) recorded at each velocity and the lower panel corresponds to the period of each velocity channel. Using Equation 5.4, the 0.1% false alarm probability level for a significant peak in the periodogram is 0.24 as can be seen in the top panels (a) of Figures 5.14 to 5.16. It is seen that for masers with velocities within -37.6 $\leq$ $V_{\rm lsr}$ $\leq$ -35.3 km s^{-1}, the cutoff (z_0) for determining the significant peaks are seen for $P_{\max} > 0.24$.

In the bottom panel of Figure 5.14, the blue-shifted masers with velocities within -37.6 $\leq$ $V_{\rm lsr}$ $\leq$ -35.3 km s^{-1} are seen to have average period of 210 days. However, the red-shifted masers have periods less than 200 days. There were periods far greater than 200 days also identified. This may be due to the presence of long-term variabilities at such velocities as can be seen in Figure C.3. There is however, a hint of periodicity at velocities around -32.7 km s^{-1} and -33.45 km s^{-1}.

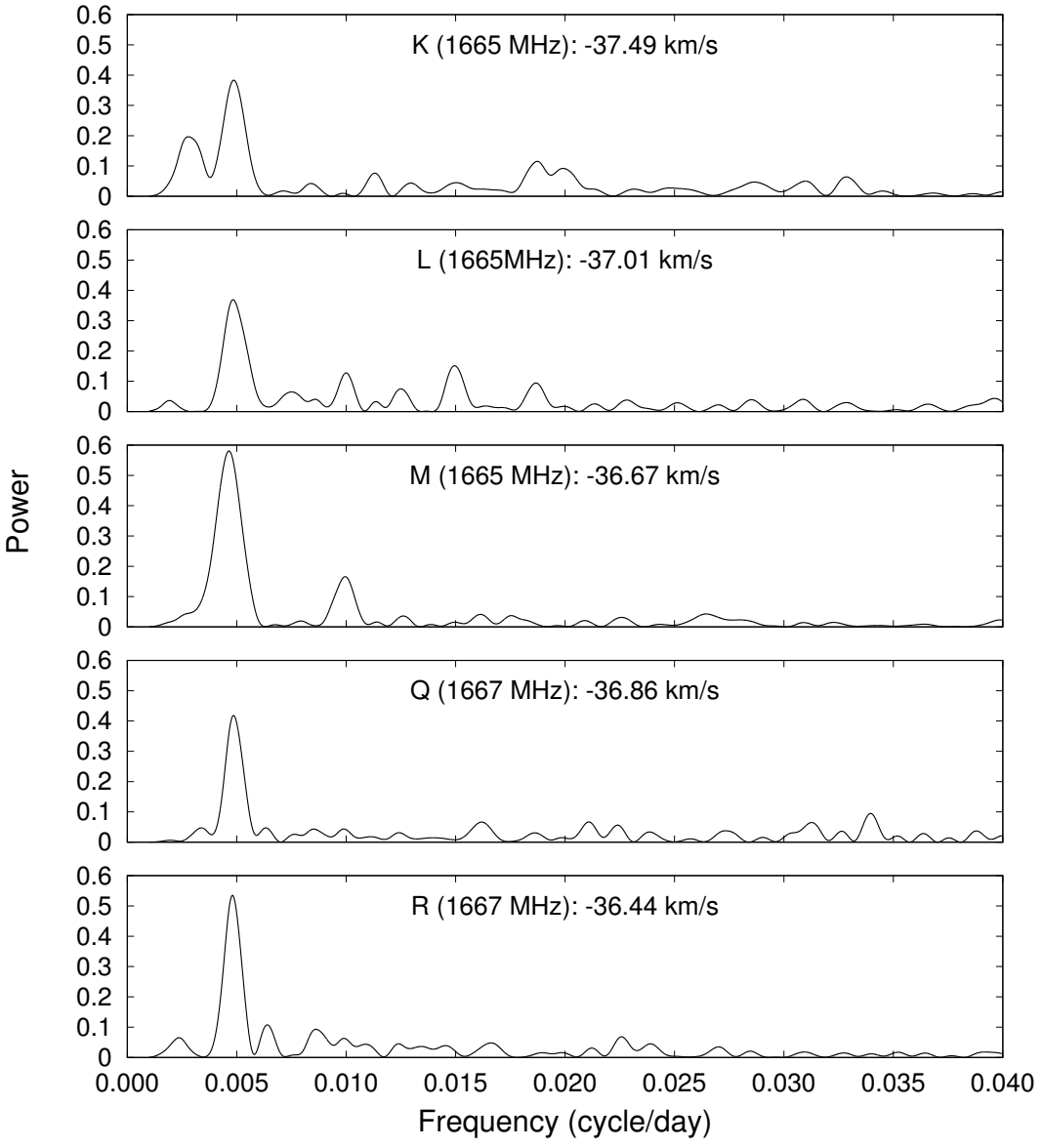

FIGURE 5.11: Periodograms for the blue-shifted 1665 MHz and 1667 MHz maser features.

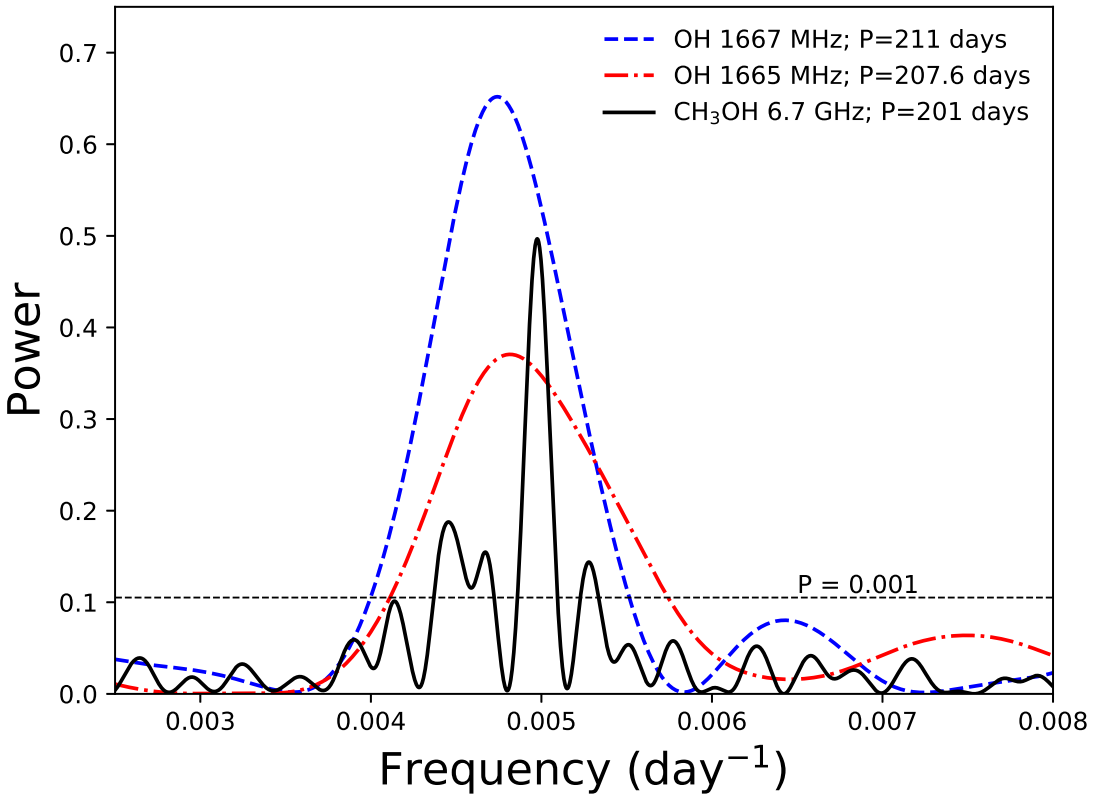

FIGURE 5.12: The periodogram for specific maser features

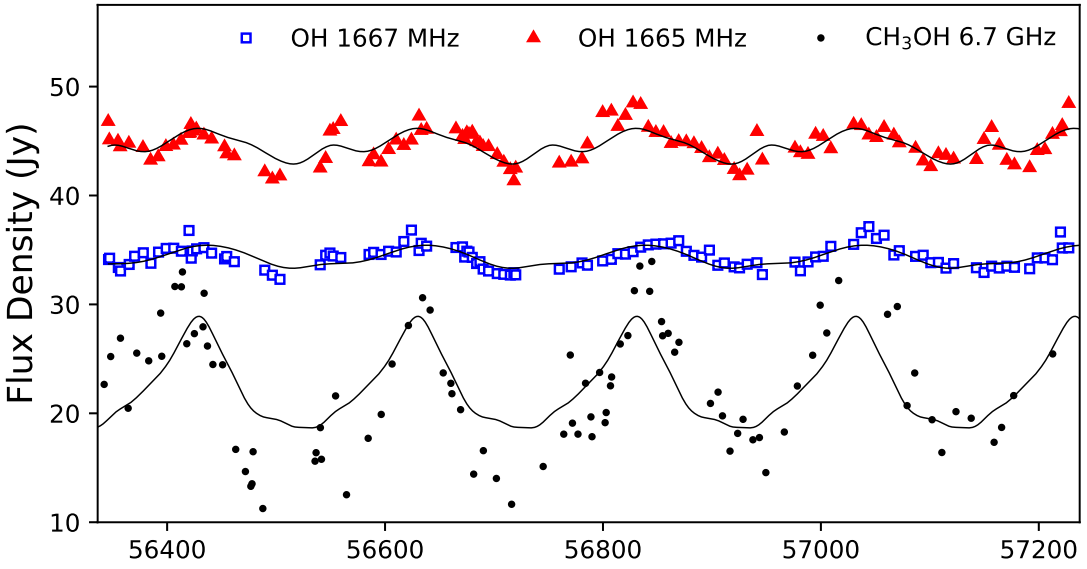

FIGURE 5.13: The running mean of individual masers profiles for the current epoch.

The period around these velocities is also manifested by a 'plateau' similar to the one seen for the blue-shifted masers. Likewise, the period for those around velocities -33.5 km s^{-1} agree with that of the blue-shifted masers. For velocities around -32.7 km s^{-1}, the average period is found to be 193 days. This is significantly less than that of the blue-shifted masers.

Figures 5.15 & 5.16 show the power and period at the maximum for the 1665 and 1667 MHz OH masers. Each time-series was detrended using a linear function. Periodic behaviour is also seen for the mainline OH masers over a range of velocity channels. For the 1665 MHz OH maser, the average period was found to be 205 days. The 1667 MHz maser also had the same average period of 205 days.

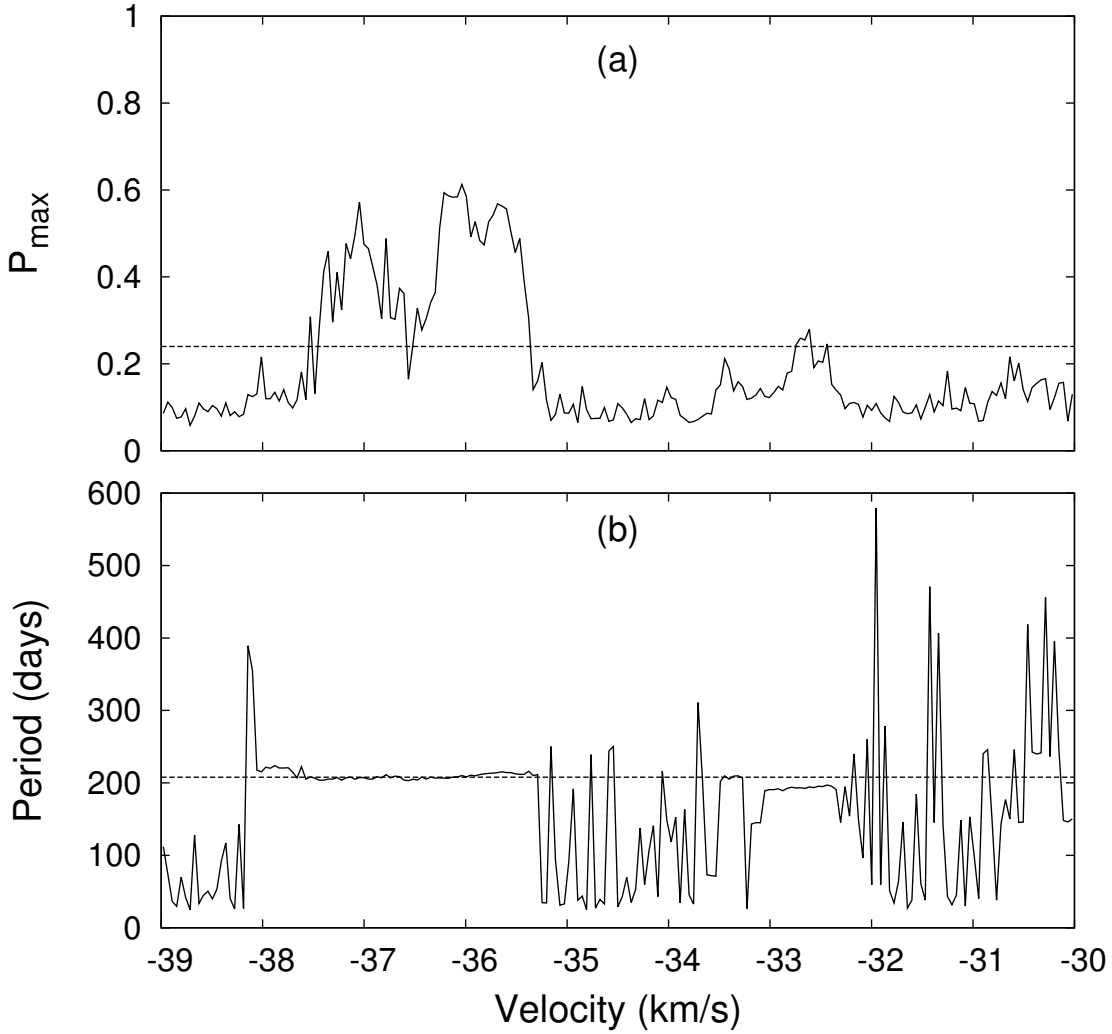

FIGURE 5.14: Panel(a): The maximum power ($P_{\max}$) as a function of velocity for the 6.7 GHz CH_3OH maser. Panel(b): The period at the maximum as a function of velocity.

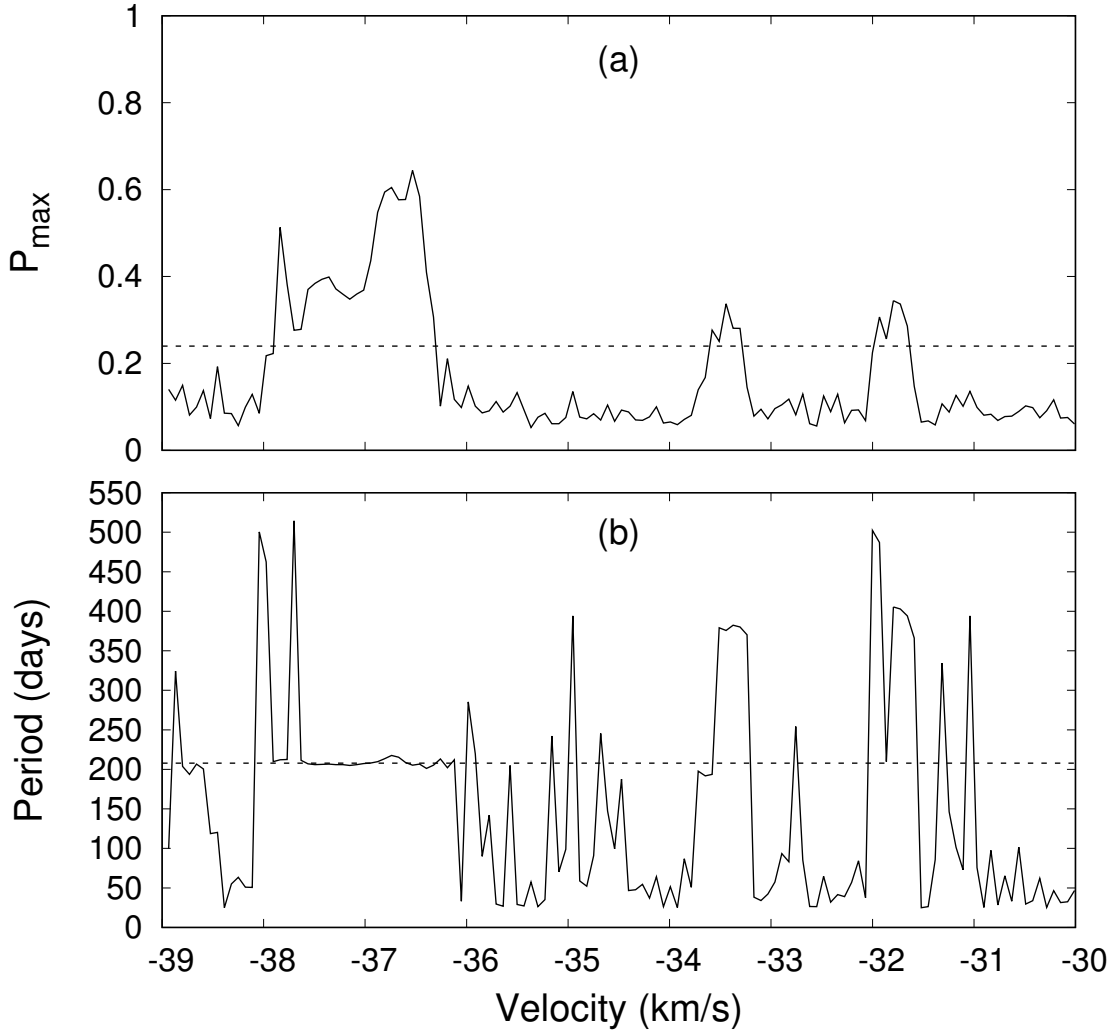

FIGURE 5.15: Panel(a): The maximum power as a function of velocity for the 1665 MHz OH maser. Panel(b): The period at the maximum across velocities -39 $\mathrm{km\,s^{-1}}$ and -30 $\mathrm{km\,s^{-1}}$.

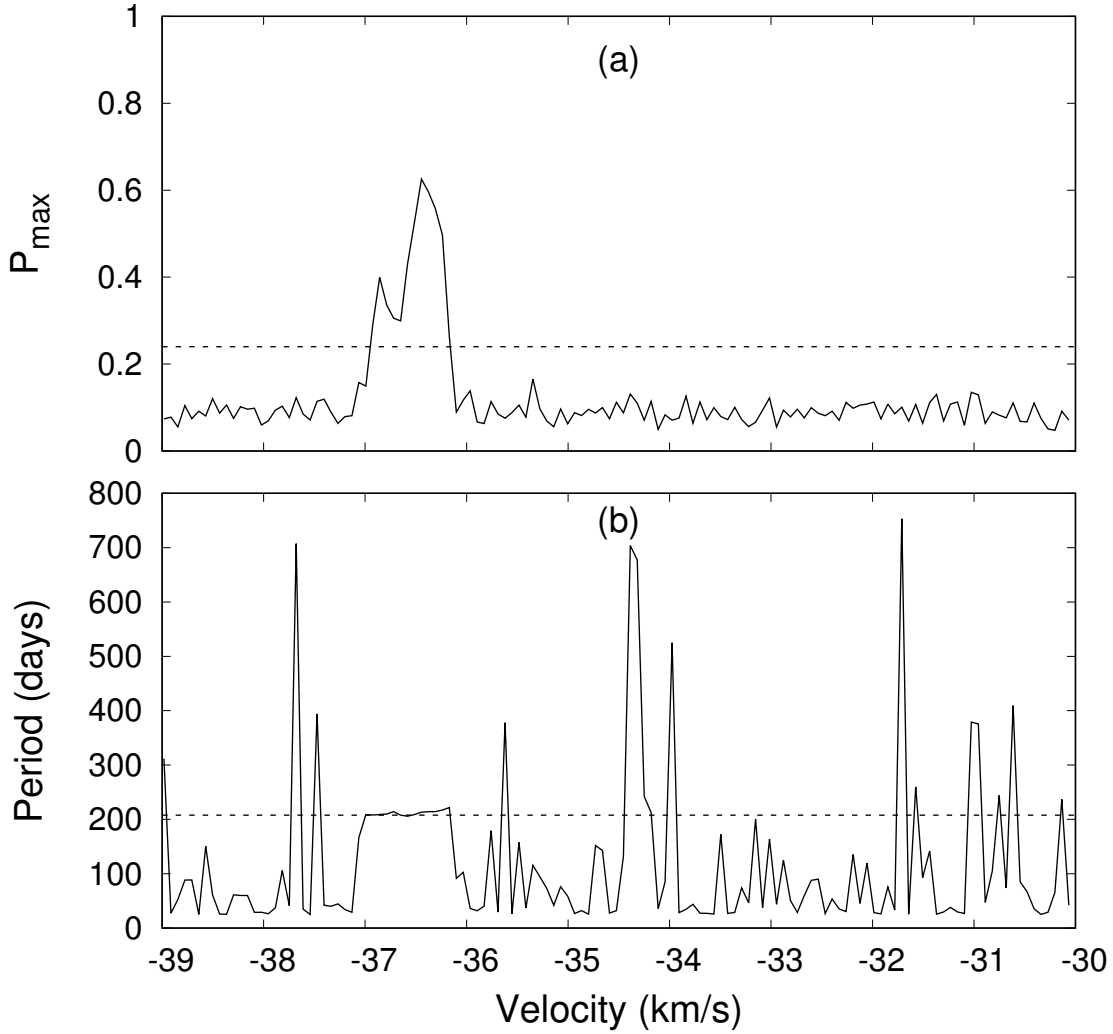

FIGURE 5.16: Panel(a): The maximum power as a function of velocity for the 1667 MHz OH maser. Panel(b): The period at the maximum as a function of velocity.

Figure 5.17 shows the peak power and the corresponding period for some selected velocities for the masers. The periods were found to be 203 ± 2 days for the 6.7 GHz CH_3OH maser, 208 ± 2 days for the 1665 MHz OH maser and 210 ± 2 days for the 1667 MHz OH maser.

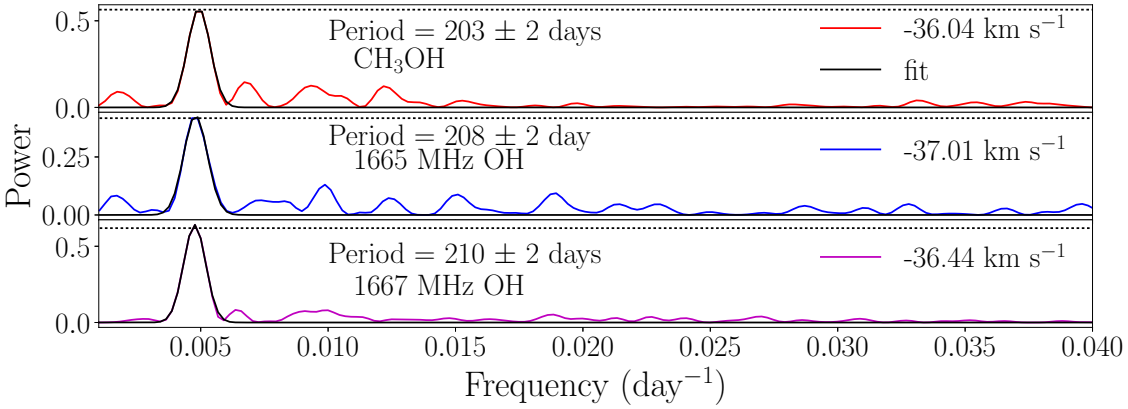

FIGURE 5.17: L-S Periodogram for the observed masers at velocities selected from the lower panels of Figure 5.14 to Figure 5.16.

Chapter 6

Discussion

6.1 The single-dish 6.7 GHz CH_3OH masers

Following the activity of the masers discussed earlier, G339.62-0.12 seems to be an interesting, yet complex source. Comparison of the single-dish 6.7 GHz CH_3OH maser spectrum in the top panel of Figure 5.5 to similar observations carried out by Goedhart et al. (2014) and MacLeod & Gaylard (1992), some of the peaks shifted in velocity. Also, the features at velocities -33.26 and -32.92 $km\,s^{-1}$ seem to have blended into the E component of the current observation. The flux density of feature C has comparatively decreased by half. Comparing with the observations of MacLeod & Gaylard (1992), maser emission was present at -34 and -35 $km\,s^{-1}$. The observations by Goedhart et al. (2004) however suggest that the maser emission in this velocity range was already not present during the time the authors monitored G339.62-0.12. This implies that apart from the observed variability, the maser spectrum is not static as some velocity components of the masers disappear while other features increase and decrease in flux density over time.

The only high-resolution imaging of the 6.7 GHz CH_3OH masers in G339.62-0.12 is that of Walsh et al. (1998). Figure 6.1 shows the position-velocity (PV) diagram of the 6.7 GHz CH_3OH maser spots associated with G339.62-0.12 as constructed by these authors. The top panel represents the structure of the methanol maser spots in G339.62-0.12. The 6.7 GHz CH_3OH masers seem to have a ring-like distribution. Walsh et al. (1998) fitted an ellipse to the maser spots in panel (a) and interpreted the maser ring-like distribution to be an indication of the presence of a rotating structure. From the fit, it may be that the structure is an inhomogeneous disk surrounding the central source (De Buizer et al., 2012). The offsets are in arcsec from the IRAS position in the maser site. The horizontal axis is the offset in position along the major axis of the brightest maser spot in the region. The vertical axis is the measured radial velocity of the central star ($M > 6\,M_\odot$). Radio observations of Purser et al. (2016) classify G339.62-0.12 as a jet candidate although the model image of Wheelwright et al. (2012) reveals G339.62-0.1 to have a bipolar structure. The bipolar structure could be an indication that outflow activities or precessing jets are present in the region. Furthermore, H_2 emission observed at 2.1 μm by Navarete et al. (2015) coincide with the source. Navarete et al. (2015) suggest the presence of H_2 emission to be a possible indication of shocked gas associated with an outflow.

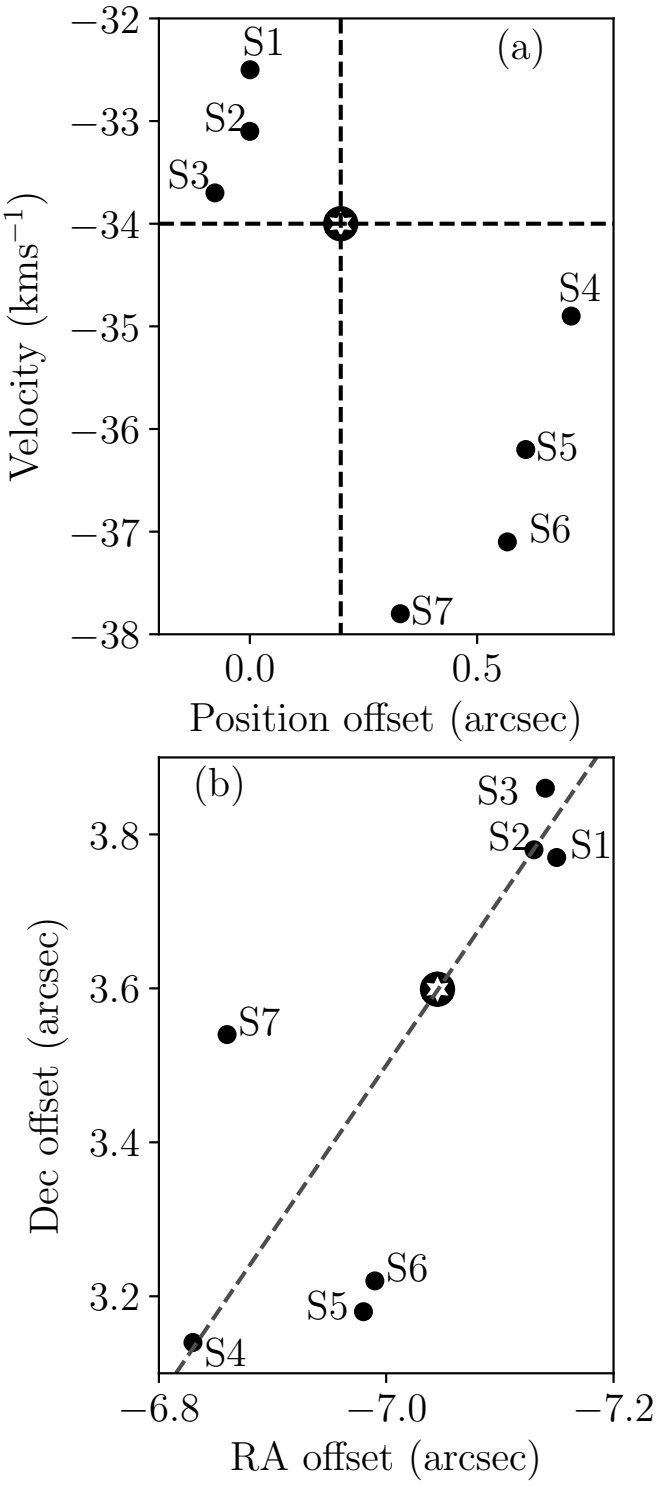

FIGURE 6.1: The P-V diagram of the 6.7 GHz CH_3OH maser spots associated with G339.62-0.12. This is adopted from the observation of Walsh et al. (1998). The star symbol represents the position of the gravitational source associated with the high-mass star in G339.62-0.12 derived by Walsh et al. (1998).

Panel (b) of Figure 6.1 shows the positions of the maser spots relative to the central star. It can be seen that the masers spots fall into two diagonally opposite quadrants. The quadrant axes indicate the position and radial velocity of the central mass. The component S7 seems to be associated with the components S2 and S3 whiles S1 is associated with S4, S5 and S6. To visualise the maser spots on the spectrum, they are overlaid on the methanol maser spectrum of this current work as shown in Figure 6.2. None of the S component is found to coincide with the peak velocities of the current maser spectrum, though the S2 feature seems to be closely associated with the feature labelled H. In the current epoch, component S4 is no longer seen to be present. Also, there is a deviation in the velocities of the maser spots to that of the maser features identified in the current epoch. This could be due to the spectral resolution ($0.044\,\mathrm{km\,s^{-1}}$) of the HartRAO 4.5 cm receiver, which is four times better than that of Walsh et al. (1998) ($0.18\,\mathrm{km\,s^{-1}}$). The features F, I and J in Figure 6.2 were not identified in the work of Walsh et al. (1998).

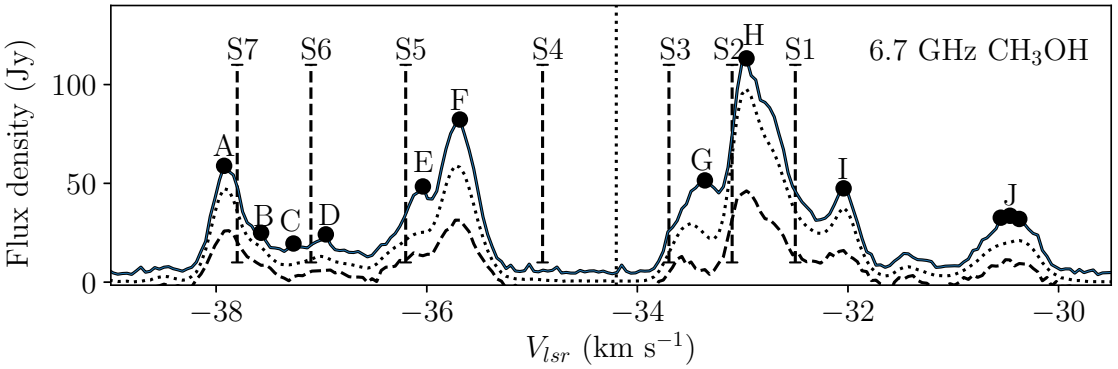

FIGURE 6.2: The overlay of velocities of the 6.7 GHz CH_3OH observed by Walsh et al. (1998) on the maser spectrum of the current observation. The small error bars at the top the of each dashed vertical line represents a velocity resolution of $0.18\,\mathrm{km\,s^{-1}}$.

From the maser spots of Walsh et al. (1998) in Figure 6.2, clear separation is seen in the red-shifted and blue-shifted masers as found in the current epoch. From the time-series of the 6.7 GHz CH_3OH masers in the current work, periodic variability is visible for the blue-shifted masers as compared to the red-shifted masers. From panel (b) of Figure 6.1, it is seen that component S7, which does not show periodic variability is rather associated with the red-shifted features S2 and S3. The S1 feature, however, is associated with the blue-shifted maser features S4, S5 and S6. This may be an indication that some of the red-shifted masers might be periodic.

6.2 The mainline OH masers

Since the work of Caswell et al. (1980), the flux density of the mainline OH masers in G339.62-0.12 has increased by a factor of about four. In comparison with the 6.7 GHz CH_3OH masers, the blue-shifted masers are periodic and the red-shifted masers are not. From the OH maser spectra, the peak flux of the 1665 MHz OH masers emission is three times higher than the peak flux of the 1667 MHz OH masers. Due to the lack of high-resolution observation of OH masers in G339.62-0.12, any possible comparison, especially at these frequencies, has become a limitation.

Chapter 7

Conclusions

In this work, we have presented the results of the 6.7 GHz CH_3OH masers which were observed in parallel with the mainline OH masers in G339.62-0.12. The following is the principal summary of the results of this work.

1. From the spectra, maser emission were found both at the blue-shifted and red-shifted sides of the systemic velocity ($V_{\rm lsr}$ = -34.2 km s^{-1}).
2. No maser emission was found at the systemic velocity. Also, the previously detected feature by MacLeod & Gaylard (1992) at about -35 km s^{-1} seems to have disappeared.
3. Periodic variability is clearly visible for features that are blue-shifted from the systemic velocity. The periods of the masers range between 205 ± 19 days to 215 ± 32 days. This period may be an indication of a similar mechanism responsible for periodic behaviour.
4. Using the Lomb-Scargle (LS) periodogram, the periods for the 6.7 GHz methanol, the 1665 and 1667 MHz OH masers are found to be 203 ± 2 days, 208 ± 2 days and 210 ± 2 days respectively. These periods fall within the derived periodicity for all the periodic maser features.
5. Some red-shifted maser features have periodic components of about 193 days. The variations could be an indication that the blue- and red-shifted masers may not have the same associated star-forming region.
6. We are uncertain about the precise location of the masers, hence, no clear conclusion about what is actually causing the periodicity can be made.

The interesting aspect of this work is the periodic behaviour exhibited by both the 6.7 GHz CH_3OH and the mainline OH masers in G339.62-0.12. The results of the 6.7 GHz methanol agree with the study from Goedhart et al. (2014). Although the masers show evidence of periodicity, the variability is complicated to explain by simply visualising the spectra and the time-series.

Furthermore, high-resolution observation of both the methanol and the mainline OH masers in the region will allow a more detailed analysis. With this, we can further identify and examine the nature of individual maser sources. Hence, we recommend a high angular resolution mapping of the G339.62-1.2 region. We also propose a multiwavelength observation to effectively understand the physical conditions in the star forming region. Relative positions of the masers will greatly help make further conclusions.

Appendix A

Theoretical calculations

A.1 KAT-7 data processing: Theoretical calculations

In order to increase the image quality for the 1665 MHz maser in the continuum, all the corrected visibilities can be merged into one data set. The dirty image can be used to estimate for the RMS noise level and the threshold determined (see Section 3.6.1). This method is generally preferred because on certain days of the observations, only a few telescopes are functional. This method tends to be more convenient and reliable. However, the threshold for CLEAN can alternatively be estimated by using theoretical calculations. The calculation below assumes all seven telescopes of the KAT-7 were operational during the observation. The theoretical RMS is then calculated by using the sensitivity equation (Thompson et al., 2017b). The sensitivity $\sigma_{\rm rms}$ of an interferometer is given by Equation A.1.

$$\sigma_{\rm rms} = \frac{2 * k * T_{\rm sys}}{\pi * r^2 * \epsilon_A * [N(N-1) * \Delta v_\nu * \tau]^{(\frac{1}{2})}} \tag{A.1}$$

where N is the number of telescopes, $\epsilon_{\rm A}$ is the aperture efficiency, Δv_ν is the bandwidth, τ is the integration time, r is the radius of the telescope, $T_{\rm sys}$ is the system temperature and k is the Boltzmann constant.

A.1.1 RMS of the 1665 MHz OH maser emitting field

Using the equation above, the sensitivity for the 1665 MHz OH maser in G339.62-0.12 SFR is calculated as

$$\sigma_{rms} = \frac{2 * 1.38 * 10^{-23} * 35}{\pi * 6^2 * 0.65 * [7(7-1) * 0.381 * 10^3 * 50 * 60]^{(\frac{1}{2})}}$$

$$\sigma_{\rm rms} = 1.896 * 10^{-27}\,{\rm J\,m\,s^{-2}}$$

$$\sigma_{\rm rms} = \frac{1.896 * 10^{-27}}{10^{-26}}[{\rm W\,m^{-2}\,Hz^{-1}}] = 0.1896\,{\rm Jy}$$

The theoretical RMS threshold for the 1665 MHz OH maser field, given as $3 \times \sigma_{\rm rms}$ is ≈ 0.57 Jy.

A.1.2 RMS of the 1667 MHz OH maser emitting field

The sensitivity for the 1667 MHz OH maser in G339.62-0.12 field is also calculated as

$$\sigma_{\rm rms} = \frac{2 * 1.38 * 10^{-23} * 35}{\pi * 6^2 * 0.65 * [7(7-1) * 0.381 * 10^3 * 45 * 60]^{(\frac{1}{2})}}$$

$$\sigma_{\text{rms}} = 2.12 * 10^{-27}\,\text{Jms}^{-2}$$

$$\sigma_{\text{rms}} = \frac{2 * 10^{-27}\,\text{Jms}^{-2}}{10^{-26}\,[\text{W m}^{-2}\,\text{Hz}^{-1}]} = 0.20\,\text{Jy}$$

The theoretical RMS threshold for the 1667 MHz OH maser field, given as $3 \times \sigma_{\text{rms}}$ is ≈ 0.6 Jy.

Appendix B

Parameter calculations for the imaging field

B.1 Image parameter calculations

B.1.1 1665 and 1667 MHz OH image parameters

The full-width at half maximum of the synthesized beam $\theta_{\rm sb}$ of the radio interferometer is given by

$$\theta_{\rm sb} \approx \frac{1}{(\frac{B_{\rm max}}{\lambda})}[rad] \tag{B.1}$$

or

$$\theta_{\rm sb} \approx \frac{3438}{(\frac{B_{\rm max}}{\lambda})}[arcmins] \tag{B.2}$$

where $\lambda = (\frac{c}{\nu})$.
The maximum baseline ($B_{\rm max}$) for KAT-7 is 185 m and the primary beam is 1°, that is $\approx$ 3600 arcseconds. From the KAT-7 observations, $\theta_{\rm sb}$ is calculated as

$$\theta_{\rm sb} \approx \frac{3438}{(\frac{185}{0.18})} = 3.4\,\text{arcmins}$$

The calculated cell size in the CLEAN is equivalent to a quarter of the $\theta_{\rm sb}$. Therefore, the cell size parameter $= \frac{3.4}{4} = 0.85$ arcmins.

Since the goal is to have pixels which are small enough to resolve the beam, the cell size was rounded down to 0.5 arcmins ($\approx$ 30 arcseconds). The field of view of the primary beam ($\theta_{\rm FWHM}$) of the interferometer is given by

$$\theta_{\rm FWHM} = \frac{1.02 * 3438}{(\frac{D_{\rm ant}}{\lambda})}$$

The diameter of each KAT-7 antenna is 12 m.
$\theta_{\rm FWHM} = 52$ arcmins

Appendix C

Time-series analysis: Extra results

The following are the time-series for the masers across velocities. Different behaviours are seen for the velocity ranges. This may suggest different maser components in the spectra as shown in Figure 5.5.

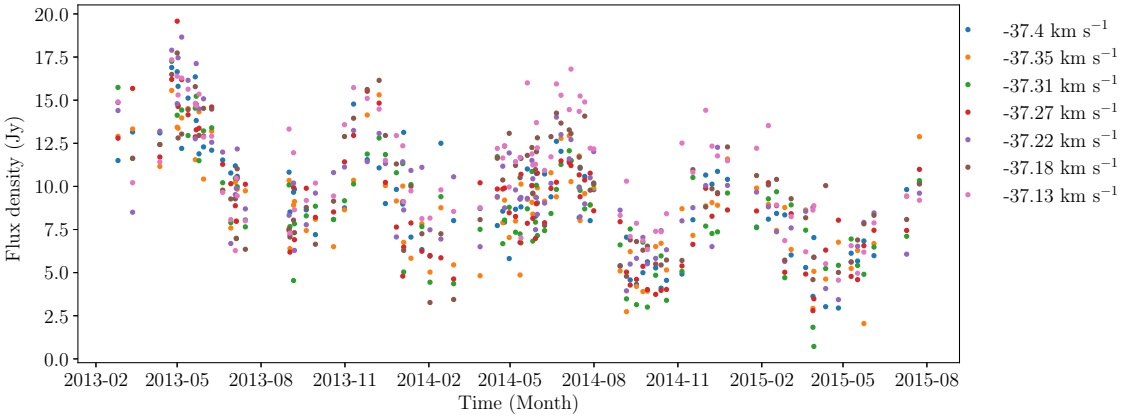

FIGURE C.1: Time-series for the 6.7 GHz CH_3OH masers with velocities ranging from -37.1 to -37.4 km s^{-1}

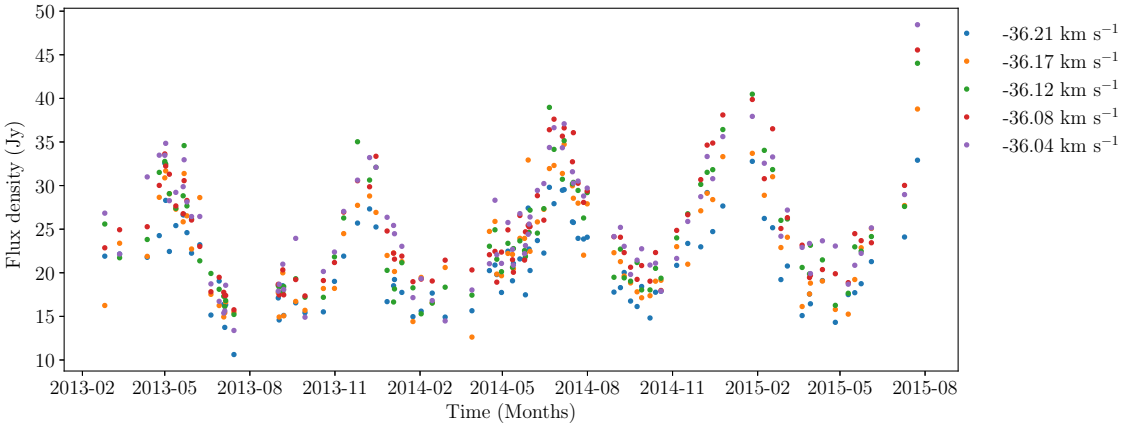

FIGURE C.2: Time-series for the 6.7 GHz CH_3OH masers with velocities ranging from -36.0 to -36.3 km s^{-1}

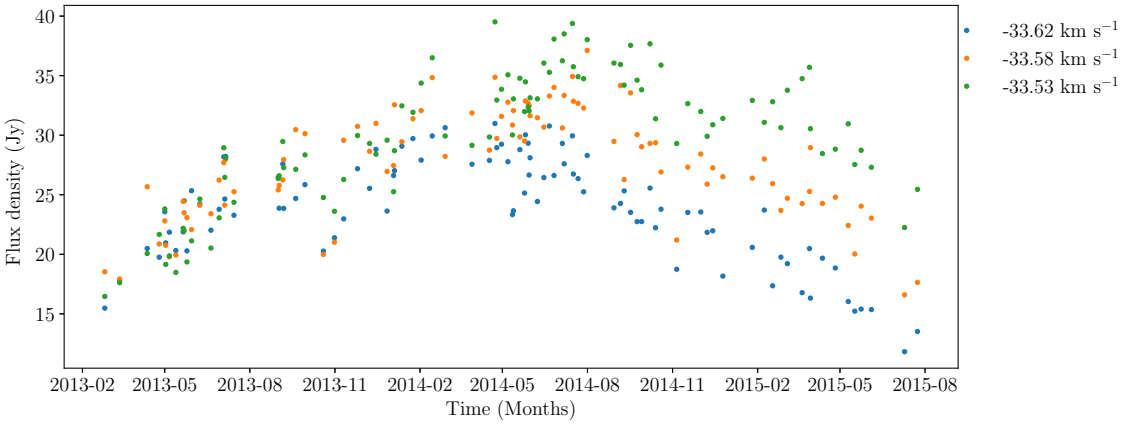

FIGURE C.3: Time-series for the 6.7 GHz CH_3OH masers at velocities ranging from -33.5 to -33.7 km s^{-1}

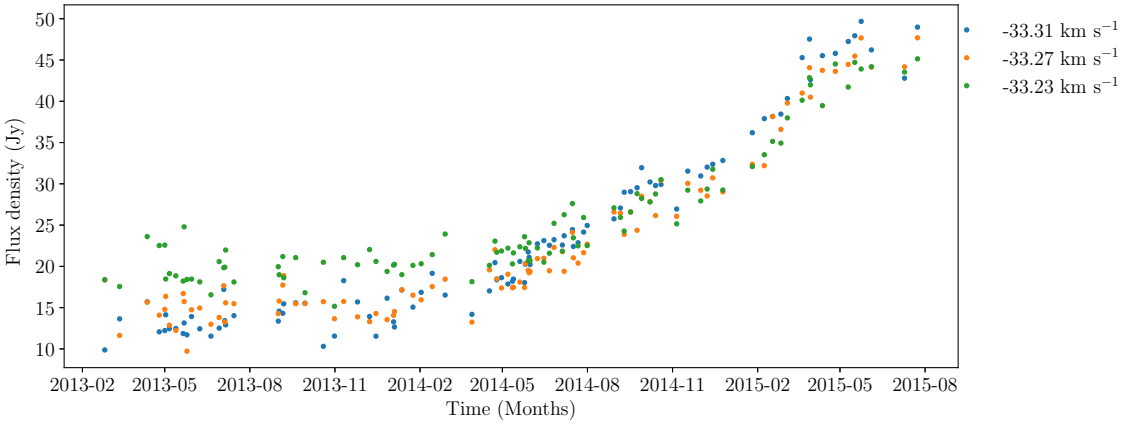

FIGURE C.4: Time-series for the 6.7 GHz CH_3OH masers at velocities ranging from -33.2 to -33.3 km s^{-1}

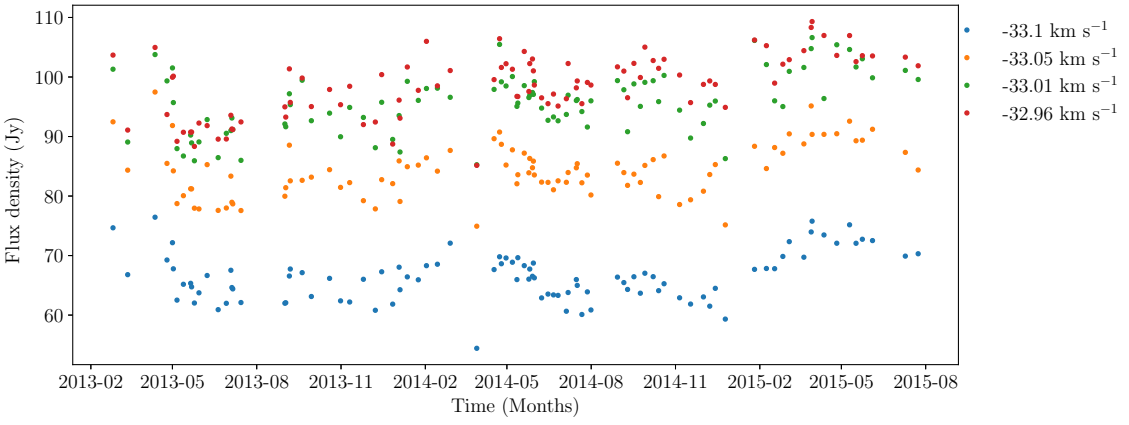

FIGURE C.5: Time-series for the 6.7 GHz CH_3OH masers at velocities ranging from -32.9 to -33.1 km s^{-1}

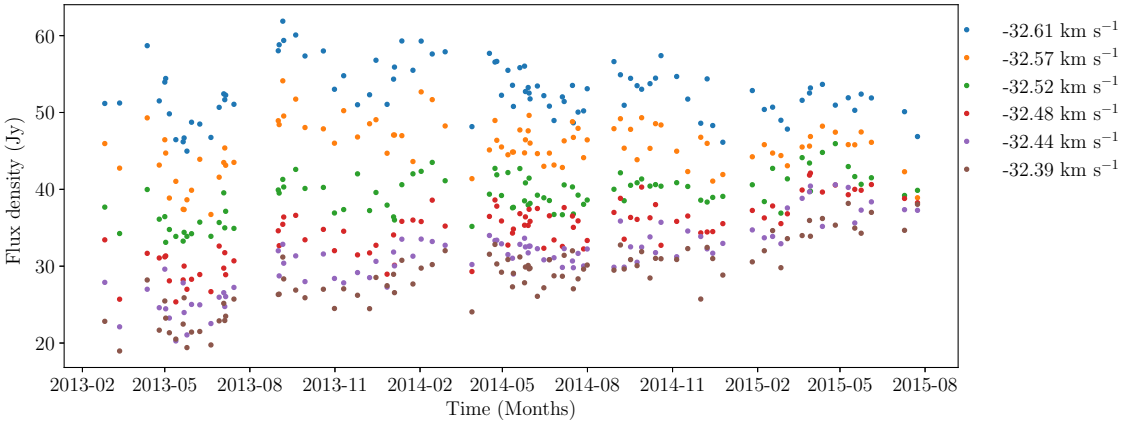

FIGURE C.6: Time-series for the 6.7 GHz CH_3OH masers at velocities ranging from -32.3 to -32.6 km s^{-1}

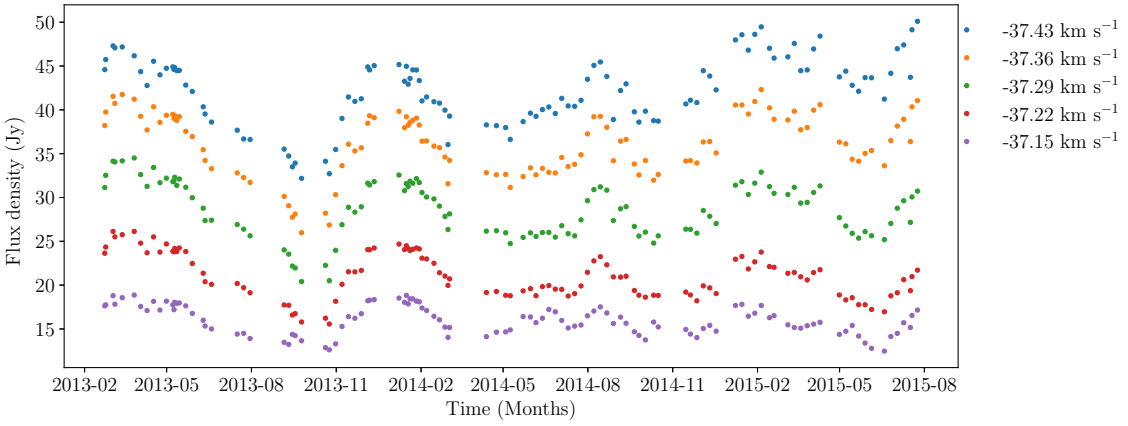

FIGURE C.7: Time-series for the 1665 MHz OH masers at velocities ranging from -37.1 to -37.5 km s^{-1}

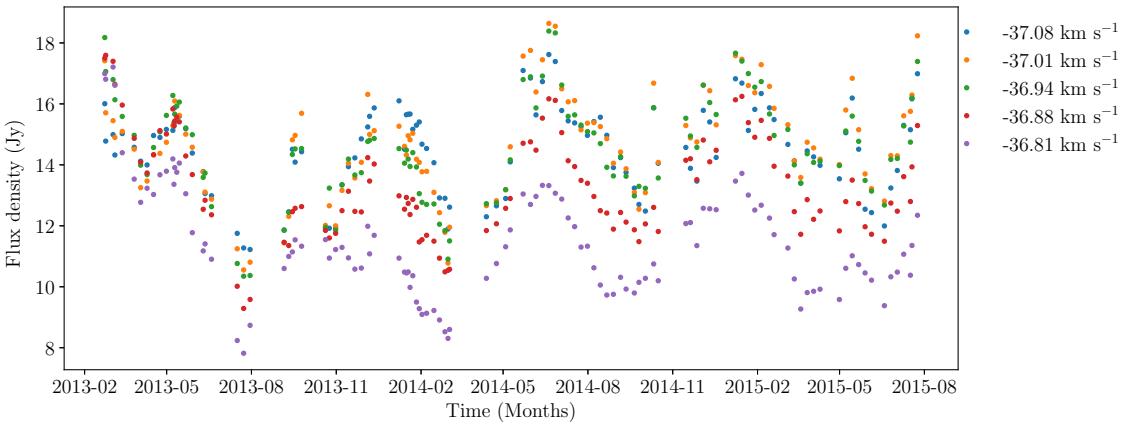

FIGURE C.8: Time-series for the 1665 MHz OH masers at velocities ranging from -36.8 to -37.1 km s^{-1}

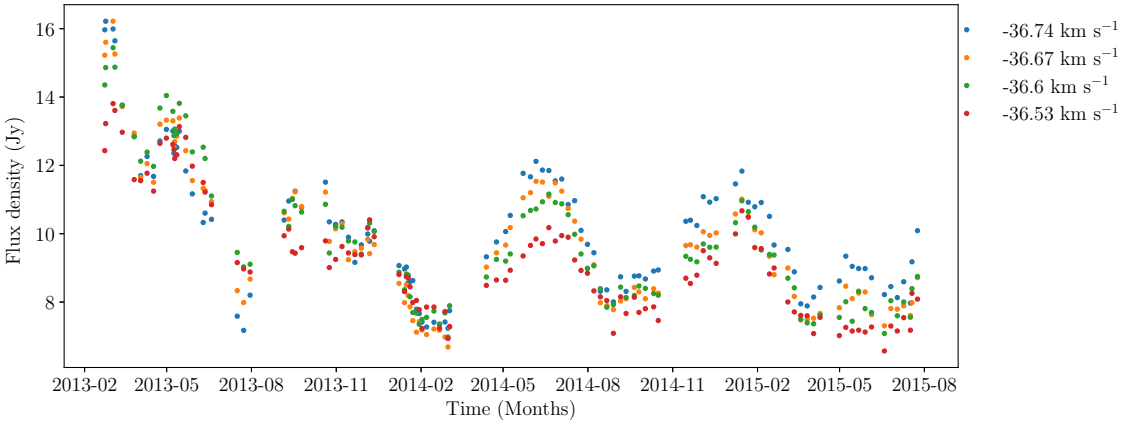

FIGURE C.9: Time-series for the 1665 MHz OH masers at velocities ranging from -36.5 to -36.8 km s^{-1}

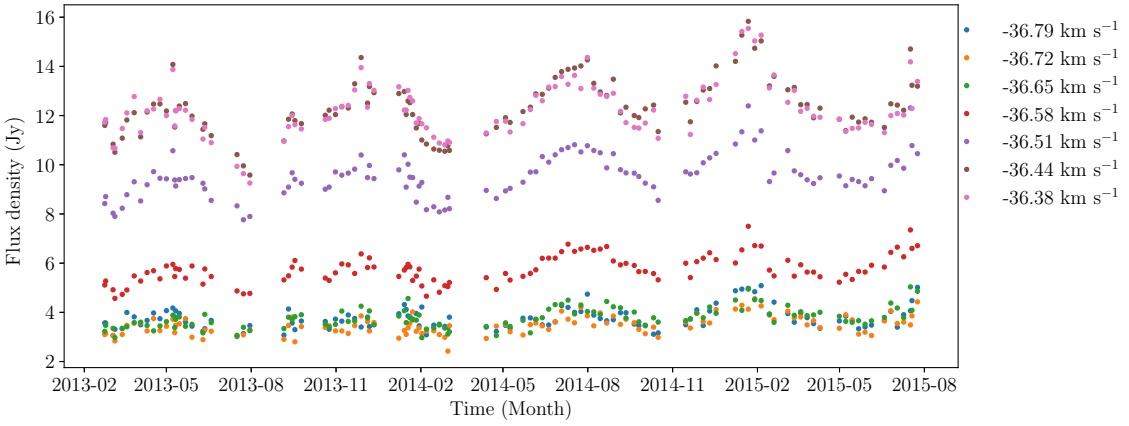

FIGURE C.10: Time-series for the 1667 MHz OH masers at velocities ranging from -36.3 to -37.0 km s^{-1}

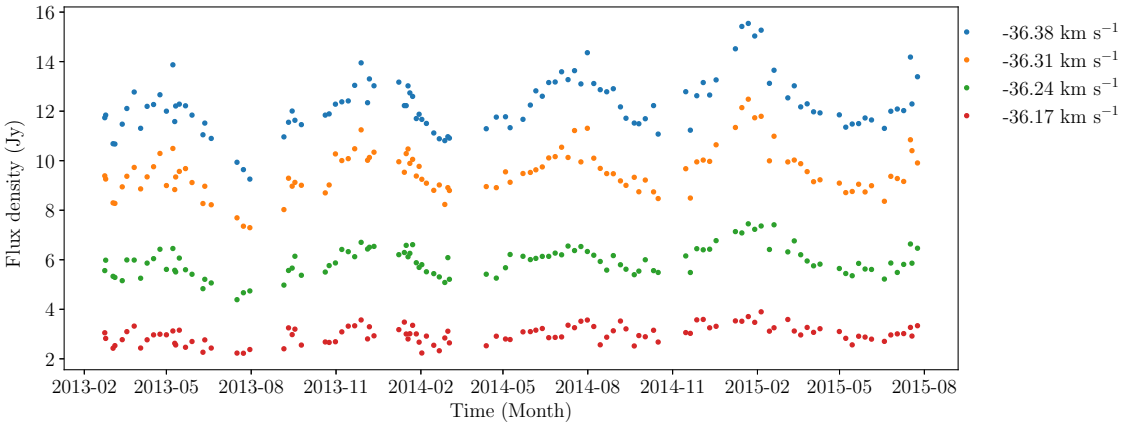

FIGURE C.11: Time-series for the 1667 MHz OH masers at velocities ranging from -36.1 to -36.4 km s^{-1}

Bibliography

Araya, E. D., Hofner, P., Goss, W. M., et al. 2010, APJ, 717, L133

Baars, J. W. M., Genzel, R., Pauliny-Toth, I. I. K., & Witzel, A. 1977, AAP, 500, 135

Batrla, W., Matthews, H. E., Menten, K. M., & Walmsley, C. M. 1987, NAT, 326, 49

Blitz, L. 1993, in Protostars and Planets III, ed. E. H. Levy & J. I. Lunine, 125

Bonnell, I. A. 2001, in IAU Symposium, Vol. 200, The Formation of Binary Stars, ed. H. Zinnecker & R. Mathieu, 23

Bonnell, I. A., & Dobbs, C. L. 2007, in IAU Symposium, Vol. 237, Triggered Star Formation in a Turbulent ISM, ed. B. G. Elmegreen & J. Palous, 344–350

Bonnell, I. A., Vine, S. G., & Bate, M. R. 2004, MNRAS, 349, 735

Breen, S. L., Caswell, J. L., Ellingsen, S. P., & Phillips, C. J. 2010, MNRAS, 406, 1487

Breen, S. L., Ellingsen, S. P., Contreras, Y., et al. 2013, MNRAS, 435, 524

Bronfman, L., Nyman, L. A., & May, J. 1996, AAPS, 115, 81

Carey, S. J., Clark, F., Egan, M., et al. 1998, The Astrophysical Journal, 508, 721

Carey, S. J., Feldman, P., Redman, R., et al. 2000, The Astrophysical Journal Letters, 543, L157

Caswell, J. L. 1996, MNRAS, 279, 79

Caswell, J. L., & Haynes, R. F. 1987, Australian Journal of Physics, 40, 215

Caswell, J. L., Haynes, R. F., & Goss, W. M. 1980, Australian Journal of Physics, 33, 639

Caswell, J. L., Vaile, R. A., & Ellingsen, S. P. 1995, PASA, 12, 37

Caswell, J. L., Fuller, G. A., Green, J. A., et al. 2011, MNRAS, 417, 1964

Choudhuri, A. R. 2010, Astrophysics for physicists (Cambridge University Press)

Churchwell, E. 2002, ARAA, 40, 27

Clark, B. G. 1980, AAP, 89, 377

Cohen, R. J. 1989, Reports on Progress in Physics, 52, 881

Combrinck, L., & Nickola, M. 2001, International VLBI Service for Geodesy and Astrometry 2000 Annual Report, 84

Condon, J. J., & Ransom, S. M. 2016, Essential Radio Astronomy (Princeton University Press)

Contreras, Y., Schuller, F., Urquhart, J. S., et al. 2013, AAP, 549, A45

Cornwell, T. J. 2008, IEEE Journal of Selected Topics in Signal Processing, 2, 793

Cragg, D. M., Johns, K. P., Godfrey, P. D., & Brown, R. D. 1992, MNRAS, 259, 203

Cragg, D. M., Sobolev, A. M., & Godfrey, P. D. 2002, MNRAS, 331, 521

Dartois, E., Schutte, W., Geballe, T. R., et al. 1999, AAP, 342, L32

De Buizer, J. M., Bartkiewicz, A., & Szymczak, M. 2012, APJ, 754, 149

Elitzur, M. 1982, Reviews of Modern Physics, 54, 1225

Elitzur, M. 1992, Annual review of astronomy and astrophysics, 30, 75

Elitzur, M., & Fuqua, J. B. 1989, APJL, 347, L35

Ellingsen, S. P. 2006, APJ, 638, 241

Ellingsen, S. P., Voronkov, M. A., Cragg, D. M., et al. 2007, in IAU Symposium, Vol. 242, Astrophysical Masers and their Environments, ed. J. M. Chapman & W. A. Baan, 213–217

Foley, A. R., Alberts, T., Armstrong, R. P., et al. 2016, MNRAS, 460, 1664

Fomalont, E. B., & Perley, R. A. 1999, in Astronomical Society of the Pacific Conference Series, Vol. 180, Synthesis Imaging in Radio Astronomy II, ed. G. B. Taylor, C. L. Carilli, & R. A. Perley, 79

Garett, M. 2015, Lecture notes on radio telescopes, https://www.strw.leidenuniv.nl/radioastronomy/lib/exe/fetch.php?media=radio_astronomy_lec_2_ma_garrett_2015.comp.pdf, Last accessed on 2019-11-14

Garsden, H., Girard, J. N., Starck, J. L., et al. 2015, A&A, 575, A90

Giannetti, A., Wyrowski, F., Brand, J., et al. 2014, AAP, 570, A65

Goedhart, S., Gaylard, M. J., & van der Walt, D. J. 2003, MNRAS, 339, L33

Goedhart, S., Gaylard, M. J., & van der Walt, D. J. 2004, MNRAS, 355, 553

Goedhart, S., Maswanganye, J. P., Gaylard, M. J., & van der Walt, D. J. 2014, MNRAS, 437, 1808

Goedhart, S., van Rooyen, R., van der Walt, D. J., et al. 2019, MNRAS, 485, 4676

Gray, M. 1999, Philosophical Transactions of the Royal Society of London Series A, 357, 3277

Gray, M. 2012, Maser Sources in Astrophysics, Vol. 50 (Cambridge University Press)

Green, J. A., Caswell, J. L., Voronkov, M. A., & McClure-Griffiths, N. M. 2012, MNRAS, 425, 1504

Green, J. A., & McClure-Griffiths, N. M. 2011, MNRAS, 417, 2500

Hartquist, T. W., Menten, K. M., Lepp, S., & Dalgarno, A. 1995, MNRAS, 272, 184

Hoare, M., Kurtz, S., Lizano, S., Keto, E., & Hofner, P. 2007, B. Reipurth, D. Jewitt & K. Keil, 181

Högbom, J. A. 1974, AAPS, 15, 417

Keto, E. 2003, APJ, 599, 1196

Klessen, R. S., & Glover, S. C. O. 2016, Saas-Fee Advanced Course, 43, 85

Kroupa, P. 2002, Science, 295, 82

Krumholz, M. R. 2015, in Astrophysics and Space Science Library, Vol. 412, Very Massive Stars in the Local Universe, ed. J. S. Vink, 43

Krumholz, M. R., & Bonnell, I. A. 2007, arXiv e-prints, arXiv:0712.0828

Krumholz, M. R., Klein, R. I., McKee, C. F., Offner, S. S. R., & Cunningham, A. J. 2009, Science, 323, 754

Kurtz, S. 2005, in IAU Symposium, Vol. 227, Massive Star Birth: A Crossroads of Astrophysics, ed. R. Cesaroni, M. Felli, E. Churchwell, & M. Walmsley, 111–119

Lehmensiek, R., & Theron, I. P. 2011, IEEE Transactions on Antennas and Propagation, 59, 1894

Lin, C. C., & Swalen, J. D. 1959, Reviews of Modern Physics, 31, 841

Lomb, N. R. 1976, APSS, 39, 447

MacLeod, G. C., & Gaylard, M. J. 1992, MNRAS, 256, 519

MacLeod, G. C., Gaylard, M. J., & Kemball, A. J. 1993, MNRAS, 262, 343

Maswanganye, J. P., Gaylard, M. J., Goedhart, S., van der Walt, D. J., & Booth, R. S. 2015, MNRAS, 446, 2730

Maswanganye, J. P., van der Walt, D. J., Goedhart, S., & Gaylard, M. J. 2016, MNRAS, 456, 4335

Matthews, H., Leech, J., & Friberg, P. 2004, Guide to spectral line observing at the JCMT, Tech. rep., Technical report, JAC

McKee, C. F., & Ostriker, E. C. 2007, ARAA, 45, 565

McKee, C. F., & Tan, J. C. 2002, NAT, 416, 59

Menten, K. M. 1991, APJL, 380, L75

Menten, K. M., Reid, M. J., Pratap, P., Moran, J. M., & Wilson, T. L. 1992, APJL, 401, L39

Motte, F., Bontemps, S., & Louvet, F. 2018, ARAA, 56, 41

Mottram, J. C., Hoare, M. G., Davies, B., et al. 2011, APJL, 730, L33

Napier, P. J. 1999, Astronomical Society of the Pacific Conference Series, Vol. 180, The Primary Antenna Elements, ed. G. B. Taylor, C. L. Carilli, & R. A. Perley, 37

Navarete, F., Damineli, A., Barbosa, C. L., & Blum, R. D. 2015, MNRAS, 450, 4364

Norris, R. P., & Booth, R. S. 1981, MNRAS, 195, 213

Olech, M., Szymczak, M., Wolak, P., Sarniak, R., & Bartkiewicz, A. 2019, MNRAS, 486, 1236

Ott, M., Witzel, A., Quirrenbach, A., et al. 1994, AAP, 284, 331

Perley, R., & Taylor, G. 1999, VLA Calibrator Manual, Tech. rep., Tech. rep., NRAO

Proven-Adzri, E., MacLeod, G. C., van den Heever, S. P., et al. 2019, MNRAS, 487, 2407

Purser, S. J. D., Lumsden, S. L., Hoare, M. G., et al. 2016, MNRAS, 460, 1039

Reid, M. J., & Moran, J. M. 1981, ARAA, 19, 231

Reid, M. J., Menten, K. M., Zheng, X. W., et al. 2009, APJ, 700, 137

Ryle, M., Hewish, A., & Shakeshaft, J. 1959, IEEE Transactions on Antennas and Propagation, 7, 120

Samal, M. R., Deharveng, L., Zavagno, A., et al. 2018, AAP, 617, A67

Scargle, J. D. 1982, APJ, 263, 835

Scheffler, H., & Elsasser, H. 1988, Science, 240, 1680

Schuster, A. 1898, Terrestrial Magnetism (Journal of Geophysical Research), 3, 13

Schwab, F. R. 1984, aj, 89, 1076

Sobolev, A. M., Cragg, D. M., & Godfrey, P. D. 1997, AAP, 324, 211

Sobolev, A. M., Cragg, D. M., & Godfrey, P. D. 2002, MNRAS, 331, 521

Stahler, S. W., & Palla, F. 2005, The Formation of Stars (Wiley-VCH)

Strel'Nitskii, V. S. 1974, SOVAST, 17, 717

Sugiyama, K., Nagase, K., Yonekura, Y., et al. 2017, pasj, 69, 59

Szymczak, M., Wolak, P., & Bartkiewicz, A. 2015, MNRAS, 448, 2284

Tan, J. C., Beltrán, M. T., Caselli, P., et al. 2014, in Protostars and Planets VI, ed. H. Beuther, R. S. Klessen, C. P. Dullemond, & T. Henning, 149

Thompson, A. R., Moran, J. M., & Swenson, G. W. 2017a, Van Cittert–Zernike Theorem, Spatial Coherence, and Scattering (Cham: Springer International Publishing), 767–786

Thompson, A. R., Moran, J. M., & Swenson, George W., J. 2017b, Interferometry and Synthesis in Radio Astronomy, 3rd Edition, doi:10.1007/978-3-319-44431-4

Tigé, J., Motte, F., Russeil, D., et al. 2017, AAP, 602, A77

Turner, B. E. 1970, pasp, 82, 996

Urquhart, J. S., König, C., Giannetti, A., et al. 2018, MNRAS, 473, 1059

van der Walt, D. J. 2011, AJ, 141, 152

Van der Walt, D. J. 2014, Astronomy & Astrophysics, 562, A68

VanderPlas, J. T. 2018, APJS, 236, 16

Walsh, A. J., Burton, M. G., Hyland, A. R., & Robinson, G. 1998, MNRAS, 301, 640

Weinreb, S., Barrett, A. H., Meeks, M. L., & Henry, J. C. 1963, NAT, 200, 829

Weinreb, S., Meeks, M. L., & Carter, J. C. 1965, NAT, 208, 440

Wheelwright, H. E., de Wit, W. J., Oudmaijer, R. D., et al. 2012, AAP, 540, A89

Wrobel, J. M., & Walker, R. C. 1999, Astronomical Society of the Pacific Conference Series, Vol. 180, Sensitivity, ed. G. B. Taylor, C. L. Carilli, & R. A. Perley, 171

Yorke, H. W., & Sonnhalter, C. 2002, APJ, 569, 846

Zernike, F. 1938, Physica, 5, 785

Zinnecker, H., & Yorke, H. W. 2007, ARAA, 45, 481